CORA Cork Open Research Archive
Cartlann Taighde Oscailte Chorcaí

Title	Advanced processing strategies for site-controlled pyramidal quantum dots
Authors	Varo, Simone
Publication date	2021-10-07
Original Citation	Varo, S. 2021. Advanced processing strategies for site-controlled pyramidal quantum dots. PhD Thesis, University College Cork.
Type of publication	Doctoral thesis
Rights	© 2021, Simone Varo. - https://creativecommons.org/licenses/by-nc-nd/4.0/
Download date	2026-11-01 15:25:18
Item downloaded from	https://hdl.handle.net/10468/12475



UCC
University College Cork, Ireland
Coláiste na hOllscoile Corcaigh

Ollscoil na hÉireann, Corcaigh

National University of Ireland, Cork



Advanced processing strategies for site-controlled pyramidal quantum dots

Thesis presented by

Simone Varo, M.Sc

for the degree of

Doctor of Philosophy

University College Cork

College of Science, Engineering and Food Science

Department of Physics

Tyndall National Institute

Head of School/Department: Prof. John McInerney

Supervisor: Dr. Emanuele Pelucchi

2021

Table of Contents

1. **Introduction**……..1
   - **1.1 General framework**……..1
   - **1.2 Non classical light sources for photonic quantum computing: requirements**……4

2. **Pyramidal quantum dots**……15
   - **2.1 Growth of PQDs**……15
   - **2.2 Post-growth sample processing techniques: back-etching**……18
   - **2.3 Post-growth sample processing techniques: polishing**……21
   - **2.4 Typical spectral features of quantum dots under optical excitation**……24
   - **2.5 Excitation schemes**……27
   - **2.6 Development of GaAs in AlGaAs and GaAs in superlattice barriers dots**……32

3. **Advanced processing strategies for Pyramidal Quantum Dots: Fabrication of site-controlled 3D dielectric structures using Electron Beam Induced Deposition**……43

4. Design and fabrication of micro/nanopillars to increase light extraction efficiency.....65
4.1 Introduction: photonic nanowires.....65
4.2 A self-aligning process for fabricating photonic nanowires with pyramidal quantum dots.....67
4.3 FDTD simulations of photonic nanowires with triangular sections.....69
4.4 Dry etching: fundamentals.....72
4.5 Fabrication of photonic micro/nanopillars: challenges and key results.....76
4.6 Development of an inversion technique: preliminary results.....80

5. Strategies for mitigation of Fine Structure Splitting: piezoelectric actuators.....87
5.1 The need of post-growth tuning mechanisms.....87
5.2 strain in semiconductors.....88
5.3 fabrication of piezoelectric devices for strain tuning.....89

6. A theoretical proposal for the a-posteriori mitigation of the effects of excitonic fine structure splitting……96

7. TEM analysis of Pyramidal Quantum Dots……116

7.1 Transmission electron microscopy: basics……117

7.2 Sample preparation techniques: lamellae cutting from back-etched structures……121

7.3 Advanced sample preparation techniques: cutting of lamellae from nanopillars……124

7.4 A different approach: Atom Probe Tomography……127

7.5 Fabrication of samples for APT-first strategy……129

7.6 Fabrication of samples for APT-direct milling using FIB……130

8. Conclusions……134

Appendix……137

Declaration

This is to certify that the work I am submitting is my own and has not been submitted for another degree, either at University College Cork or elsewhere. All external references and sources are clearly acknowledged and identified within the contents. I have read and understood the regulations of University College Cork concerning plagiarism and intellectual property.

Simone Varo,

Tyndall National Institute,

University College Cork,

August 2021

Abstract

Today, the world is on the verge of a new technological breakthrough that has been called the “second quantum revolution”: much like the understanding of semiconductor physics paved the way for the development of integrated circuits and ushered the age of information technology, the development of the first working quantum computers might start a profound change in the way we process information, and pave the way for much anticipated technological breakthrough.

In my thesis, I have investigated the applications of Pyramidal Quantum Dots (PQDs) as potential sources of single and entangled photons, with a particular focus on improving their quality and brightness, and explored new approaches for their processing that would make them suitable for integration in future quantum devices.

In order to address the limits of the conventional InGaAs in GaAs PQDs in relation to resonant pumping of the biexcitonic state, I contributed to the development of two new families of dots: GaAs in AlGaAs PQDs and GaAs dots confined by superlattice barriers. For the former, only results of growths on templates of smaller size were reported in the literature, while the latter is a completely new family of PQDs altogether. Results reported in this thesis indicate a surprising uniformity in spectral features for either family, and demonstrate that resonant excitation can indeed be achieved due to the binding biexcitonic state.

In collaboration with Prof. Di Falco’s group in the University of St. Andrews (UK), we have demonstrated potential applications in the field of semiconductor non-classical light sources of the Electron Beam Induced Deposition technique, which allowed us to fabricate complex dielectric nanostructures directly above the quantum emitters. Our work showed how this approach doesn’t cause any significant degradation in the emission spectra, and was complemented by a large number of simulations to elucidate

the underlying mechanisms that allow SiO_2 nanostructures to boost light extraction efficiency form the semiconductor matrix depending on their shape.

A more promising approach to boost the brightness of our dots was also developed, in the form of a self-aligning technique that allows to fabricate micro and nanopillars using dry etching, and that allowed us to achieve our own record of brightness.

Furthermore, an approach to compensate for the effects of the excitonic fine structure splitting on the level of entanglement was devised: the model we have developed complements similar proposals that have previously appeared in the literature, but is also extremely intuitive due to its sequential logic gate structure.

Finally, for the first time transmission electron microscopy of PQDs was achieved in a joint effort with Queen's University Belfast, a success in large part made possible by the new processing strategies devised in this thesis, and whose preliminary results are here reported.

Acknowledgments

During my three and a half years in Tyndall I got the opportunity to work with several great researchers, without whom many of the results described in this thesis would have never been achieved.

My gratitude goes in particular to Dr. Gediminas Juska for having taken care of most of the spectroscopic characterization of the many samples I made, and to Dr. Agnieska Gocalinska for having had the patience of doing the MOVPE growths I required: they have been exceptional colleagues as well as mentors.

I would like to thank Dan O' Connell, Alan Hydes and Dr. James O' Callaghan for the assistance they provided me with in the cleanroom, and for the many suggestions they gave me during the years.

I am also particularly grateful to Dr. Michael Schmidt for his assistance with the Focussed Ion Beam, and the many hours we have spent together trying to find the best way to mill our samples.

My co-authors from the University of St. Andrews, Prof. Andrea Di Falco and his former PhD student Dr. Xin Li deserve a special mention: our successful collaboration is a testament to their hard work and commitment to our shared project.

Likewise, I would like to thank Dr. Kristina Holsgrove and Dr. Miryam Arredondo-Arechavala from Queen's University Belfast for their dedication to the TEM side of our project, and the many fruitful discussions we have had.

Finally, I would like to thank all of my current and previous fellow group members: Stefano, Iman, Francesco, Luca, Enrica, John and Nicola, for the amazing work we have done together. A special mention goes to my surpervisor, Dr. Emanuele Pelucchi, for having always encouraged and helped me in these years, and to my parents and my dear friend Princia for having supported me all the way

Publications

Journal papers:

1. S. T. Moroni, **S. Varo**, G. Juska, T. H. Chung, A. Gocalinska, E. Pelucchi "*Vanishing biexciton binding energy from stacked, MOVPE grown, site-controlled pyramidal quantum dots for twin photon generation*", Journal of Crystal Growth **506,** 36–39 (2019)

2. Gediminas Juska, Iman Ranjbar Jahromi, Francesco Mattana, **Simone Varo**, Valeria Dimastrodonato, and Emanuele Pelucchi**,** "*Biexciton Initialization by Two-Photon Excitation in Site-Controlled Quantum Dots: the Complexity of the Antibinding State Case*", Applied Physics Letters **117**, 134001 (2020)

3. **Simone Varo**, Xin Li, Gediminas Juska, Iman Ranjbar Jahromi, Agnieszka M. Gocalinska, Andrea Di Falco, and Emanuele Pelucchi, "*Planar Semiconductor Membranes with Brightness Enhanced Embedded Quantum Dots via Electron Beam Induced Deposition of 3D Nanostructures: Implications for Solid State Lighting*", ACS Applied Nano Materials 3, 12401-12407, (2020)

4. Iman Ranjbar Jahromi, Gediminas Juska, **Simone Varo**, Francesco Basso Basset, Francesco Salusti, Rinaldo Trotta, Agnieszka Gocalinska, Francesco Mattana, and Emanuele Pelucchi, "*Optical Properties and Symmetry Optimization of Spectrally (Excitonically) Uniform Site-Controlled GaAs Pyramidal Quantum Dots*" Appl. Phys. Lett. **118**, 073103 (2021)

5. **Simone Varo**, Gediminas Juska, Emanuele Pelucchi, "*An intuitive scheme for the restoration of entanglement for polarization-*

entangled photons emitted from quantum dots with non-vanishing fine structure splitting"-submitted

6. Kristina M. Holsgrove, Tamsin O'Reilly, **Simone Varo**, Demie M. Kepaptsoglou, Emanuele Pelucchi and Miryam Arredondo, "*Characterization of III-V pyramidal QDs by TEM techniques*"-to be submitted
7. **Simone Varo,** Gediminas Juska and Emanuele Pelucchi, "A novel technique for the fabrication of photonic nanowires self-aligned to quantum dots: prospects and challenges"-to be submitted

Conference papers:

1. **S. Varo**, G. Juska, I. Ranjbar, S. Moroni, A. Gocalinska, and E. Pelucchi "*Engineering site-controlled quantum dots for optical quantum information processing*", Proc. SPIE 11085, Low-Dimensional Materials and Devices 2019, 1108507

Conferences:

01. E. Pelucchi (*invited talk*), G. Juska, S. T. Moroni, **S. Varo**, and A. Gocalinska, "*Engineering opportunities (and struggles) with site-controlled Pyramidal quantum dots*", 6th international workshop on "Engineering of Quantum Emitter Properties" – 5-6/12/2018, Rome, Italy.

02. **S. Varo** (*invited talk, presenting author)*, G. Juska, I. Ranjbar, S. T. Moroni, A. Gocalinska, R. Trotta, J. Martín-Sánchez, H. Huang, A. Rastelli and E. Pelucchi, "*Prospects and applications of site-controlled pyramidal quantum dots*", 8th Applied Optics and Photonics China (AOPC 2019) 7 -9 July 2019 Beijing China

03. E. Pelucchi (*invited talk*), G. Juska, S. T. Moroni, **S. Varo**, I. Ranjbar, A. Gocalinska, "*Engineering site-controlled quantum dots for optical*

quantum information processing", SPIE Optics + Photonics 2019, 11–15 August 2019 San Diego Convention Center, San Diego, California, USA

04. Emanuele Pelucchi (*invited talk*), G. Juska, **S. Varo**, I. Ranjbar, S. T. Moroni and A. Gocalinska, "*Integration challenges with site-controlled quantum dots for quantum information processing*", EQEP 2019 - 7th International Workshop on Engineering of Quantum Emitter Properties, 11th to 13th of December 2019 at Technische Universität Berlin, Germany

05. G. Juska (*invited talk*), S.T. Moroni, **S. Varo**, T-H. Chung, A. Gocalinska, E. Pelucchi, *Engineering flexibility of site-controlled Pyramidal quantum dots for single and entangled photon emission*, SPIE Security + Defence, Berlin, Germany, 10 - 13 September 2018.

06. Gediminas Juska (*oral*), Stefano T. Moroni, **Simone Varo**, Tung-Hsun Chung, Agnieszka Gocalinska, and Emanuele Pelucchi (*presenting author*), "*Engineering flexibility of MOVPE grown site-controlled Pyramidal quantum dots (PQDs)*" 19th International Conference on Metalorganic Vapor Phase Epitaxy, (ICMOVPE-XIX), June 3 – 8, 2018 Nara Kasugano International Forum, Nara, Japan.

07. S. Moroni (*oral*), G. Juska, **S. Varo**, T.H. Chung, A. Gocalinska, R. Trotta, J. Martín-Sánchez (Spain), H. Huang, A. Rastelli, E. Pelucchi, "*A unique tuneable, scalable and easily integrable source of quantum light based on pyramidal quantum dots*" ICPS 2018 - 34th International conference on the physics of semiconductors - Montpellier, on July 29 to August 3, 2018.

08. **S. Varo** (*oral*), S. T. Moroni, G. Juska, T. H. Chung, A. Gocalinska, R. Trotta, J. Martin-Sanchez, H. Huang, A. Rastelli and E. Pelucchi, "*Site-controlled pyramidal dots: from quantum light to quantum devices*", Photonics Ireland Conference 2018 Pairc ui Chaoimh, Cork, Ireland, 3·5 September 2018

1. Introduction

1.1 General framework

It was in 1938 that Konrad Zuse built the first modern computer in his apartment in Berlin, called the "Z1": it was soon followed by more advanced electromechanical models built for the *Luftwaffe* (German Air Force), which needed a way to reliably perform tedious calculations related to airplane design. In the same years, but working for the opposite front of the war, Thomas Flowers began building the *Colossus* to speed up the codebreaking effort.

The rush for developing faster and better performing machines had started, and was about to become even more competitive with the beginning of the Cold War: the ability to perform calculations at ever increasing speeds quite literally propelled the Human Race to the stars, and ushered a new industrial revolution and the dawn of the Information Age.

This was made possible in the first place by technological advancements in the field of semiconductor device processing, that allowed to progressively reduce the footprint of the fundamental components of integrated circuits[1], as empirically shown by Gordon Moore with the law that bears his name.

Today, however, there is a general consensus that the main strategy so far used to improve the performance of integrated circuits has finally exhausted its momentum: the gate length of modern transistors is approaching the limit where quantum effects will begin to dominate[2] and cause greater leakage currents between source and drain, calling for novel approaches to further raise the performance of modern computers.

While this problem can be somewhat worked around using parallel architectures, there is a more fundamental one that presses for a paradigm shift, rather than an incremental advance: simulation of quantum systems is

usually extremely demanding in terms of computational resources and can only be performed for relatively simple cases with a small number of particles[3]. Richard Feynman was the first to propose to simulate quantum systems by using something that shares their quantum behavior, rather than trying to represent them via strings of Boolean values: what he was envisioning was a device that processes quantum objects, and that would have been known in the years to come as a quantum computer.

The whole field of quantum computing, initially considered not very different from fringe science, began booming when Peter Shor proposed the first, practical, quantum algorithm for the factorization of a number in its prime components: he showed that such an operation, that would scale exponentially in time with increasing complexity on a classical computer, would scale polynomially by fully harnessing the power of a (theoretical) quantum computer. Exactly like Turing's work during World War II, a revolution in codebreaking paved the way for an unexpected, but highly welcomed, new field to explore.

Now, the world might be on the verge of a new era, as the first quantum computers begin to appear. Whether they will ever be able to deliver the (great) expectations they have been associated with remains to be seen, but the effort to solve scalability and decoherence problems is titanic: rarely in history so many scientists and engineers have been devoting themselves to bring to bear not the solution to a problem, but a concept that, by its nature, transcends a single field. From semiconductor Physics to superconductivity, from photonics to software engineering, no effort is spared in trying to make the dream of a quantum computer a reality.

When Zuse started building his Z-series of computer, the technology he was using was changing between different generations of his devices, as he was trying to figure out the best one to build his computing machine with: likewise,

it is not obvious today what the natural platform to build a quantum computer from could be. Superconductive devices seem to be dominating the competition so far[4–6], but they are plagued by problems of decoherence, and stringent requirements in terms of operating temperature. Photonic quantum computing is attractive due to possibility of easily transferring photons over significant distances (thus overlapping with the field of quantum cryptography), and the fact that properties of the photons such as their phase can be easily manipulated: this led to the proposal of a Linear Optic Quantum Computer (LOQC)[7–10].

The fundamental unit of classical information is a bit: an object that can assume only 2 distinct values, and that could be represented by the voltage of a transistor, the charge in a vacuum tube, the holes (or lack thereof) in a punchcard or even the position of some mechanical part. Its quantum correspondent object is called a Qubit, which is the short for Quantum Bit: likewise, different quantum objects can be used to represent it, as long as they can exist in a superposition of 2 states. Basic quantum mechanics tells us that if we consider a system that can exist in two possible, distinguishable configurations, $|0\rangle$ and $|1\rangle$ that have the same energy, the most general way of writing the state of the system is as a quantum superposition of said configurations: $|\psi\rangle=\alpha|0\rangle+\beta|1\rangle$. The states $|0\rangle$ and $|1\rangle$ are called a (canonical or standard) computational basis, as they define the Hilbert space a Qubit will belong to, with $|\alpha|^2$ and $|\beta|^2$ giving the probabilities of a measurement outcome giving either state, as per the Copenhagen interpretation of quantum mechanics. The fact that measurement operations will indeed collapse quantum states implies that the outcome of a quantum computation will always be a classical in nature, such as a string of bits.

1.2 Non classical light sources for photonic quantum computing: requirements

As discussed before, single photons are simple quantum objects that are quite attractive as a resource for quantum computing, especially in view of the possibility of encoding information in their polarization states (and superpositions thereof). They tend to be quite resilient with respect to external perturbations and there is a mature technology for their transmission and manipulation[11–13], although they have limited capabilities of interacting with each other, which stems from their bosonic nature and lack of electric charge: this greatly complicates the development of multi photon quantum gates, such as the fundamental CNOT.

Beside the challenges related to the fabrication of photonic circuits that could act as quantum processors, a significant obstacle is represented by the need to have a source of single photons of high quality to start with, which translated in the latter's need to fulfill several stringent requirements:

- **On-demand generation of photons:** similarly to how a classical CPU works in steps defined by a clock, such as a crystal oscillator, an ideal source of photons would have to emit them at regular intervals in time, dictated by some external signal. For emitters such as quantum dots, atoms/ions or molecules, this implies a fast pumping to the excited state and a short relaxation to the ground via emission of a photon[14–17]. It also implies that a high quantum yield is required with most, and desirably all, of the recombinations to the ground state happening in a radiative way to ensure deterministic generation of the quantum resource.

- **High brightness:** strongly related to the previous point, this umbrella term indicates that a large photon flux is not only desirable to achieve

high frequency operation, but is also a fundamental requirement, as photons will have to be coupled to a photonic circuit for any operation to be performed onto them. A low brightness of the source will also render it non-deterministic, if most photons emitted are lost and not harvested and coupled to the circuit, rendering the ability to generate them on demand a moot point[18]. For solid state sources such as quantum dots this translates to an efficient extraction from the semiconductor matrix and an optimal coupling to the collecting optics. In a broader sense, this could also imply requirements on the far field profile that for instance has to match that of a single mode waveguide[15,19–21].

- **Single photon purity:** The purity of a single photon source is a parameter that indicates its quality as a single photon emitter. It's gauged by the second order autocorrelation at zero delay $g^2(0)$, which would be zero for an ideal single photon source. The autocorrelation function is usually measured in a standard Hanbury-Brown-Twiss experiment that employs a 50:50 beam splitter to send half of the incoming photon flux to each of a pair of detectors. Since the autocorrelation function is defined as:

$$g^2(\tau) = \frac{< N_1(t)N_2(t+\tau) >}{< N_1(t) >< N_2(t+\tau) >}$$

with N_1 and N_2 the number of counts registered in either detector, the condition $g^2(0)$=0 is equivalent to never having two photons detected simultaneously on the two detectors. This condition is called *antibunching.*

- **Indistinguishability:** For photons to exhibit bosonic coalescence at a beam splitter, they need to be indistinguishable, that is, they ought to

be almost perfectly identical[22,23]. This implies not only that they need to have the same energy, but also that their wavepackets should be the same. If we consider a quantum dot in some excited state, interaction with phonons, charges generated in the surrounding matrix and even nuclear spins can give rise to *spectral diffusion* (e.g. via quantum confined Stark effect) and *phase jumps.* In order to mitigate these effects, besides operating at a low temperature, environmental noise should be kept to a minimum by reducing generation of free charges around the quantum dot and minimizing the density of defects in its proximity. A widely used approach is also to limit the emitter's radiative recombination lifetime, so that it is much shorter than its coherence time: this is achieved by exploiting microcavities to provide a Purcell effect. A photon wavepacket that has not been affected by decoherence mechanisms is called a (Fourier) transform limited one. Bosonic coalescence provides a way to experimentally quantify the degree of indistinguishability of photons emitted in sequence by a source in the form of the visibility V of a Hong-Ou-Mandel experiment[24,25]. This can be seen as an evolution of the HBT experiment used to assess the degree of single photon emission: if two indistinguishable photons are fed to the input arms of a beam splitter, bosonic coalescence will result in them leaving on the same output arm, meaning that no simultaneous counts will be registered by two detectors placed on the outputs: the hallmark of an indistinguishable photon source is thus once more a pronounced dip (ideally reaching zero) at zero delay of the coincidence counts.

- **Entangled photon emission:** The ability of a source to generate entangled photons is of great importance for quantum communications and especially quantum cryptography, with quantum key distribution

algorithms such as the BB84[26] based on the distribution of the components of an entangled EPR (Einstein-Podolsky-Rosen) pair. Several different types of entanglement are possible such as energy or time-bin entanglement[27,28], but in the course if this thesis we will mostly refer to polarization entanglement[29,30]. Several parameters can be used to quantify the degree of entanglement, such as the Fidelity, Concurrence and Peres criterion. A deeper discussion regarding (polarization) entanglement is contained in chapter 6.

Besides, there are a few features of an ideal source that would be desirable, although not strictly necessary, for quantum technology applications:

- **Electrical pumping:** While most photon sources are today optically pumped, these schemes usually require expensive equipment and large (bench top) apparatuses that complicate miniaturization. Achieving electrical pumping would indeed be a desirable outcome, and it would help bridge the technological gap between photonic and superconductive quantum computing, although only a few results in this sense have been reported so far[31–35].

- **Room temperature operation:** photonic source such as quantum dots or molecules have to be operated at cryogenic temperatures of a few Kelvins in order to generate photons of acceptable quality. There is hope that in the future GaN quantum dots[36–40] might allow for operation at much higher temperatures.

- **Operating wavelength:** In order to minimize losses, it would be desirable for the photon source to operate at a wavelength where absorption in the chosen photonic platform is minimized. This requirement becomes even more stringent when we also consider

quantum communications and cryptography[41,42], where photons are to be transferred over great distances using optical fibers. It is possible to shift the frequency of single photons using non-linear effects or frequency modulation[43,44], but at the price of an increase in complexity and efficiency losses.

- **Scalability:** In order to move from exploratory lab testing to industrial production, the fabrication process of the sources should be deterministic. This implies both a form of site control[45–48], where the sources are fabricated at predetermined locations, and a high yield of sources with acceptable properties (e.g. spectral quality), although the latter problem can be somewhat mitigated via the use of external tuning knobs[49–52].

The workhorse of photonic quantum information was initially represented by Spontaneous Parametric DownConversion (SPDC), which allows for generation of single and entangled photons[53,54] with very high purity and entanglement fidelity using non-linear crystals. Such a process is however probabilistic in nature, and thus fails to deliver photons on demand. Meanwhile, in the last 20 years advances in epitaxial growth technology have brought a new generation of solid state quantum emitters in the form of quantum dots[55,56], of sufficient quality[47,51,57–60] to become serious contenders as the ideal source for photonic quantum technologies. Still, this system is not without its drawbacks, as the fact that the emitter is embedded in a complex matrix creates serious dephasing problems as previously discussed, and the high refractive index of the semiconductor material significantly limits the brightness of the source due to total internal reflection.

The class of quantum dots that was used throughout my research work in Tyndall is known as Pyramidal Quantum Dots (PQDs), whose main features will be described in the following chapter.

1. Moore, G. E. Lithography and the future of Moore's law. *Integr. Circuit Metrol. Insp. Process Control IX* **2439**, 2–17 (1995).
2. Powell, J. R. The quantum limit to Moore's law. *Proc. IEEE* **96**, 1247–1248 (2008).
3. Cao, Y. *et al.* Quantum Chemistry in the Age of Quantum Computing. *Chem. Rev.* **119**, 10856–10915 (2019).
4. Clarke, J. & Wilhelm, F. K. Superconducting quantum bits. *Nat. 2007 4537198* **453**, 1031–1042 (2008).
5. Kjaergaard, M. *et al.* Superconducting Qubits: Current State of Play. *Annu. Rev. Condens. Matter Phys.* **11**, 369–395 (2020).
6. Huang, H.-L., Wu, D., Fan, D. & Zhu, X. Superconducting quantum computing: a review. *Sci. China Inf. Sci. 2020 638* **63**, 1–32 (2020).
7. Kok, P. *et al.* Linear optical quantum computing with photonic qubits. *Rev. Mod. Phys.* **79**, 135 (2007).
8. O'Brien, J. L., Pryde, G. J., White, A. G., Ralph, T. C. & Branning, D. Demonstration of an all-optical quantum controlled-NOT gate. *Nat. 2003 4266964* **426**, 264–267 (2003).
9. Browne, D. E. & Rudolph, T. Resource-Efficient Linear Optical Quantum Computation. *Phys. Rev. Lett.* **95**, 010501 (2005).
10. O'Brien, J. L. Optical quantum computing. *Science (80-.).* **318**, 1567–

1570 (2007).

11. Crespi, A. *et al.* Integrated photonic quantum gates for polarization qubits. *Nat. Commun.* **2**, 566 (2011).

12. Norman, J. C., Jung, D., Wan, Y. & Bowers, J. E. Perspective: The future of quantum dot photonic integrated circuits. *APL Photonics* **3**, 030901 (2018).

13. O'Brien, J. L., Furusawa, A. & Vučković, J. Photonic quantum technologies. *Nat. Photonics* **3**, 687–695 (2009).

14. Senellart, P., Solomon, G. & White, A. High-performance semiconductor quantum-dot single-photon sources. *Nat. Nanotechnol.* | **12**, (2017).

15. Somaschi, N. *et al.* Near-optimal single-photon sources in the solid state. *Nat. Photonics* **10**, 340–345 (2016).

16. Aharonovich, I., Englund, D. & Toth, M. Solid-state single-photon emitters. *Nat. Photonics* **10**, 631–641 (2016).

17. Lounis, B. & Moerner, W. E. Single photons on demand from a single molecule at room temperature. *Nature* **407**, 491–493 (2000).

18. Auffeves, A. *et al.* Scalable performance in solid-state single-photon sources. *Opt. Vol. 3, Issue 4, pp. 433-440* **3**, 433–440 (2016).

19. Gregersen, N., Nielsen, T. R., Claudon, J., Gérard, J.-M. & Mørk, J. Controlling the emission profile of a nanowire with a conical taper. *Opt. Lett.* **33**, 1693 (2008).

20. Reimer, M. E. *et al.* Bright single-photon sources in bottom-up tailored nanowires. *Nat. Commun.* **3**, 737 (2012).

21. Gschrey, M. *et al.* Highly indistinguishable photons from deterministic

quantum-dot microlenses utilizing three-dimensional in situ electron-beam lithography. *Nat. Commun.* **6**, (2015).

22. Santori, C., Fattal, D., Vuč Kovi, J., Solomon, G. S. & Yamamoto, Y. Indistinguishable photons from a single-photon device.

23. Huber, T., Predojevi, A., Föger, D., Solomon, G. & Weihs, G. Optimal excitation conditions for indistinguishable photons from quantum dots.

24. Hong, C. K., Ou, Z. Y. & Mandel, L. Measurement of subpicosecond time intervals between two photons by interference. *Phys. Rev. Lett.* **59**, 2044 (1987).

25. Bouchard, F. *et al.* Two-photon interference: the Hong–Ou–Mandel effect. *Reports Prog. Phys.* **84**, 012402 (2020).

26. Bennett, C. H. & Brassard, G. Quantum cryptography: Public key distribution and coin tossing. *Theor. Comput. Sci.* **560**, 7–11 (2014).

27. Jayakumar, H. *et al.* Time-bin entangled photons from a quantum dot. *Nat. Commun. 2014 51* **5**, 1–5 (2014).

28. Huber, T. *et al.* Coherence and degree of time-bin entanglement from quantum dots. *Phys. Rev. B* **93**, 201301 (2016).

29. Akopian, N. *et al.* Entangled photon pairs from semiconductor quantum dots. *Phys. Rev. Lett.* **96**, 130501 (2006).

30. Stevenson, R. M. *et al.* Evolution of entanglement between distinguishable light states. *Phys. Rev. Lett.* **101**, 170501 (2008).

31. Lin, X. *et al.* Electrically-driven single-photon sources based on colloidal quantum dots with near-optimal antibunching at room temperature. doi:10.1038/s41467-017-01379-6.

32. Yuan, Z. *et al.* Electrically driven single-photon source. *Science (80-.).*

295, 102–105 (2002).

33. Hargart, F. *et al.* Electrically driven quantum dot single-photon source at 2 GHz excitation repetition rate with ultra-low emission time jitter. *Cit. Appl. Phys. Lett* **102**, (2013).

34. Chung, T. H. *et al.* Selective carrier injection into patterned arrays of pyramidal quantum dots for entangled photon light-emitting diodes. *Nat. Photonics* **10**, 782–787 (2016).

35. Conterio, M. J. *et al.* A quantum dot single photon source driven by resonant electrical injection. *Appl. Phys. Lett.* **103**, 162108 (2013).

36. Deshpande, S., Frost, T., Hazari, A. & Bhattacharya, P. Electrically pumped single-photon emission at room temperature from a single InGaN/GaN quantum dot. *Appl. Phys. Lett.* **105**, 141109 (2014).

37. Arita, M., Roux, F. Le, Holmes, M. J., Kako, S. & Arakawa, Y. Ultraclean Single Photon Emission from a GaN Quantum Dot. *Nano Lett.* **17**, 2902–2907 (2017).

38. Gačević, Ž. *et al.* Emission of Linearly Polarized Single Photons from Quantum Dots Contained in Nonpolar, Semipolar, and Polar Sections of Pencil-Like InGaN/GaN Nanowires. *ACS Photonics* **4**, 657–664 (2017).

39. Xia, S. *et al.* Enhanced Single-Photon Emission from GaN Quantum Dots in Bullseye Structures. *ACS Photonics* **8**, 1656–1661 (2021).

40. Tamariz, S. *et al.* Toward Bright and Pure Single Photon Emitters at 300 K Based on GaN Quantum Dots on Silicon. *ACS Photonics* **7**, 1515–1522 (2020).

41. Kimble, H. J. The quantum internet. *Nature* **453**, 1023–1030 (2008).

42. Gisin, N., Ribordy, G., Tittel, W. & Zbinden, H. Quantum cryptography. *Rev. Mod. Phys.* **74**, 145 (2002).

43. Chen, C., Heyes, J. E., Shapiro, J. H. & Wong, F. N. C. Single-photon frequency shifting with a quadrature phase-shift keying modulator. *Sci. Reports 2021 111* **11**, 1–7 (2021).

44. Matsuda, N. Deterministic reshaping of single-photon spectra using cross-phase modulation. *Sci. Adv.* **2**, e1501223 (2016).

45. Tatebayashi, J. *et al.* Site-controlled formation of InAs/GaAs quantum-dot-in-nanowires for single photon emitters. *Appl. Phys. Lett.* **100**, (2012).

46. Reitzenstein, S. & Forchel, A. Quantum dot micropillars. *J. Phys. D Appl. Phys. J. Phys. D Appl. Phys. J. Phys. D Appl. Phys* **43**, 33001–25 (2010).

47. Juska, G., Dimastrodonato, V., Mereni, L. O., Gocalinska, A. & Pelucchi, E. Towards quantum-dot arrays of entangled photon emitters. *Nat. Photonics* **7**, 527–531 (2013).

48. Calic, M. *et al.* Deterministic radiative coupling of two semiconductor quantum dots to the optical mode of a photonic crystal nanocavity. *Sci. Rep.* **7**, 1–7 (2017).

49. Trotta, R. *et al.* Universal recovery of the energy-level degeneracy of bright excitons in ingaas quantum dots without a structure symmetry. *Phys. Rev. Lett.* **109**, 1–5 (2012).

50. Martín-Sánchez, J. *et al.* Strain-tuning of the optical properties of semiconductor nanomaterials by integration onto piezoelectric actuators. *Semiconductor Science and Technology* vol. 33 39 (2018).

51. Huber, D. *et al.* Highly indistinguishable and strongly entangled photons from symmetric GaAs quantum dots. *Nat. Commun.* **8**, 15506 (2017).

52. Trotta, R. *et al.* Wavelength-tunable sources of entangled photons

interfaced with atomic vapours. *Nat. Commun.* **7**, 1–7 (2016).

53. U'Ren, A. B., Kaneda, F., Garay-Palmett, K. & Kwiat, P. G. Heralded single-photon source utilizing highly nondegenerate, spectrally factorable spontaneous parametric downconversion. *Opt. Express, Vol. 24, Issue 10, pp. 10733-10747* **24**, 10733–10747 (2016).

54. Keller, T. E. & Rubin, M. H. Theory of two-photon entanglement for spontaneous parametric down-conversion driven by a narrow pump pulse. *Phys. Rev. A* **56**, 1534 (1997).

55. Stevenson, R. M. *et al.* A semiconductor source of triggered entangled photon pairs. *Nature* **439**, 178–182 (2006).

56. Shields, A. J. Semiconductor quantum light sources. *Nat. Photonics* **1**, 215–223 (2007).

57. Liu, J. *et al.* A solid-state source of strongly entangled photon pairs with high brightness and indistinguishability. *Nat. Nanotechnol.* **14**, 586–593 (2019).

58. Kiravittaya, S., Rastelli, A. & Schmidt, O. G. Advanced quantum dot configurations. *Reports Prog. Phys.* **72**, 046502 (2009).

59. Gurioli, M., Wang, Z., Rastelli, A., Kuroda, T. & Sanguinetti, S. Droplet epitaxy of semiconductor nanostructures for quantum photonic devices. *Nature Materials* vol. 18 799–810 (2019).

60. Basso Basset, F. *et al.* High-Yield Fabrication of Entangled Photon Emitters for Hybrid Quantum Networking Using High-Temperature Droplet Epitaxy. *Nano Lett.* **18**, 505–512 (2018).

2. Pyramidal quantum dots

2.1 Growth of pyramidal quantum dots

Pyramidal quantum dots (PQDs) are a family of inherently site-controlled quantum emitters, fabricated using Metal-Organic Vapor Phase Epitaxy (MOVPE)[1]. Their fabrication process is sketched in figure 2.1: it starts by defining an ordered array of inverted tetrahedral holes on an 111B oriented GaAs wafer using a combination of lithography and selective chemical etch. A Br:MeOh etchant stops on the 3 111A planes, and thus exposes the faces of an inverted tetrahedron.

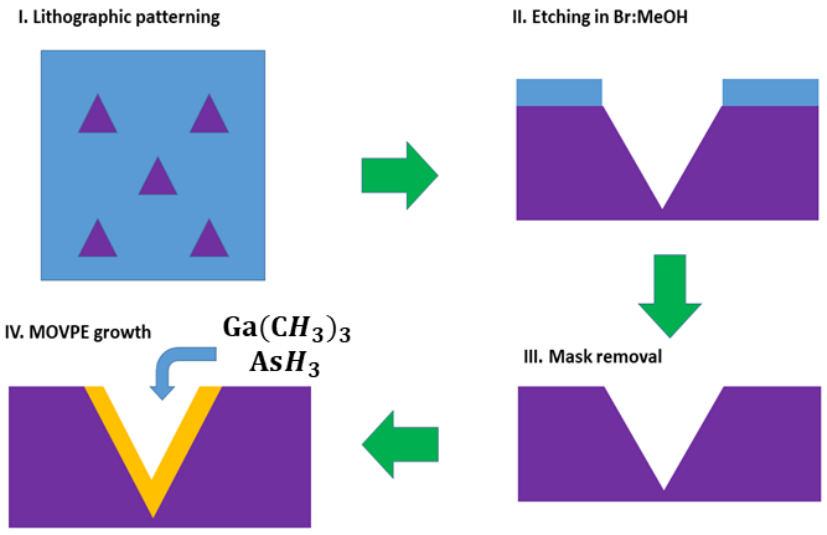


Figure2.1 Steps in the fabrication of Pyramidal Quantum dots

If the wafer is then loaded in an MOVPE reactor, the different chemical behaviors of the various crystal planes come once more into play: the 3 111A planes allow for an easier thermokinetic dissociation of the metalorganic precursors, de facto allowing for epitaxial growth to take place almost exclusively within the tetrahedral recesses if proper conditions in terms of temperature are met. A mathematical model was developed in our group[2] to

describe the growth process, and its heart is a reaction-diffusion equation of the form:

$$D_i \nabla^2 n_i + F_i - \frac{n_i}{\tau_i} = 0$$

Where D_i, F_i and τ_i are the diffusion constant, effective atomic flux and incorporation time for each atomic species. All of these parameters are also crystal-plane dependent, and in particular the aforementioned surface-catalyzed decomposition of the metalorganic precursors translates in a significant source term (F_i) only inside the recess, thus confining epitaxial growth to the three 111A faces and the bottom of the tetrahedral hole.

In a simplified picture, this allows for the growth of epitaxial layers that mimic the shape (and symmetry) of the inverted tetrahedral hole[3]; however, the growth of ternary alloys is often complicated by the different dissociation kinetics and diffusion coefficients of the various precursors: these create what are called “segregation effects”, that is, spatial variation in the stoichiometry of the grown alloys within the 3 dimensional grown layer[4]. These are actually a result of the competition of the different group III adatoms for bonding sites. Far from being a nuisance, they allow for the spontaneous creation of a plethora of nanostructures within the epitaxial structure, as shown in figure 2.2: for example, growth of an $Al_xGa_{1-x}As$ alloy will result in a symmetric region along the axis of the tetrahedron with lower Al content, and thus a smaller bandgap, resulting in a quantum wire. It should be noted that this approach to fabricate quantum dots and other nanostructures in an inverted tetrahedral template can be considered a 3-dimensional extension of growth techniques of quantum wires on V grooves[5,6].

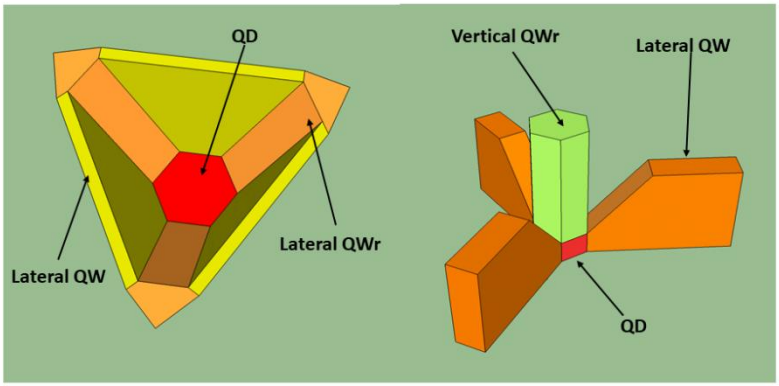


Figure 2.2 Nanostructures formed during growths. Left: InGaAs dots are grown alongside three lateral quantum wres and quantum wells. Right: GaAs in AlGaAs dots are formed alongside three lateral quantum wells and a vertical quantum wire

If a sufficiently thin layer of semiconductor material is grown between two higher-bandgaps layers, a quantum dot will be deterministically formed along the axis of the tetrahedron[7]: this is in stark contrast with most other quantum dot systems (e.g. Stranski-Kranstanov or self-assembled ones) that instead are randomly positioned due to their fabrication process relying on strain relaxation of non-lattice matched epitaxial layers. It should be noted that other ways to fabricate site-controlled quantum dots exist, such as the infilling of nanoholes defined with electron beam lithography[8], but the growth of the quantum emitter so close to processed surfaces usually severely degrades its optical quality: in PQDs these effects can be reduced if the tetrahedral recess is made sufficiently large to accommodate the growth of a thick buffer layer, resulting in quantum dots of superior quality.

Furthermore, pyramidal quantum dots are believed to retain a high degree of symmetry from their growth template, which in principle significantly reduces the excitonic fine-structure splitting by ruling out shape deformations, one of its prime causes in Stranski-Kranstanov quantum dots. Other effects such as alloy disorder[9,10] are however unavoidable, and likely to be responsible for the residual FSS displayed by PQDs.

The first generation of PQDs, developed in Prof. Eli Kapon's group at the EPFL, was mostly grown within medium size recesses (~ 5 micron or smaller), including the later development of relatively small nanoholes (< than 500 nm pitch) with the goal of pursuing photonic crystal integration.

In Tyndall a choice was made to move to holes of larger size, way bigger than precursors' diffusion length (up to 12.5 microns), and to introduce thicker buffer layers which significantly improved the spectral quality of the QDs' emission, and allowed to demonstrate, for the first time, emission of entangled photons from this family of QDs[1,11].

On the other hand, fabrication of dots within structures much larger than their emission wavelength created significant challenges for further processing and interfacing of the emitters with the rest of the world.

2.2 Post-growth sample processing techniques: back-etching

First of all, the growth of pyramidal quantum dots yields a structure with a vestigial recess several microns wide and deep (figure 2.3), located directly above the quantum emitter, which is detrimental for light extraction: extracting light from a high refractive index semiconductor such as GaAs is already difficult in the case of a planar structure due to total internal reflection, but the presence of the recess depresses light extraction efficiency even further, resulting in a brightness so low that little to nothing could be done with this family of emitters in this pristine, as grown configuration.

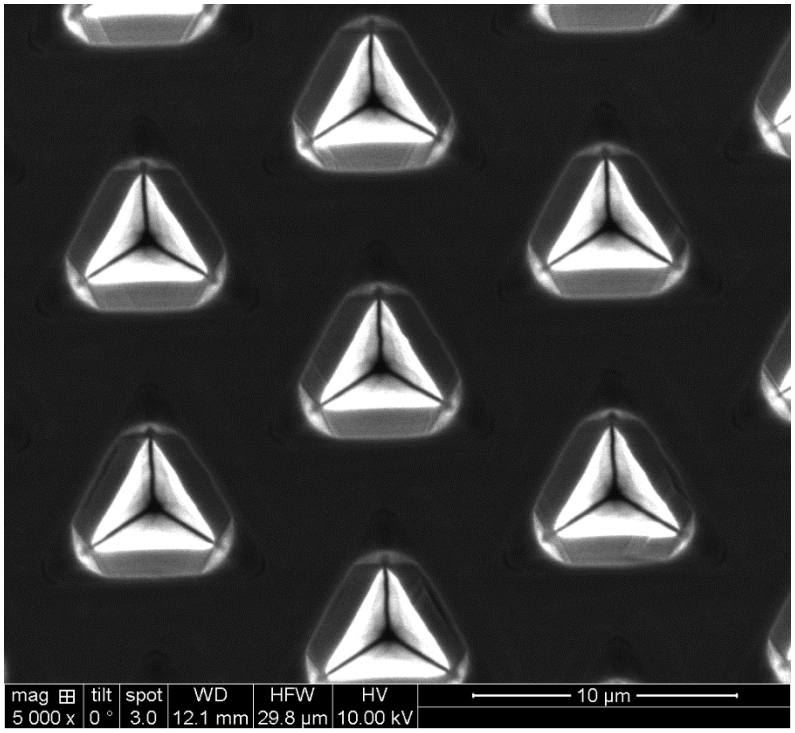


Figure 2.3 SEM image of a PQD sample after MOVPE growth, with the vestigial recess clearly visible

The historical strategy employed to boost light extraction efficiency, and thus the overall brightness of the quantum emitter is called back-etching. The sample is bonded upside down with an adhesive (usually the SU8 resist, which has excellent structural properties after hard baking) on a larger wafer dice in order to provide mechanical support. In the past, bonding was achieved via melting of a Ni-Au eutectic alloy: a much longer procedure that required gold evaporations on both the sample and the carrier, while the introduction of SU8 bonding was an improvement I developed early on in my PhD, and allowed to significantly speed up sample fabrication. Mechanical grinding with large (few microns) Alumina powder solution is employed to remove most of the substrate, leaving a few tens of microns, which are subsequently etched away in a NH_4OH/H_2O_2 solution which easily etches Gallium Arsenide.

If an etch stop layer is inserted in the epitaxial growth (e.g. Al(Ga)As), the chemical etching will expose the pyramids, which will remain in an apex-up configuration, significantly boosting light extraction efficiency and allowing for micro-photoluminescence to be performed (fig. 2.4).

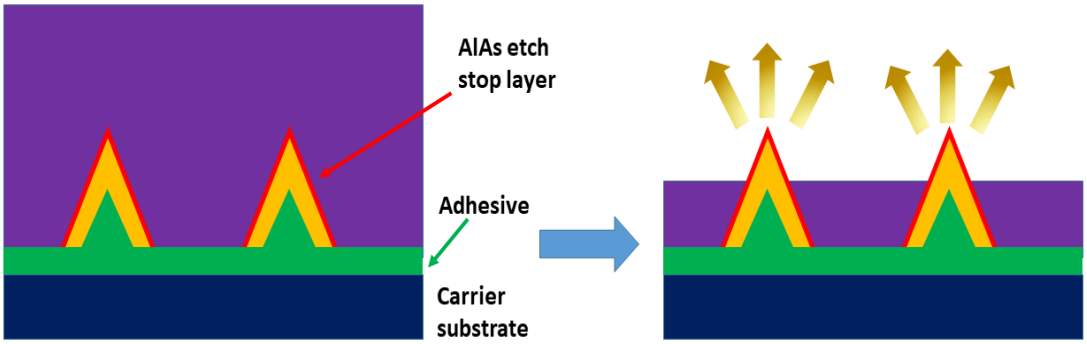


Figure 2.4: sketch of a back-etching process used to expose pyramidal microstructures

This approach, albeit relatively simple and straightforward, is not without drawbacks: first of all, tilts introduced during the various bonding and grinding stages result in poor uniformity across the sample on a macroscopic scale, but even more problematic is the damage often introduced to the quantum emitters due to the aggressive chemical etch: the limited selectivity of the etch stop layer and its oxidation when exposed to air due to the high Al content contribute to the introduction of chemical damage on the pyramidal structures, which in turn translate to a significant broadening of the QD's emission lines, or to a loss of quantum dots spectral features altogether.

As if these shortcomings were not enough, it should be noted that while the brightness of the QD is increased by orders of magnitude with respect to the as grown configuration, it still remains in the range of a few point percent of the total emission of the dot, while the tetrahedral shape of the pyramidal microstructure causes a complex, multi-lobed far field pattern that is unsuitable for coupling to single mode fibers or a photonic circuit of any kind (see Fig. 2.5). It became apparent early on in my PhD that radically new strategies had to be developed in order to circumvent these problems.

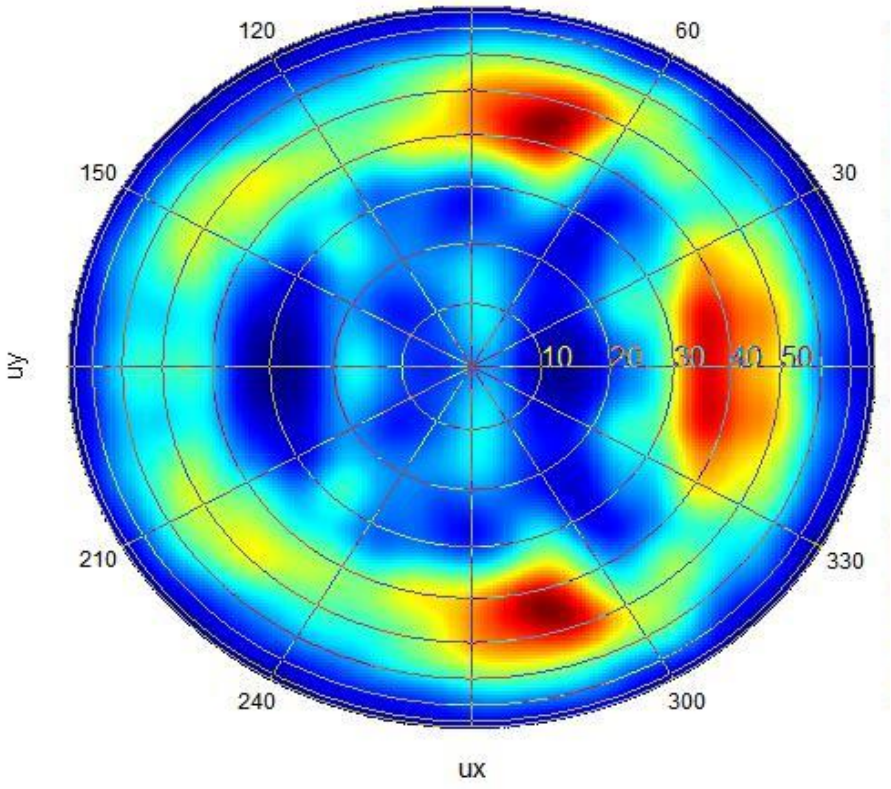


Figure 2.5: FDTD simulation of the far field profile of a back-etched PQD structure, calculated at a typical emission wavelength of 865 nm.

2.3 Post-growth sample processing techniques: polishing

Chemo-mechanical planarization (CMP) is a simple way to get rid of the vestigial recess and move back to a planar geometry, which in turn would allow to use on Pyramidal quantum dots the plethora of processing techniques developed for more conventional dots families.

In all of our experiments, samples were bonded using wax on a glass slide, and subjected to CMP on a Logitech PM5 grinder/polisher equipped with a Silicon Carbide polishing plate, while a slurry containing 70 nm silicon dioxide nanoparticles (Eminess 2EX) provided the abrasive effect.

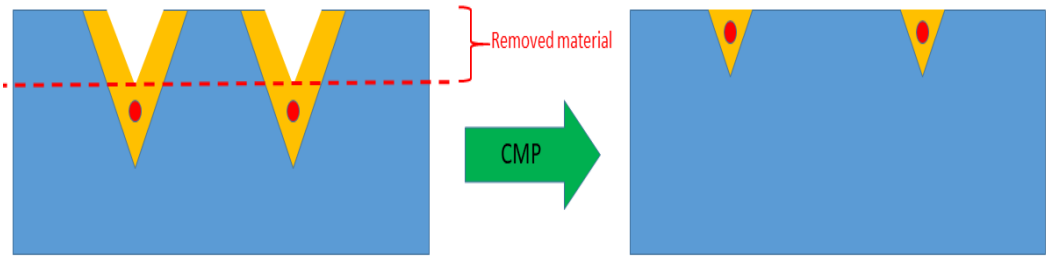


Figure 2.6 sketch of the CMP process used to remove the vestigial recess

Periodic inspection using an optical microscope showed a clear shrinking of the recess, and the process was repeated until a perfectly flat surface was obtained: it should be noted that given the small size of the nanoparticles of the polishing slurry, the resulting surface finish is of high quality, and very limited scattering and light trapping can be expected at the interface. Moreover, the epitaxially-grown layer can still be located via simple optical inspection due to high contrast of the AlAs/AlGaAs layer usually employed as an etch-stop during back-etching and GaAs: this implies that the position of individual quantum dots can still be correctly identified without the need for additional alignment marks, as can be seen in figure 2.7.

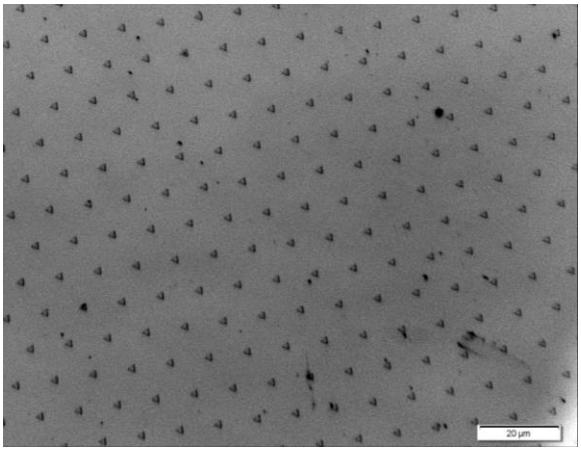


Figure 2.7 Optical microscope image showing the surface of a polished sample. The triangular base of the inverted tetrahedron can be clearly seen

Investigation using micro-PL of samples processed via this polishing approach showed an overall improvement of the spectral quality of the dots and a far greater uniformity across the sample, although the brightness remained rather limited, and still inferior to the one obtained via back-etching as one would expect. The greater uniformity and improved spectral quality we obtained are an indication that the back-etching process generally results in (chemical) surface damage, which in turn is likely to generate free and trapped charges negatively influencing the photoluminescence quality.

Poor extraction of light from high-refractive index semiconductors is usually due to an interplay of two effects. On one side, the high refractive index contrast between the semiconductor and air (or vacuum) is very high, leading to a rather small critical angle: total internal reflection causes all the light reaching the interface at a steeper angle to be entirely reflected back into the substrate. On the other side, only a fraction of the light which is extracted from the semiconductor can be in practice collected, due to the finite numerical aperture of the objective employed.

On possible solution is the use of a solid immersion lens: this mitigates the former problem, by reducing the refractive index contrast at the interface, but even more importantly affects the far field, and thus improves collection efficiency.

Indeed, experiments performed using our QDs and 1mm-wide superhemispherical (Weierstrass) glass lenses, glued using thin layers of SU-8 resist or optical adhesives (Norland NOA 61) showed a significant boost of light extraction efficiency, which becomes comparable, if not even slightly superior, to the one achievable with back-etched samples (fig. 2.8), but without the drawbacks of the latter approach.

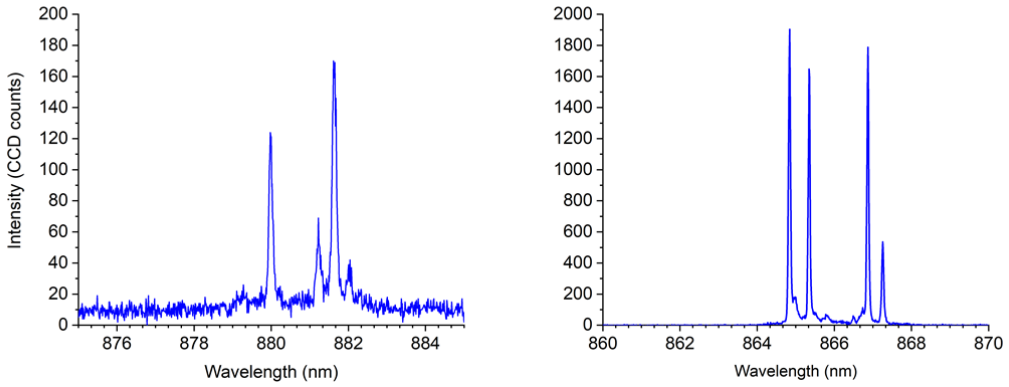


Figure 2.8 Micro-PL spectrum of polished samples. Left, without a SIL and an integration time of 5 seconds, right with a SIL and an integration time of 1 second. The sample with the SIL is almost 50 times brighter

While the total brightness still remained much below what is obtained by other groups that employ more sophisticated strategies, it soon became clear that moving away from the original pyramidal shape and the limits of conventional processing approaches could be the key to push applications of PQDs much further.

2.4 Typical spectral features of quantum dots under optical excitation

A typical semiconductor quantum dot possesses a large number of different bound states that are potentially optically active. The ones which are usually seen in a typical spectra from our QDs are the following:

- **Exciton(s)**: an exciton is a quasi-particle formed by an electron and a hole paired together and subjected to mutual electrostatic interaction. There are in total four different excitonic states, due to the different arrangements of their spins. In the simplest picture, these are two sets of double degenerate states: one pair has a total angular momentum J=1, and is thus optically active, as transition to the ground state is allowed by spin-selection rules. The other pair, dubbed dark excitons, is instead made by very long-living states due to the transition to the

ground being spin-forbidden, and are usually not observed in photoluminescence spectra.

However, reality is a little more complex, as degeneracy between the excitonic states is often removed, leading to the appearance of a fine-structure splitting (FSS): the most elegant way to understand this is by using Noether's theorem, which highlights how the lifting of a degeneracy is the consequence of the breaking of a symmetry. Anisotropies in the shape of a quantum dot, composition of the barriers, or other causes of asymmetry in the confining potential such as strain or electric fields concur to determine the magnitude of said FSS, whose values can reach tens of μeV.

- **Trions**: trions are excitons paired with either an electron (negative trion, or X^-), or a hole (X^+).
- **Biexciton**: a biexciton is an excited state made up of two electrons and two holes. It has a total angular momentum J=0

Conservation of total angular momentum, exemplified in optical selection rules, implies that recombination of excited states can happen only via the emission of a single photon, exactly like it would for an individual atom, thus implying that quantum dots can indeed be excellent single photon sources.

Even more interestingly however, conservation of angular momentum results in the possibility of emitting (polarization) entangled photon pairs via a mechanism known as the biexciton-exciton recombination cascade[12].

If we consider for simplicity a situation where there is no fine structure splitting, so that the two (bright) excitonic states are perfectly degenerate and a quantum dot which is prepared in a biexcitonic state |XX>, direct radiative recombination to the ground state is not allowed by angular momentum selection rules for single photon transitions, so that the recombination will

happen via two transitions taking place in sequence. A first transition, accompanied by the emission of a photon, will bring the quantum dot in a superposition of the excitonic states, while a second transition will relax the system in its ground state. The relationship between the polarizations of the two photons can be intuitively understood via a semi-classical model based on the conservation of angular momentum: as both the initial (|XX>) and final ground state have J=0, the sum of the angular momentum carried away by the two photons should be zero, so that if the first emitted photon is measured to have a spin angular momentum component of +ħ (left circular polarization), the second is expected to have an angular momentum of -ħ (right circular polarization) and vice versa, so that the state of the photon pair, prior to the measurement, can be written as

$$|\psi>=\frac{1}{\sqrt{2}}(|L_{XX}R_X>+|R_{XX}L_X>)$$

Or, in a linear basis

$$|\psi>=\frac{1}{\sqrt{2}}(|H_{XX}H_X>+|V_{XX}V_X>)$$

Which implies that the two photons are *polarization entangled*.

The aforementioned problem of fine structure splitting tends to break the simple picture we have discussed so far, and spoils entanglement as discussed by Stevenson in his seminal paper[13]. One of the following chapters is dedicated to this problem, and we will not discuss here the mechanism by which entanglement is degraded to avoid unnecessary repetitions. It is however important to remark how one of the most effective mitigation strategies that is employed to reduce FSS and improve the quality of entangled photons emission is to use quantum dots grown on high symmetry planes such as 111A and 111B[14,15]: indeed, our system falls in this category, and InGaAs pyramidal quantum dots usually display quite small values of excitonic fine structure

splitting of only a few μeV on average, which makes them suitable for entangled photon emission. In fact, theory predicts that as the QD is expected to inherit the C_{3v} symmetry of the tetrahedral growth template, there should be no contribution from shape anisotropy to the FSS[6,16,17].

2.5 Excitation schemes

There are two ways to generate excited states in a quantum dot: electrically and optically. Electrical pumping is the most attractive approach from an engineering standpoint, as it entails the possibility of using quantum dots as active sources in proper scalable quantum circuits. Efforts to achieve electrical pumping have been rewarded with remarkable results, but besides the fabrication complexity of this class of devices, there is usually a very poor control on the nature of the excited state which is being generated via charge injection.

Optical pumping on the other hand, while being a technique which is further away from large scale technological and commercial applications, has a far greater flexibility, and allows for the initialization of a desired state for the quantum dots. The name optical pumping is actually an umbrella name for several techniques which target different states, the most notable of whom will now be briefly discussed along with their advantages and disadvantages:

- **Non-resonant pumping**: by far the simplest approach, this technique consists of the irradiation of the quantum dot with a laser (continuous wave or pulsed) operating at a wavelength shorter than the one corresponding to the bandgap of the substrate material. This generates a large amount of charges in the surroundings of the quantum dot, which then diffuse and get trapped within its potential well, relaxing to one of the QD's excited states by exchanging energy with its surroundings. For Stranski-Kranstanov dots, excitation of the wetting layer (i.e. the thin planar layer epitaxially grown before the nucleation

of the dot) falls under this category as well. The downside of this approach is obviously the lack of any control whatsoever on the states that are generated, the introduction of a jitter (i.e. a temporal delay between the laser pulse and the initialization of the excited state) due to the feeding mechanism and the creation of a rather noisy environment due to the large number of charges generated around the quantum dot, which can in turn give rise to a broadening of the transitions' linewidths via Stark Shift (and thus a reduction of indistinguishability) and interfere with the recombination cascades.

- **Quasi-resonant pumping**: also called P-shell pumping, it allows for the direct generation of charges within the quantum dot by tuning the laser frequency in resonance with a transition between the ground state and an excited state that lies above the target one. This allows the population of the latter via conventional radiative or non-radiative recombination processes, significantly reducing the temporal jitter and improving indistinguishability.

- **Resonant excitation of the excitonic state:** as transitions between the ground state and the bright excitonic ones are dipole-allowed, using a laser of the right frequency allows for a direct population of the X state. However, decoupling the emission of the quantum dot and excitation laser becomes a significant challenge as no spectral filtering is possible: using a linearly polarized excitation and a cross-polarizer in the detection line to suppress the laser is an option, but it also causes the loss of 50% of the emission from the QD. It is possible to separate the direction of the emission and that of the excitation laser by employing waveguides, but only at the price of a greater fabrication complexity. A simpler solution is to have a phonon-assisted process, where the

frequency of the laser is tuned to be slightly higher than that of the ground to X transition.

- **Resonant excitation of the biexcitonic state:** the ground to XX transition is not allowed by dipole-selection rules for single photon events, so there is no way it can be achieved via the absorption of a single photon, even if the latter's energy perfectly matches that of the |XX> state. The biexciton can however be populated via a two-photon process (TPE), which as such requires a significant power due to the far smaller two photon cross section. On the other hand, as the frequency of the laser will be tuned to that of a virtual level between the ground and |XX> state, spectral discrimination of the signal from the excitation pulse will be possible, and no polarization filtering will be required: this is obviously pivotal for the generation of polarization entangled photons.

  A variation of this approach is a *phonon assisted* resonant excitation of the biexcitonic state, where a detuning of the laser frequency is introduced so that population of the |XX> state is achieved thanks to the interaction of acoustic phonons with the generated carriers.

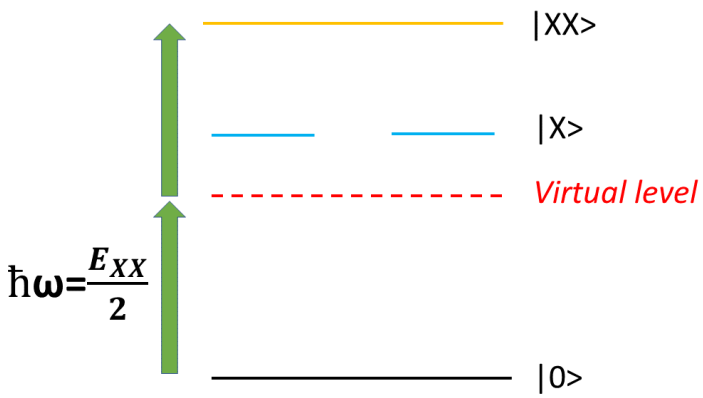


Figure 2.9: Sketch of a 2 photon resonant pumping excitation scheme

The two hallmarks of resonant pumping are *spectral cleanliness* and *Rabi oscillations*.

With spectral cleanliness we indicate the disappearance from the QD's emission spectra of all features originating from other transitions besides the ones directly involved in the pumping scheme and relaxation of the generated states, while Rabi oscillations indicate the behavior of the excited population as a function of the pulse's pump area. For a generic two level system coherently driven by a continuous laser, solution of the time-dependent Schrodinger equation will yield, in the so-called strong field regime, an oscillating function for the probability of the state being in the excited level:

$$|C_{upper}(t)|^2 = \alpha * sin^2\left(\frac{\omega t}{2}\right)$$

Where ω is called the Rabi frequency: in our case, we would be interested in initializing the system in a specific state, and then let the system relax, meaning that pulses will be used in place of a continuous wave. In order to deterministically prepare the system, the pulse area must be properly chosen: a pulse having the optimal amplitude and duration, so that the system will be brought in the target excited state with unitary probability is called a π-pulse, as it would intuitively correspond to the situation where ωt=π in the continuous wave case.

It is obvious that for any advanced quantum protocol or even practical application resonant pumping is a fundamental requirement, as it allows an on demand generation of the single photon to be used as a qubit, or of an entangled photon pair, without the issues related to the jitter intrinsic of non-resonant excitation schemes.

However, while pyramidal InGaAs quantum dots have in the past proven to be promising sources of single and most notably entangled photons, issues arise when a resonant pumping is attempted, as they have an *antibinding* biexciton, whose energy with respect to the ground state of the system is more than twice that of a single exciton. This complicates preparation of the biexcitonic state via photon excitation, as the virtual level will be lying above (and close to) the excitonic one, meaning that a phonon assisted process can populate the intermediate excitonic state (fig. 2.10), and will be in competition with the former excitation scheme[18].

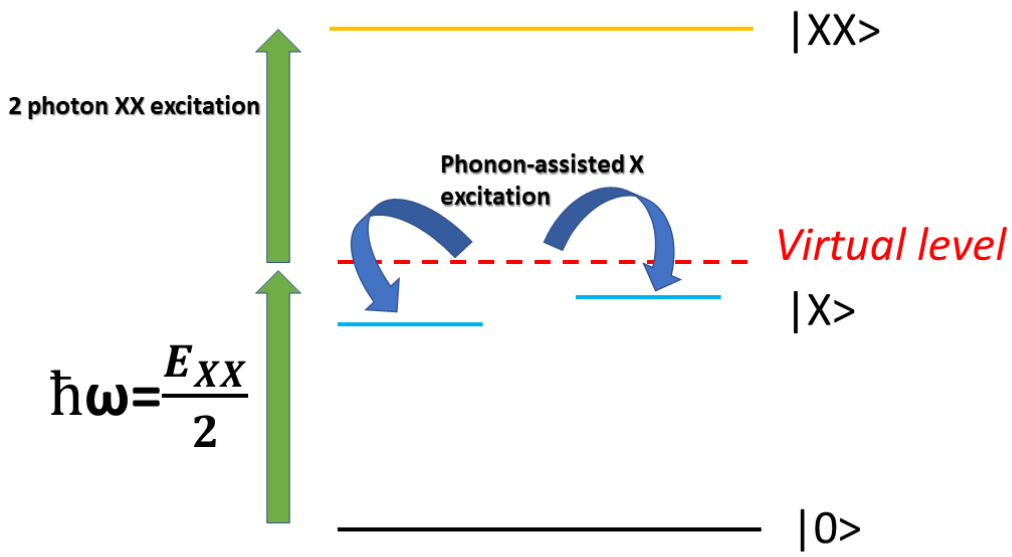


Figure 2.10: Competing excitation mechanisms in quantum dots with an antibinding biexciton. 2 photon excitation of the XX state is competing with a phonon assisted population of the intermediate X states.

Since the cross-section for a two photon process is usually rather small, phonon assisted population of the exciton tends to become the dominant excitation pathway, thus preventing on demand generation of entangled photon pairs.

In order to solve this fundamental problem, several routes were followed. The first attempt was based on the stacking of multiple dots to create so-called QD

molecules: a feat that is greatly simplified in our system in view of the deterministic positioning of the dots along the axis of the tetrahedron during growth. It was shown that these systems exhibit a variation of the binding energy of the biexciton as a function of the parameters of the structure[19,20], such as thickness and distance of the dots, and that samples can be produced with a binding energy that is close to zero, or whose biexcitons' character switches from antibinding to binding, although the reason for this behavior has not been fully explained at the time of this thesis being written.

While this approach proved successful in producing samples with at least a sizeable fraction of dots having a binding biexciton, it failed to produce values of the binding energy that were good enough to straightforwardly achieve resonant pumping, as beside the fundamental issue we have described, there are practical ones related to the need of suppressing the laser used to excite the system. Polarization filtering is obviously not compatible with the generation of polarization entangled photons, which is our main goal, and the geometry of the sample prevents us from achieving a spatial separation of the excitation signal and of the QD's emission. The only possibility is to perform a spectral filtering, for instance using optical notch filters, but that requires that the spectrum of the laser pulse and the transitions of interest are separated enough to allow for the former to be filtered out.

2.6 Development of GaAs in AlGaAs and GaAs in superlattice barriers dots

A family of dots that has proved time and again to be very suitable for resonant pumping is represented by droplet etched GaAs dots with AlGaAs barriers[21,22]: these can be fabricated via Molecular Beam Epitaxy (MBE) by filling via epitaxial growth of GaAs a nanohole etched by an Aluminium droplet on an AlGaAs substrate, and then fabricating an overlayer that acts as a top barrier. It would be tempting to draw a comparison between the growth inside one of

our tetrahedral recesses and the infilling of a nanohole, but the physics of the two growth process are quite different, as is the resulting morphology of the outcome.

As discussed before, growth of PQDs via MOVPE on large tetrahedral recesses is a complex process whose result is determined by an interplay of reaction kinetics and diffusion of the various species on the tetrahedral sidewalls: growth models predict the arising of compositional gradients when ternary alloys are grown, which determine the formation of the various nanostructures interconnected to the dot. In the case of AlGaAs growth, the concentration of Al tends to be lower the closer to the growth axis, resulting in the formation of a vertical quantum wire which, if a GaAs dot is to be grown between AlGaAs barriers, provides the confining potential in the vertical direction: since the quantum wire doesn't have the typical "core-shell" structure, but displays a smooth change of the Al concentration, the confining potential is far from homogeneous, and is expected to be stronger on the sides of the quantum dot and smaller towards the center, where the wavefunctions might penetrate more inside the barriers, whose varying composition might be an additional source of fine-structure splitting. Nevertheless, GaAs pyramidal quantum dots are expected to have a much larger confinement than their InGaAs counterparts, due to the increased height of their barriers, even when leaking effects are taken into account.

Also, the stoichiometry of the barriers can indirectly affect the lateral size of the dot if their thickness is sufficient: the interplay of the various factors that affect growth of ternary alloys determines the base width of the growth profile in equilibrium conditions, that is, after transients due to stoichiometry changes have been resolved (fig. 2.11).
Growth models indicate that a higher Al content will result in a smaller lateral size of the growth profile, and thus yield more tightly confined dots.

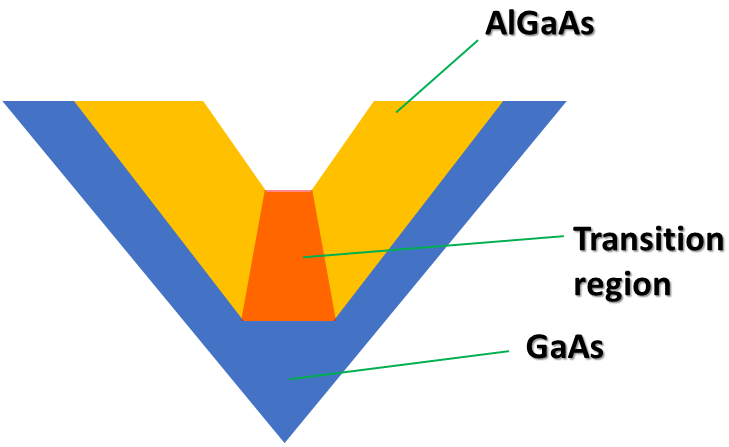


Figure 2.11 Evolution of the base width of the growth profile when the growth is switched from GaAs to AlGaAs

The typical structure of a GaAs pyramidal quantum dot sample is reported in Table 1: the first layer to be grown is a thick buffer that takes advantage of the relatively large amount of epitaxial material that the tetrahedral recess can accommodate to increase the distance between the region containing the quantum dot and the wet-etched surfaces. An AlAs (or AlGaAs with high Al content) layer is subsequently grown to behave as an etch stop layer during the final chemical etch step used to expose the pyramids, as discussed before. The large thickness of the first $\mathrm{Al_xGa_{1-x}As}$ barrier, 100 nm, is chosen not only to provide the confinement effect, but also so that the transient evolution of the self-limited growth profile is completed (see Fig 2.11), and the lateral size of the dot is determined by the selected stoichiometry of the $\mathrm{Al_xGa_{1-x}As}$ alloy.

Table 1: typical structure of a GaAs/AlGaAs PQD sample

	Material	Nominal Thickness (nm)	Growth temperature (°C)
Buffer	GaAs	160	770
Etchstop	AlAs	60	770
Spacer	GaAs	50	730
Barrier	$Al_xGa_{1-x}As$	100	730
QD	GaAs	0.07-1	730
Barrier	$Al_xGa_{1-x}As$	70	730
Cap	GaAs	70	730

GaAs dots with AlGaAs barriers were grown both in 7.5 as well as in 10 µm tetrahedral holes, and exhibited very uniform and reproducible spectral features, most notably a surprisingly constant biexciton binding energy across a single sample: while fluctuations intrinsic to epitaxial growth are exacerbated by the sensitivity of quantum emitters to the environment, and yield different spectra for different quantum dots, it looks like the energy difference between the biexciton and exciton photon remains the same, as shown in fig. 2.12a.

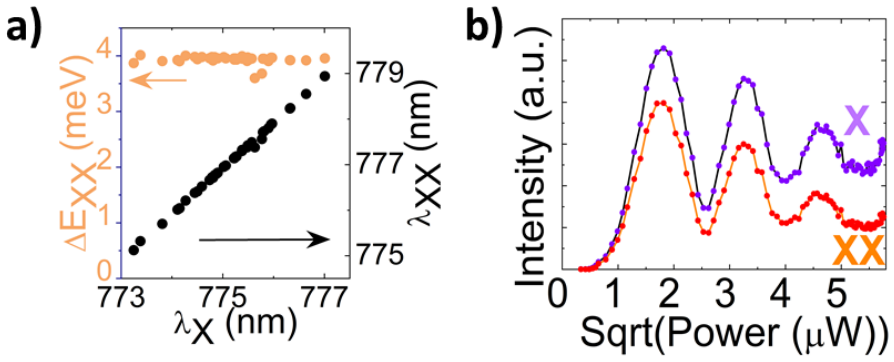


Figure 2.12: a) emission wavelength for biexciton and exciton photons for various quantum dots, and corresponding binding energies. B) Rabi oscillation displayed by GaAs dots under 2 photon resonant excitation of the biexciton.

This welcomed feature, coupled with the relatively large values of the (positive) binding energy, makes this family of dot particularly suitable for resonant pumping, which was indeed successfully attempted both by our group and Prof. Trotta's group in Rome[23], as proven by the clear Rabi oscillations reported in fig. 2.12b and by the clean spectrum in figure 2.13 where a comparison is shown with the spectrum of the same dot when non-resonant excitation is attempted with a red (633 nm) laser. However, figure 2.12b also shows that the amplitude of the Rabi oscillations of the XX and X transitions are not the same, as would usually be expected: since the two curves clearly indicate that the power dependence is the same and suggest that photons are indeed coming from the biexciton-exciton cascade after resonant population of the XX state, this behavior can be attributed to some mechanism causing a non-radiative de-excitation of the biexciton, rather than to a resonant population of the excitonic state as for InGaAs dots.

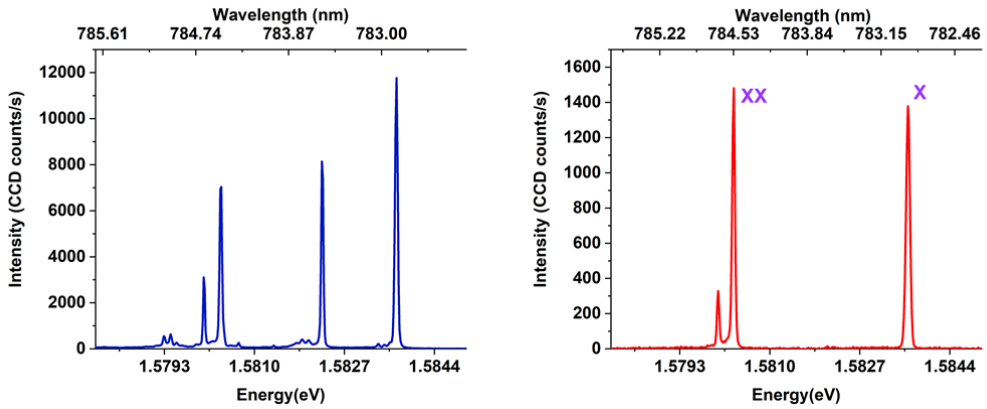


Figure 2.13 Emission spectrum of a GaAs quantum dot under non-resonant (left) and 2 photon resonant excitation (right)

Temporal resolved photoluminescence also indicated a short lifetime of roughly 500 ps and 220 ps for the exciton and biexciton states respectively. However, the large values of excitonic fine structure splitting displayed by

GaAs dots (several tens of μeV) are hardly compensated by such relatively short lifetimes, and make them unsuitable as sources of polarization entangled photons. The cause of such a large FSS is likely to be found in the vertical quantum wire being responsible for vertical confinement, as the latter exhibits a far from uniform composition in the plane as discussed before, and likely exacerbates the impact of alloy fluctuations in the barrier regions.

Interestingly however, a clear trend was observed for the FSS when changing the thickness of the QD in the growth direction, with the former getting smaller as the dot was getting thinner: this looks counterintuitive, as it would cause an increased leaking of the wavefunction in the barrier layers, which would in turn increase the sensitivity to alloy fluctuations. It is possible however that this was compensated by a diminished exchange integral, due to a lesser superposition of the excitonic wavefunctions.

A better approach is the use of a digital alloy, also called a superlattice, for the barriers of the dot: this is grown by alternating very thin layers of GaAs and AlAs, and removes the anisotropy of ternary alloy growth while still allowing for a confining effect to take place, since the resulting material will still have a larger bandgap than GaAs.

The typical structure of a sample with superlattice barriers is reported in table 2: the outer barrier layers allow to adjust the lateral size of the dot, and provide additional protection during the chemical etch step in case the etch stop layer fails. The growth is further terminated with a very thin GaAs layer to protect the underlying AlGaAs layers from oxidation in the atmosphere.

Indeed, superlattice dots proved a quite successful endeavor, and displayed both reasonable values of fine structure splitting and spectral features that allow to achieve resonant pumping.

	Material	Nominal Thickness (nm)	Growth temperature (°C)
Buffer	GaAs	60	770
Etchstop	AlAs	40	770
Spacer	GaAs	100	730
Outer barrier	$Al_{0.55}Ga_{0.45}As$	70	730
Outer barrier	$Al_{0.45}Ga_{0.55}As$	90	730
Superlattice barrier	AlAs GaAs	25 repetitions: 0.2 nm 0.2 nm Total thickness: 10 nm	730
QD	GaAs	0.65	730
Superlattice barrier	AlAs GaAs	25 repetitions: 0.2 nm 0.2 nm Total thickness: 10 nm	730
Outer barrier	$Al_{0.45}Ga_{0.55}As$	60	730
Outer barrier	$Al_{0.55}Ga_{0.45}As$	70	730
Cap	GaAs	1	730

Table 2 Typical structure of a dot with superlattice barriers

A final approach is to get rid of any complex material in the barriers entirely, by using AlAs instead of AlGaAs or superlattices, and if needed tune the emission energy by changing the size of the dot. Since all alloys in this case are binary, a very small FSS was expected, but while results did confirm that the FSS was relatively small, it was still on average of a few μeV: roughly of the same magnitude found in InGaAs/GaAs dots, where the wavefunction is actually confined in a ternary alloy, and of the one exhibited by dots confined by a superlattice. This behavior is quite surprising, and no explanation has so far been produced: the small lattice mismatch between GaAs and AlAs seems to rule out strain as a potential source of asymmetry, but results obtained via TEM suggest that it is quite difficult to grow AlAs on the base of the growth profile, and the resulting layer might be thinner and more disordered than expected, leading to a significant leakage of the wavefunctions into the AlGaAs outer layers (see chapter 7). As such, it might be possible to further improve this family of dots by increasing the thickness of the AlAs barriers.

A summary of the results obtained by our group for the various families of GaAs dot is reported in figure 2.14 for the reader's convenience.

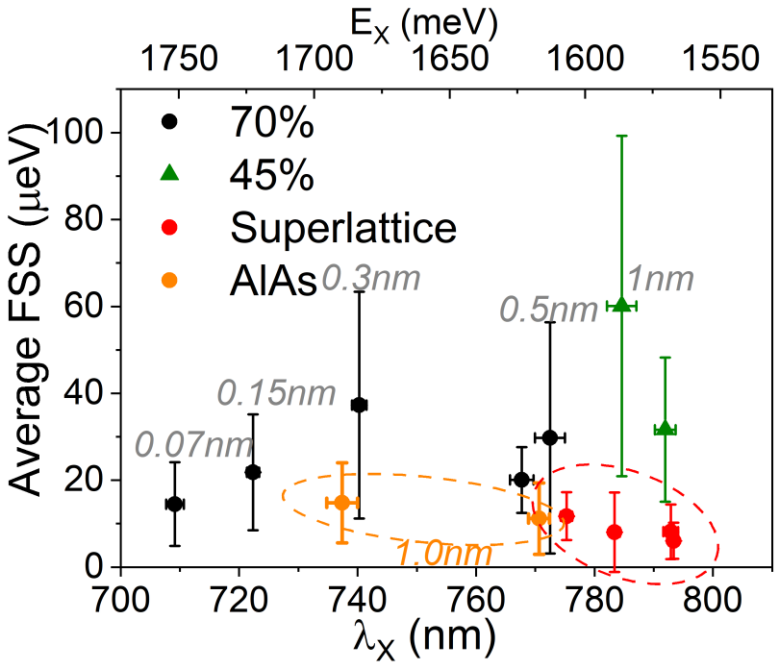


Figure 2.14 Comparison of FSS distribution for pyramidal GaAs quantum dots with different confining barriers

1. Juska, G., Dimastrodonato, V., Mereni, L. O., Gocalinska, A. & Pelucchi, E. Towards quantum-dot arrays of entangled photon emitters. *Nat. Photonics* **7**, 527–531 (2013).

2. Dimastrodonato, V., Pelucchi, E. & Vvedensky, D. D. Self-Limiting Evolution of Seeded Quantum Wires and Dots on Patterned Substrates. *Phys. Rev. Lett.* **108**, 256102 (2012).

3. Pelucchi, E., Moroni, S. T., Dimastrodonato, V. & Vvedensky, D. D. Self-ordered nanostructures on patterned substrates. *J. Mater. Sci. Mater. Electron.* **29**, 952–967 (2018).

4. Dimastrodonato, V., Pelucchi, E., Zestanakis, P. A. & Vvedensky, D. D. Morphological, compositional, and geometrical transients of V-groove quantum wires formed during metalorganic vapor-phase epitaxy. *Appl. Phys. Lett.* **103**, 042103 (2013).

5. Ducommun, Y. *et al.* Structure and optical properties of V-groove quantum wire superlattices. *Phys. E Low-dimensional Syst. Nanostructures* **2**, 954–958 (1998).

6. Hartmann, A., Ducommun, Y., Leifer, K. & Kapon, E. Structure and optical properties of semiconductor quantum nanostructures self-formed in inverted tetrahedral pyramids. *J. Phys. Condens. Matter* **11**, 5901–5915 (1999).

7. Juska, G. *et al.* Conditions for entangled photon emission from (111)B site-controlled pyramidal quantum dots. *J. Appl. Phys.* **117**, 134302 (2015).

8. Helfrich, M. *et al.* Investigation of pre-structured GaAs surfaces for subsequent site-selective InAs quantum dot growth. *Nanoscale Res. Lett.* **6**, 211 (2011).

9. Luo, J. W., Singh, R., Zunger, A. & Bester, G. Influence of the atomic-scale structure on the exciton fine-structure splitting in InGaAs and GaAs quantum dots in a vertical electric field. *Phys. Rev. B - Condens. Matter Mater. Phys.* **86**, 161302 (2012).

10. Singh, R. & Bester, G. Lower bound for the excitonic fine structure splitting in self-assembled quantum dots. *Phys. Rev. Lett.* **104**, 196803 (2010).

11. Chung, T. H. *et al.* Selective carrier injection into patterned arrays of pyramidal quantum dots for entangled photon light-emitting diodes. *Nat. Photonics* **10**, 782–787 (2016).

12. Yamamoto, Y., Santori, C. & Pelton, M. Regulated and entangled photons from a single quantum dot. *Phys. Rev. Lett.* **84**, 2513–2516 (2000).

13. Stevenson, R. M. *et al.* Evolution of entanglement between distinguishable light states. *Phys. Rev. Lett.* **101**, 170501 (2008).

14. Basso Basset, F. *et al.* High-Yield Fabrication of Entangled Photon Emitters for Hybrid Quantum Networking Using High-Temperature Droplet Epitaxy. *Nano Lett.* **18**, 505–512 (2018).

15. de Boer, S. K., van Dorp, W. F. & De Hosson, J. T. M. Charging effects during focused electron beam induced deposition of silicon oxide. *J. Vac. Sci. Technol. B, Nanotechnol. Microelectron. Mater. Process. Meas. Phenom.* **29**, 06FD01 (2011).

16. Abbarchi, M. *et al.* Fine structure splitting of quantum dot excitons: Role of geometry and environment. *Phys. E Low-Dimensional Syst. Nanostructures* **42**, 881–883 (2010).

17. Dupertuis, M. A. *et al.* Symmetries and the Polarized Optical Spectra of

Exciton Complexes in Quantum Dots. *Phys. Rev. Lett.* **107**, 127403 (2011).

18. Juska, G. *et al.* Biexciton initialization by two-photon excitation in site-controlled quantum dots: The complexity of the antibinding state case. *Appl. Phys. Lett.* **117**, 134001 (2020).

19. Moroni, S. T., Chung, T. H., Juska, G., Gocalinska, A. & Pelucchi, E. Statistical study of stacked/coupled site-controlled pyramidal quantum dots and their excitonic properties. *Appl. Phys. Lett.* **111**, 083103 (2017).

20. Moroni, S. T. *et al.* Vanishing biexciton binding energy from stacked, MOVPE grown, site-controlled pyramidal quantum dots for twin photon generation. *J. Cryst. Growth* **506**, 36–39 (2019).

21. Gurioli, M., Wang, Z., Rastelli, A., Kuroda, T. & Sanguinetti, S. Droplet epitaxy of semiconductor nanostructures for quantum photonic devices. *Nature Materials* vol. 18 799–810 (2019).

22. Huber, D. *et al.* Highly indistinguishable and strongly entangled photons from symmetric GaAs quantum dots. *Nat. Commun.* **8**, 15506 (2017).

23. Jahromi, I. R. *et al.* Optical properties and symmetry optimization of spectrally (excitonically) uniform site-controlled GaAs pyramidal quantum dots. *Appl. Phys. Lett.* **118**, 073103 (2021).

3 Advanced processing strategies for pyramidal quantum dots: fabrication of site-controlled 3D dielectric structures using Electron Beam Induced Deposition

This chapter covers the applications of the EBID fabrication technique to the field of solid state quantum light sources we have investigated in conjunction with Prof. Andrea Di Falco's group, based at the University of St. Andrews, UK. It will be presented in the form of the accepted paper we have submitted reporting our investigation, which has been published on ACS Applied Nano Materials.

Planar Semiconductor Membranes with Brightness-enhanced Embedded Quantum Dots via Electron Beam Induced Deposition of 3D Nanostructures: Implications for Solid State Lighting

*Simone Varo[1] *‡, Xin Li[2]‡, Gediminas Juska[1], Iman Ranjbar Jahromi[1], Agnieszka M. Gocalinska[1], Andrea Di Falco[2] and Emanuele Pelucchi[1]*

1 Tyndall National Institute, University College Cork, Dyke Parade, Cork, T12R5CP, Republic of Ireland

2 SUPA, University of St. Andrews, School of Physics & Astronomy, Physical Science Building, North Haugh, St Andrews, KY16 9SS, United Kingdom

* simone.varo@tyndall.ie

KEYWORDS: Quantum dots, Electron Beam Induced Deposition, Microlenses, Additive Manufacturing, Photonic trimming.

ABSTRACT

The engineering of the surrounding photonic environment is one of the most successful approaches routinely used to increase light extraction efficiency and tune the properties of solid state sources of quantum light. However, results achieved so far have been hampered by the lack of a technology that allows for the straightforward fabrication of large scale 3D nano- and microfeatures, with very high resolution and sufficient flexibility in terms of available materials. In this paper we show that Electron Beam Induced Deposition can be a very promising approach to solve this issue, as exemplified by the fabrication of Pt and SiO_2 nanofeatures on a membrane containing ordered arrays of site-controlled pyramidal quantum dots. Micro-photoluminescence has been used to compare the emission of the dots before and after the deposition of the structures, remarkably showing both a significant increase in the light extraction efficiency and no degradation of the spectral quality, implying that negligible damage has been caused to the emitter due to the deposition process. This paves the way for novel post-growth processing strategies for epitaxial quantum dots used in both quantum information technologies and lighting applications.

Introduction

Epitaxially grown semiconductor quantum dots (QDs) have emerged over the last decade as extremely promising sources of non-classical light[1] due to their high quantum yield, single photon purity and indistinguishability[2], capability of emitting entangled photons via the biexciton-exciton recombination cascade[3] and possibility to achieve electrical pumping[4,5].

However, the high refractive index of the semiconductor host matrix usually severely limits the brightness of the source due to total internal reflection, making it incompatible with any of the envisioned practical applications[6]. Moreover, the combined requirement to engineer both the properties of the emitter[7] and its interface with the surrounding photonic circuitry[8] call for sophisticated fabrication approaches: major milestones have been achieved

by the community by embedding QDs within micropillar cavities[9,10,11], 2D photonic crystals[2], photonic nanowires[12], circular Bragg gratings[13], nanotrumpets[14], and by fabrication of site-controlled microlenses[15,16] on top of the semiconductor matrix. All of these approaches are usually based on multi-step processes that require locating a QD using micro photoluminescence[17,18] or cathodoluminescence[15], the definition of alignment marks and the top-down fabrication of the photonic nanostructures via electron beam lithography: the change of the exposure dose, as its customary in greyscale lithography, can allow for the fabrication of simple 3D features such as microlenses, while multi-photon optical lithographic techniques can create much more complex structures, but at the price of a lower resolution.

It is clear that the limits of the techniques employed so far have prevented the fabrication of arbitrary 3D micro- and nanostructures in the proximity of QDs, and new approaches will have to be considered to overcome the current technological barriers.

In striking contrast with conventional electron beam lithography (EBL), Electron Beam Induced Deposition[19–21] (EBID) is not based on the exposure and development of an electron-sensitive resist, but is an additive technique that uses a focused electron beam to promote the decomposition of chemical precursors inserted in the gas phase within the electron microscope chamber. By means of 3D scanning of the electron beam, EBID allows for the local deposition of a target material and the fabrication of complex nanofeatures while retaining the typical resolution of EBL[22,23], with the additional benefit of a remarkable flexibility in terms of material choice: both oxides, such as SiO_2, as well as metals, such as Pt[24] and Au[25], can be deposited in a single processing run by interchanging gases. This paves the way for a direct deposition of hard masks to be used in subsequent dry etching steps, or of plasmonic[26] and dielectric nanostructures aimed at improving light extraction efficiency[27] and/or tailoring of the emitters properties[28].

Here we carry out a study on the possible applications of the EBID technique for the most widely used starting configuration of an epitaxial quantum dot sample, that is, a planar semiconductor membrane with embedded quantum dots, on top of whom we have fabricated several structures with the aim of studying the effect on the underlying quantum dots. In particular, Platinum containing structures were fabricated to investigate the possibility of achieving plasmonic resonance effects, which would however be accompanied by the introduction of undesirable ohmic losses. Dielectric structures based on SiO2 on the other hand would exhibit a more passive operation, and are expected to merely improve light extraction without providing any cavity-like effect such as the shortening of the QD's lifetime, but without introducing drawbacks.

Sample fabrication

Throughout our work we have used arrays of site-controlled pyramidal quantum dots[29,30] which can be easily located using a standard scanning electron microscope (SEM). However, it should be noted that the obtained results can be readily extended to self-assembled, and randomly distributed, Stranski-Krastanov QDs, e.g. by employing the consolidated alignment marks fabrication approach[13].

All depositions have been carried out on a sample of InGaAs in GaAs pyramidal quantum dots, grown via Metal Organic Vapor Phase Epitaxy (MOVPE) using an Aixtron 200 reactor on a (111)B GaAs substrate, patterned with inverted tetrahedra using conventional lithography and wet etching in Br:MeOH. The different decomposition kinetics of the precursors in the MOVPE reactor ensures that growth takes place preferentially on the three exposed (111)A GaAs faces of the inverted tetrahedra[31], and an interplay of kinetics and diffusion of the precursors ensures the deterministic fabrication of QDs interconnected with a series of quantum wires along the axes of the tetrahedral, if the thicknesses of the stacked layers are properly chosen.

For the sample used in this work, first a 180 nm-thick buffer layer was grown at a temperature of 770 °C, in order to increase the distance of the nanostructures of interest from the three exposed (111)A faces that were subjected to chemical etch, then a 75 nm AlAs layer was grown in order to facilitate the location of the quantum dots in the SEM due to the high contrast with GaAs. Finally, a series of three stacked $In_{0.25}Ga_{0.75}As$ quantum dots was grown at a lower temperature of 730 °C: the first two, grown with a nominal thickness of 0.4 nm, help stabilizing the environment by trapping charges generated during optical pumping along with the quantum wires that are fabricated with them, while the last one is the target QD, and is grown with a nominal thickness of 0.65 nm to ensure that its emission spectrum does not overlap with the other ones and will be the dot we will be referring to from now on.

While the epitaxial growth takes place almost exclusively inside the lithographically-defined inverted tetrahedra, the post-growth sample still retains a vestigial recess: in order to move back to the typical geometry used by the epitaxial QD community that is, a planar sample, a chemo-mechanical planarization has been carried out[32] using a 70 nm silica nanoparticle slurry (Ultra-Sol 2EX, Eminess Technologies) on a Logitech PM5 polishing machine. This ensures that the resulting surface is both flat and polished to an acceptable optical quality, with the QDs lying around 100 nm below the surface.

The sample was then placed in a Raith E-line plus EBL system for the fabrication of the nanostructures. In order to investigate the possible applications of the technique in terms of both depositable material and shapes, two series of features were fabricated above a series of QDs in this first deposition run: Pt-containing features were made by inserting the precursor $(Me_3)MeCpPt$ in the chamber, and decomposing it with a deposition current of 150 pA, accelerating voltage of 3 kV, dose of 1 C/cm^2, step size of

20 nm, and dwelling time of 50ms, with the sample nominally at room temperature, which is expected to lead to a Pt percentage of 30% in the final material[24], the rest being made up mostly by carbon. Secondly, SiO_2 based structures were fabricated by decomposing the precursor Penta Methyl Cyclo Penta Siloxane (PMCPS), with a deposition current of 150 pA, accelerating voltage of 3 kV, dose of 1 C/cm^2, step size of 10 nm, and dwelling time of 0.01ms with variable (100-5000) writing loops, again at room temperature. Chemical analysis performed using EDX spectroscopy with a Quanta 650 SEM shows the amount of carbon incorporated in the structures to be surprisingly very low and not detectable with the tool employed. A high purity of the material is however in line with what previously reported using similar deposition conditions[33]. Typical EDX spectra are reported in the Supplementary Materials on Table S2 for the reader's convenience.

A summary of the fabrication procedure employed is reported in figure 3.1.

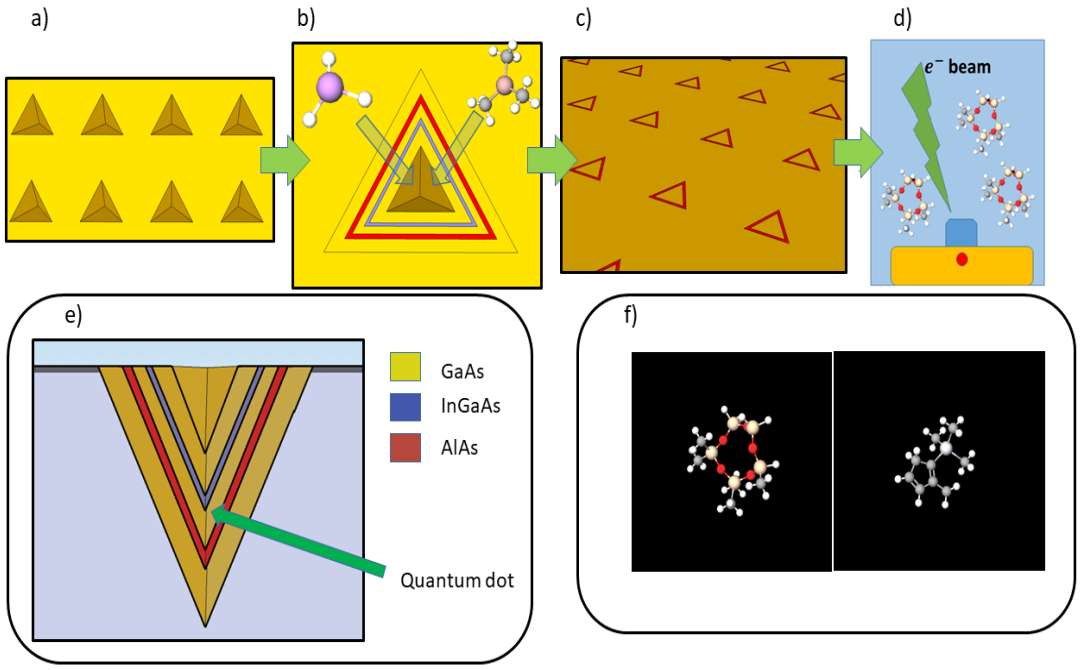


Figure 3.1 Representation of the steps in the fabrication of the samples: a) patterning of the substrate; b) MOVPE growth, organometallic precursors dissociate preferentially on the three exposed 111A faces; c) planarization; d) EBID growth; e)

cross section of the structure after MOVPE growth. The QD is formed by enclosing a thing InGaAs layer between two GaAs barriers. f) EBID precursors PMCPS (left) and (Me_3)MeCpPt (right)

A wide array of shapes, ranging from nanopillar-like adiabatically tapered waveguides to microlenses was fabricated by exploiting the 3-dimensional capabilities of the technique and in order to investigate their effects on the underlying QD. Images of each of the fabricated structures are reported in the Supplementary Materials as well (figures S1-S5), while some significant ones are included in figure 3.2 as reference.

Pt alignment marks were also fabricated to allow for an easier location and identification of the processed QDs in the subsequent micro photoluminescence (μ-PL) measurement stages: these were carried out using a confocal setup and a helium closed-cycle cryostat that cooled the sample to a temperature of 8 K. All measurements at this stage were performed under non-resonant continuous wave excitation conditions with a 635 nm wavelength laser using a 0.45 numerical aperture objective (Mitutoyo) for light collection, with an excitation power density of 150 nW/μm^2 for all the structures.

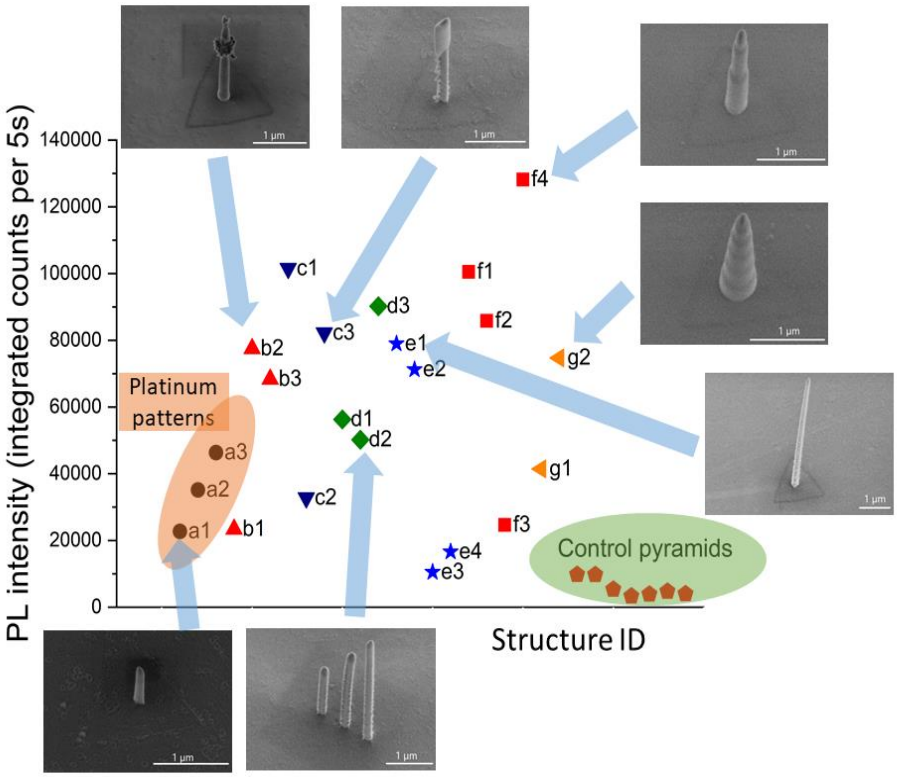


Figure 3.2. Integrated CCD counts for the QDs after the fabrication of nanostructures on top. Control QDs (without any deposited structure) are also shown for comparison. Insets display some fabricated nanofeatures.

Results and discussion

As can be seen from figure 3.2, nearly every of the fabricated structures provide a boost of the extraction efficiency when compared to the control (unprocessed) QDs.

For the three Pt-based nanopillars, (left low corner in Fig. 3.2), it is worth mentioning no significant change in the lifetime was detected, meaning that a plasmonic coupling between the quantum emitter and the deposited structure can be ruled out: this is likely due to the latter's relatively small Pt content (around 30% with the used deposition parameters), resonance frequency, as well as the distance of the buried QD from the surface that prevents efficient overlapping of the QD's dipole with the mode sustained by the antenna. As plasmonic effects have already been achieved using the same deposition

technique[28], we believe that this unsatisfactory performance can be mostly ascribed to the planarization technique hereby employed, that provides limited control over the dot's final distance from the surface.

Dielectric micro- and nano-features on the other hand have shown remarkable results, with values of the light extraction efficiency often surpassing the ones obtained from pyramidal quantum dots using the conventional back-etching technique (i.e. the conventional approach to obtain apex-up pyramids and improve extraction efficiency[34]). These structures work by changing the dielectric environment above the semiconductor, reducing internal reflection and displaying a waveguiding effect (more pronounced for the pillar-like ones) that helps not only extracting photons from the surface of the high refractive index GaAs, but also collecting it with the objective by reducing the angular distribution of the emitted light.

These results, while already proving the capabilities of this technique, can hardly be used to reach any general conclusion on the properties of each of the deposited structures as they do not take into account the differences in term of blinking and quantum yield of the QDs they were fabricated onto. Moreover, the structures themselves, by channeling and focusing light in different ways, are expected to affect the excitation efficiency of the QD lying beneath it, thus making the use of the same excitation power a rather naïve approach for a systematic comparison.

In order to address these shortcomings, we have exploited the previously deposited alignment marks to carry out the mapping of a series of 30 quantum dots, that were subsequently used for a second run of depositions (Figure 3.3): this ensured that we were able to quantitatively estimate the effect of the structures in terms of both light extraction efficiency and changes of the spectra due to defects or strain created by the deposition itself by comparing the measurements taken prior and after the in-situ fabrication had been carried out. Additional care was employed to avoid deposition nonuniformities

by simplifying the geometry of the structures, which are now simple cones of different base radii and heights, creating structures that vary from lens-like to tall pillars: the former are expected to work similarly to solid immersion lenses, while the latter is assumed to rely on leaking of a guided mode to promote light extraction In any case, as the structures are deposited on top of the GaAs layer, they are expected to merely improve the amount of light that leaves the semiconductor, while phenomena such as Purcell enhancement or re-direction of the QD's emission are negligible in this case. Geometrical parameters were also varied smoothly between the structures in order to both investigate the presence of trends in the PL enhancement and assess the reproducibility of the results via comparison of similar structures. To circumvent the aforementioned problem of different excitation efficiencies with and without the structures, during the measurements of the second set of depositions, every QD has been excited close to the saturation level of ground state-related transitions: the resulting photoluminescence spectra was composed of several excitonic complexes, the dominant ones typically being neutral exciton, biexciton, negative and positive trions, excited positive trion and positively charged biexcitons. Ideally, an identical or very similar spectral shape was recreated in every case from the corresponding QDs after the deposition of the nanostructures, indicating the same QD population conditions. Light extraction enhancement was subsequently calculated as a ratio of an integrated QD photoluminescence signal post- and prior-deposition. This technique also allowed for the overcoming of uncertainties arising due to variations in the experimental conditions, such as a different focal distance and excitation power.

Furthermore, having already proven the flexibility of the technique in terms of material choices, we have decided to narrow down the scope of our investigation to a subset of the previously investigated geometries: we have thus deposited a series of extruded SiO_2 structures whose shapes range from

dome-like to conical to pillar-like, in order to determine the effect of different base radiuses and heights. Details and images of each of the fabricated structures are once more included as Supplementary Materials (figures S6-S10) for the reader's convenience.

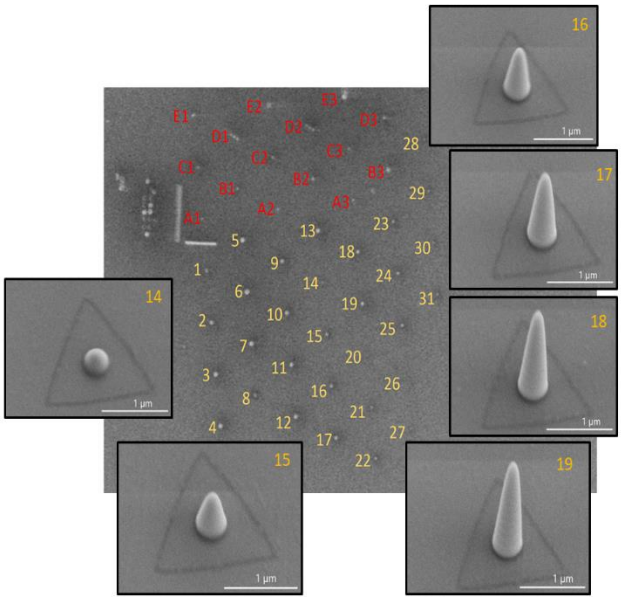


Figure 3.3. Mapping of the sites used for the fabrication of structures above the QDs and numbers identifying the single structures. The insets show some examples of the deposited structures. Alignment marks can be seen in the top left corner.

First of all, a comparison of the measurements performed before and after the deposition (figure 3.4) shows surprisingly negligible changes in the dominant spectral features, a telltale sign that the deposition technique does not, in fact, cause significant damage to the quantum dots or to the matrix they are embedded into. Minor spectral shifts, usually in the order of tens of µeV, can be attributed to either small strains field induced by the structures or to local temperature variations caused by the different heat distribution and dissipation in close proximity of the QD once the thermally insulating dielectric is deposited.

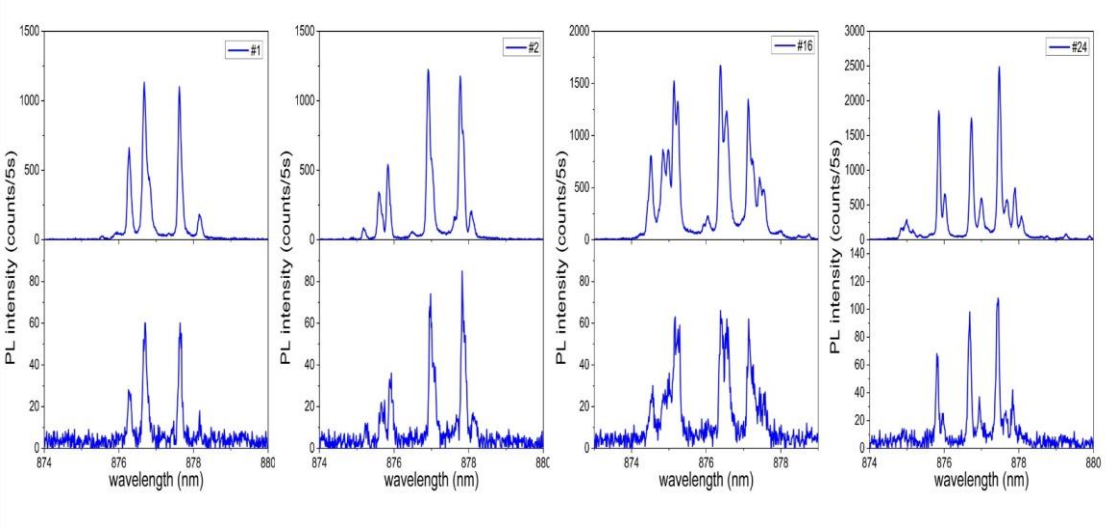


Figure 3.4. Comparison of the spectra before (bottom) and after (top) the fabrication of the structures for four randomly chosen QDs, showing negligible spectral shifts and excitonic distribution.

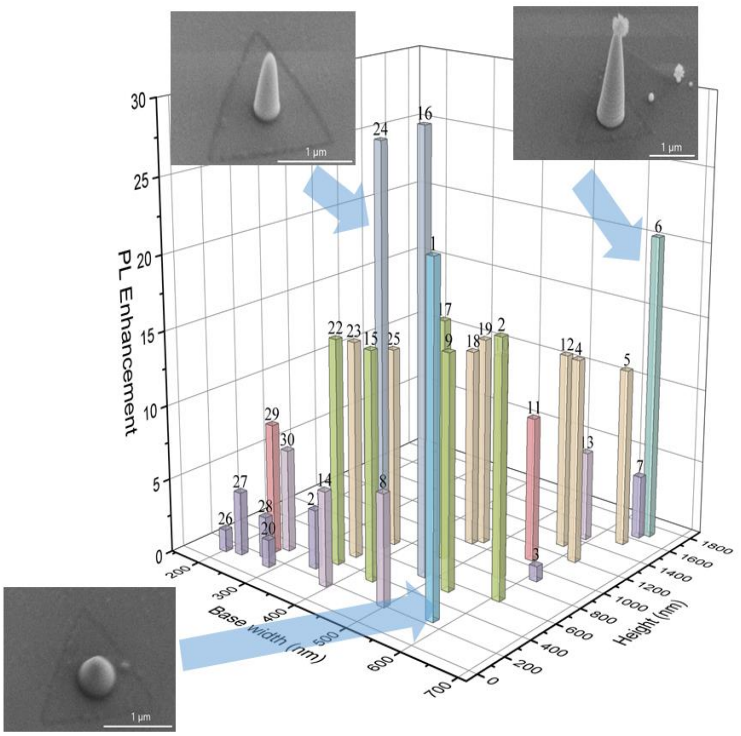


Figure 3.5. Enhancement of the brightness for the 30 deposited dielectric nanostructures with different heights and base widths. Numbers on top of the bars identify the corresponding structure, whereas the three insets show the shape of the brightest ones

The brightness of the sources is clearly increased significantly after the deposition, up to an order of magnitude or more as can be seen in figure 3.5, which summarizes the key finding of our investigation. However, the interpretation of the obtained results is not straightforward: first of all, it can be noticed that in comparison to the dome-like, low-height structures, the elongated, tapered features often provide a far more significant boost of the light extraction efficiency (LEE). Different mechanisms are likely simultaneously at play and their relative effects difficult to decouple from each other: it is intuitive that a larger base radius should allow the microstructure to collect and channel more light that would otherwise be trapped inside the semiconductor due to total internal reflection. Secondly, the shape of the microstructure affects, via Fresnel reflection at the interface and adiabatic coupling, the amount of light that leaves it, as well as the far field of the radiated light, and thus the final collection efficiency from the objective.

For the low-height, dome-like structures, it is apparent that the LEE depends more on their base size than on their aspect ratio, as one would intuitively assume due to their behavior being similar to that of lenses: in this regard, it comes to no surprise that structure number 1, having the largest base radius, provides by far the best performance, and one of the best performances overall. Similar structures such as number 14 and 18 however display a far less significant enhancement, due to their base radiuses being smaller and thus collecting less light from the quantum emitter, despite being closer in shape to a hemispherical lens. Minor displacements from the shape of an ideal micro-lens, implying that the light is emitted in a broader cone, are likely to be counterbalanced by the high numerical aperture of the objective.

It is interesting to observe that the remaining, tapered, pillar-like structures display boosts of the LEE that look relatively constant across a broad set of geometrical parameters, as clearly seen in figure 3.5, showing remarkably

coarse fabrication tolerances, albeit only two of them, number 16 and 24, manage to break the level reached by the best dielectric lens (number 1). Moreover, they usually perform better than the dome-like structures of similar base radius: this is clear when comparing for instance structures 14 and 22 or 23, and can probably be ascribed to their ability to efficiently couple light that propagates along their axes in the free space via their adiabatic tapering, as it happens with semiconductor nanopillars[35]. Surprisingly, however, structures with a larger base radius and very small aspect ratio (and thus very small tapering angle), such as number 7 or 13, actually perform worse than those with a smaller base, and a larger tapering angle.

Structure number 6, that displayed a far more significant boost of the LEE when compared to the relatively similar structures numbered 5 and 7, was affected by some fabrication imperfections (figure 3.5) that are likely to cause a scattering of the light from the tip.This might suggest that the quality of the latter plays a more fundamental role in determining the performance of these kind of structures than other geometrical parameters.

FDTD simulations

In order to better understand the effect of geometrical parameters and assess the impact of the purity of the deposited material on the performance of EBID-fabricated structures, an extensive simulation work has been performed using Lumerical FDTD.

In all of our simulations we have assumed the dielectric structure to be conical in shape, and independently varied its base radius and its height to define a matrix of 15x15 simulations, while approximating the quantum dot as a dipole located 150 nm below the GaAs/dielectric interface.

For each of said simulations, the collection efficiency by a 0.45 NA objective like the one employed in our experiment was estimated via integration of the far field, and the collection enhancement with respect to the bare GaAs

substrate was calculated by taking the ratio of the former to collection efficiency of the latter case, at a wavelength of 860 nm which is typical for our quantum dots.

Furthermore, we computed the aforementioned matrix 3 times, assuming on each run a different refractive index for the dielectric in order to evaluate the impact of carbon impurities: to do so, we estimated the refractive index to be the weighted average of that of SiO_2 and graphite, with concentrations of the latter being of 0, 15 and 30 % for each of the three runs. It should be noted however that this only provides a very rough estimation of the effects of Carbon incorporation in the structure, as the latter will likely be bound in Si-O-C complex whose optical behavior might differ significantly from the one we are assuming, besides the fact that we are neglecting any porosity in the material, which will reduce the refractive index. Indeed, the presence of carbon as contaminant is expected to introduce an imaginary component of the refractive index, leading to absorption losses within the material. A precise estimation of the impact of Carbon impurities would require to experimentally determine the refractive index of the deposited Si-O-C material, for instance by using ellipsometry, which could not be performed on features as small as the ones fabricated in the present work.

Regardless of our naïve assumption on the relation between refractive index and stoichiometry of the deposited nanomaterial, our results allow to draw some general conclusions on the performance of the fabricated nanostructures with respect to variations of their refractive index.

First of all, by comparing the graphs displayed in figure 3.6, it can be easily seen that pure silica structures exhibit the best performance, while the presence of carbon degrades their effectiveness. Taller structures in this case tend to extract less light, with the LEE reaching a plateau and then decreasing, a behavior we ascribe to absorption losses incurred during the propagation through the structure itself: as the imaginary part of the refractive index

increases, the maximum of the predicted LEE both lowers and progressively shifts to shorter structures.

This remarks that a control of the purity of the deposited material is of paramount importance for further photonic applications.

For the pure silica batch of simulations a plateau is not reached for the investigated geometries: we believe that similarly to what happens with semiconductor nanowires[36], the tapering angle of the structure plays a key role in determining the amount of light which is collected by the objective. As the cone behaves as an adiabatic taper, an increment in the radius of the base will indeed increase the amount of light funneled into the dielectric structure, but the fraction which is ultimately collected will drop if the height of the structure is not increased accordingly. These results agree qualitatively with the ones of our experimental investigation reported in figure 3.5, where a similar trend is displayed, and imply that the base radius and height of the structures cannot be treated as independent parameters for a maximization of the LEE.

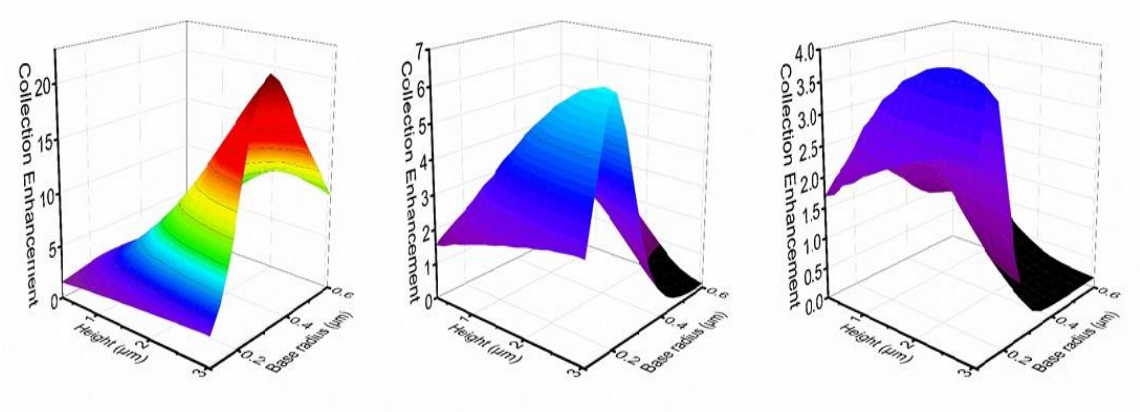


Figure 3.6 Simulated enhancement of PL collection efficiency for structures with different sizes and carbon content. From left to right, C incorporation of 0, 15 and 30 %

Conclusions

In this preliminary investigation, we have shown for the first time that the EBID technique can be a useful resource for the post-growth processing of epitaxial quantum dots, by significantly enhancing light extraction from the semiconductor matrix without causing any degradation in the quality of the dot and its emission features.

While the overall extraction efficiency hereby achieved by means of the fabricated nanostructures is definitely below the levels reached by the best performing semiconductor photonic cavities, the results are promising, especially in view of the possibility of using the deposited dielectric in subsequent processing steps as a hard mask for dry etching: this would allow for instance to fabricate tapered[35], or lens-topped, semiconductor nanowires with unprecedented precision.

More broadly, we believe that the 3D capabilities of the technique, coupled to its flexibility in terms of material choices, make it extremely attractive to the semiconductor quantum dot community, where extensive and complex nanofabrication is often performed on individual quantum emitters: for this purpose, the lack of damages induced in the processed QDs, as reported in our work, is of the utmost importance.

From the direct deposition of dielectric masks for dry etching and metal contacts for electrical nanodevices, to the fabrication of complex structures on top of the semiconductors to improve light extraction or engineer the projected far field, we expect EBID to play a significant role in the years to come in the field of quantum photonics with semiconductor QDs.

ASSOCIATED CONTENT

The following files are available free of charge.

Supporting information (PDF): Details and high resolution SEM images of each of the fabricated structures, and EDX analysis

AUTHOR INFORMATION

Corresponding Author

*Simone Varo, Tyndall National Institute, Dyke Parade, Cork, Republic of Ireland.

simone.varo@tyndall.ie

Author Contributions

The manuscript was written through contributions of all authors. All authors have given approval to the final version of the manuscript. ‡These authors contributed equally.

Funding Sources

This research was supported by Science Foundation Ireland under Grant Nos. 15/IA/2864, and 12/RC/2276_P2. ADF acknowledges support from EPSRC (EP/L017008/1) and ERC (Grant No. 819346).

Notes

Any additional relevant notes should be placed here.

ACKNOWLEDGMENT

The authors are grateful to Dr. K. Thomas for the MOVPE system support.

ABBREVIATIONS

MOVPE, Metal-Organic Vapor Phase Epitaxy; EBID, Electron beam Induced Deposition; QDs, Quantum Dots; LEE, Light Extraction Efficiency

REFERENCES

(1) Shields, A. J. Semiconductor Quantum Light Sources. *Nat. Photonics* **2007**, *1* (4), 215–223.

(2) Englund, D.; Majumdar, A.; Faraon, A.; Toishi, M.; Stoltz, N.; Petroff, P.; Vučkovi, J. Resonant Excitation of a Quantum Dot Strongly Coupled to a Photonic Crystal Nanocavity. *Phys Rev. Lett.* **2010**, 104, 073904.

(3) Benson, O.; Santori, C.; Pelton, M.; Yamamoto, Y. Regulated and Entangled Photons from a Single Quantum Dot. *Phys Rev. Lett.* **2000**, *84, 2513*.

(4) Chung, T. H.; Juska, G.; Moroni, S. T.; Pescaglini, A.; Gocalinska, A.; Pelucchi, E. Selective Carrier Injection into Patterned Arrays of Pyramidal Quantum Dots for Entangled Photon Light-Emitting Diodes. *Nat. Photonics* **2016**, *10* (12), 782–787.

(5) Zhang, J.; Wildmann, J. S.; Ding, F.; Trotta, R.; Huo, Y.; Zallo, E.; Huber, D.; Rastelli, A.; Schmidt, O. G. High Yield and Ultrafast Sources of Electrically Triggered Entangled-Photon Pairs Based on Strain-Tunable Quantum Dots. *Nat. Commun.* **2015**, *6*, 1–7.

(6) Zwiller, V.; Björk, G. Improved Light Extraction from Emitters in High Refractive Index Materials Using Solid Immersion Lenses. *J. Appl. Phys.* **2002**. 92, 660-665

(7) Höfer, B.; Zhang, J.; Wildmann, J.; Zallo, E.; Trotta, R.; Ding, F.; Rastelli, A.; Schmidt, O. G. Independent Tuning of Excitonic Emission Energy and Decay Time in Single Semiconductor Quantum Dots. *Appl. Phys. Lett.* **2017**, *110* (15), 151102.

(8) Norman, J. C.; Jung, D.; Wan, Y.; Bowers, J. E. Perspective: The Future of Quantum Dot Photonic Integrated Circuits. *APL Photonics* **2018**, *3* (3), 030901.

(9) Reitzenstein, S.; Forchel, A. Quantum Dot Micropillars. *J. Phys. D Appl. Phys.* **2010**, *43* (43), 33001–33025.

(10) Somaschi, N.; Giesz, V.; De Santis, L.; Loredo, J. C.; Almeida, M. P.; Hornecker, G.; Portalupi, S. L.; Grange, T.; Antón, C.; Demory, J.; Gómez, C.; Sagnes, I.; Lanzillotti-Kimura, N. D.; Lemaítre, A.; Auffeves, A.; White, A. G.; Lanco, L.; Senellart, P. Near-Optimal Single-Photon Sources in the Solid State. *Nat. Photonics* **2016**, *10* (5), 340–345.

(11) Michler, P.; Kiraz, A.; Becher, C.; Schoenfeld, W. V.; Petroff, P. M.; Zhang, L.; Hu, E.; Imamoğlu, A. A Quantum Dot Single-Photon Turnstile Device. *Science.* **2000**, *290* (5500), 2282–2285.

(12) Reimer, M. E.; Bulgarini, G.; Akopian, N.; Hocevar, M.; Bavinck, M. B.; Verheijen, M. A.; Bakkers, E. P. A. M.; Kouwenhoven, L. P.; Zwiller, V. Bright Single-Photon Sources

in Bottom-up Tailored Nanowires. *Nat. Commun.* **2012**, *3* (1), 737.

(13) Kolatschek, S.; Hepp, S.; Sartison, M.; Jetter, M.; Michler, P.; Portalupi, S. L. Deterministic Fabrication of Circular Bragg Gratings Coupled to Single Quantum Emitters via the Combination of *in-Situ* Optical Lithography and Electron-Beam Lithography. *J. Appl. Phys.* **2019**, *125* (4), 045701.

(14) Munsch, M.; Malik, N. S.; Dupuy, E.; Delga, A.; Bleuse, J.; Gérard, J.-M.; Claudon, J.; Gregersen, N.; Mørk, J. Dielectric GaAs Antenna Ensuring an Efficient Broadband Coupling between an InAs Quantum Dot and a Gaussian Optical Beam. *Phys. Rev. Lett.* **2013**, *110* (17), 177402.

(15) Gschrey, M.; Thoma, A.; Schnauber, P.; Seifried, M.; Schmidt, R.; Wohlfeil, B.; Krüger, L.; Schulze, J. H.; Heindel, T.; Burger, S.; Schmidt, F.; Strittmatter, A.; Rodt, S.; Reitzenstein, S. Highly Indistinguishable Photons from Deterministic Quantum-Dot Microlenses Utilizing Three-Dimensional in Situ Electron-Beam Lithography. *Nat. Commun.* **2015**, *6*.

(16) Ma, Y.; Kremer, P. E.; Gerardot, B. D. Efficient Photon Extraction from a Quantum Dot in a Broad-Band Planar Cavity Antenna. *J. Appl. Phys.* **2014**, *115* (2), 023106.

(17) Sartison, M.; Portalupi, S. L.; Gissibl, T.; Jetter, M.; Giessen, H.; Michler, P. Combining In-Situ Lithography with 3D Printed Solid Immersion Lenses for Single Quantum Dot Spectroscopy. *Sci. Rep.* **2017**, *7* (1), 39916.

(18) Sapienza, L.; Davanço, M.; Badolato, A.; Srinivasan, K. Nanoscale Optical Positioning of Single Quantum Dots for Bright and Pure Single-Photon Emission. *Nat. Commun.* **2015**, *6* (1), 7833.

(19) Huth, M.; Porrati, F.; Schwalb, C.; Winhold, M.; Sachser, R.; Dukic, M.; Adams, J.; Fantner, G. Focused Electron Beam Induced Deposition: A Perspective. *Beilstein J. Nanotechnol.* **2012**, *3* (1), 597–619.

(20) van Dorp, W. F.; Hagen, C. W. A Critical Literature Review of Focused Electron Beam Induced Deposition. *J. Appl. Phys.* **2008**, *104* (8), 081301.

(21) De Angelis, F.; Liberale, C.; Coluccio, M. L.; Cojoc, G.; Di Fabrizio, E. Emerging Fabrication Techniques for 3D Nano-Structuring in Plasmonics and Single Molecule Studies. *Nanoscale* **2011**, *3* (7), 2689-2696.

(22) Fowlkes, J. D.; Winkler, R.; Lewis, B. B.; Fernández-Pacheco, A.; Skoric, L.; Sanz-Hernández, D.; Stanford, M. G.; Mutunga, E.; Rack, P. D.; Plank, H. High-Fidelity 3D-Nanoprinting via Focused Electron Beams: Computer-Aided Design (3BID). *ACS Appl. Nano Mater.* **2018**, *1* (3), 1028–1041.

(23) Jesse, S.; Borisevich, A. Y.; Fowlkes, J. D.; Lupini, A. R.; Rack, P. D.; Unocic, R. R.; Sumpter, B. G.; Kalinin, S. V.; Belianinov, A.; Ovchinnikova, O. S. Directing Matter: Toward Atomic-Scale 3D Nanofabrication. *ACS Nano*., **2016**, pp 5600–5618.

(24) Frabboni, S.; Gazzadi, G. C.; Felisari, L.; Spessot, A. Fabrication by Electron Beam Induced Deposition and Transmission Electron Microscopic Characterization of Sub-10-Nm Freestanding Pt Nanowires. *Appl. Phys. Lett.* **2006**, *88* (21), 213116.

(25) Shawrav, M. M.; Taus, P.; Wanzenboeck, H. D.; Schinnerl, M.; Stöger-Pollach, M.; Schwarz, S.; Steiger-Thirsfeld, A.; Bertagnolli, E. Highly Conductive and Pure Gold Nanostructures Grown by Electron Beam Induced Deposition. *Sci. Rep.* **2016**, *6* (1), 34003.

(26) Winkler, R.; Schmidt, F. P.; Haselmann, U.; Fowlkes, J. D.; Lewis, B. B.; Kothleitner, G.; Rack, P. D.; Plank, H. Direct-Write 3D Nanoprinting of Plasmonic Structures. *ACS Appl. Mater. Interfaces* **2017**, *9* (9), 8233–8240.

(27) Pfeiffer, M.; Lindfors, K.; Wolpert, C.; Atkinson, P.; Benyoucef, M.; Rastelli, A.; Schmidt, O. G.; Giessen, H.; Lippitz, M. Enhancing the Optical Excitation Efficiency of a Single Self-Assembled Quantum Dot with a Plasmonic Nanoantenna. *Nano Lett.* **2010**, *10* (11), 4555–4558.

(28) Li, X.; Su, R.-L.; Zhou, Z.-K.; Yu, Y.; Di Falco, A. Photonic Trimming of Quantum Emitters via Direct Fabrication of Metallic Nanofeatures. *APL Photonics* **2018**, *3* (7), 071301.

(29) Juska, G.; Dimastrodonato, V.; Mereni, L. O.; Gocalinska, A.; Pelucchi, E. Towards Quantum-Dot Arrays of Entangled Photon Emitters. *Nat. Photonics* **2013**, *7* (7), 527–531.

(30) Dimastrodonato, V.; Pelucchi, E.; Vvedensky, D. D. Self-Limiting Evolution of Seeded Quantum Wires and Dots on Patterned Substrates. *Phys. Rev. Lett.* **2012**, *108* (25), 256102.

(31) Pelucchi, E.; Moroni, S. T.; Dimastrodonato, V.; Vvedensky, D. D. Self-Ordered Nanostructures on Patterned Substrates. *J. Mater. Sci. Mater. Electron.* **2018**, *29* (2), 952–967.

(32) Varo, S.; Juska, G.; Ranjbar, I.; Moroni, S.; Gocalinska, A.; Pelucchi, E. Engineering Site-Controlled Quantum Dots for Optical Quantum Information Processing. In *Low-Dimensional Materials and Devices 2019*; Kobayashi, N. P., Talin, A. A., Davydov, A. V., Eds.; SPIE, 2019; Vol. 11085, p 6.

(33) de Boer, S. K.; van Dorp, W. F.; De Hosson, J. T. M. Charging Effects during Focused Electron Beam Induced Deposition of Silicon Oxide. *J. Vac. Sci. Technol. B,*

Nanotechnol. Microelectron. Mater. Process. Meas. Phenom. **2011**, *29* (6), 06FD01.

(34) Juska, G.; Murray, E.; Dimastrodonato, V.; Chung, T. H.; Moroni, S.; Gocalinska, A.; Pelucchi, E. Conditions for Entangled Photon Emission from (111)B Site-Controlled Pyramidal Quantum Dots. *J. Appl. Phys* **2015,** 117, 134302

(35) Claudon, J.; Bleuse, J.; Malik, N. S.; Bazin, M.; Jaffrennou, P.; Gregersen, N.; Sauvan, C.; Lalanne, P.; Gérard, J.-M. A Highly Efficient Single-Photon Source Based on a Quantum Dot in a Photonic Nanowire. *Nat. Photonics* **2010**, *4* (3), 174–177.

(36) Gregersen, N.; Nielsen, T. R.; Claudon, J.; Gérard, J.-M.; Mørk, J. Controlling the Emission Profile of a Nanowire with a Conical Taper. *Opt. Lett.* **2008**, *33* (15), 1693-1695.

4. Design and fabrication of micro/nanopillars to increase light extraction efficiency

4.1 Introduction: photonic nanowires

While the deposition of nanostructures via EBID proved to yield significant improvements to the light extraction efficiency from the semiconductor matrix, it was well below the level achieved by other groups using microcavities. Several examples of high-performing ones are reported in the literature, either in the form of micropillars[1,2] or as 2D photonic crystals[3–7]: the underlying principle is that when a quantum emitter radiates its power, the configuration of the surrounding environment dictates in which directions emission can take place. Micropillars can be easily fabricated via dry etching, and if the quantum dot is grown between two distributed Bragg reflectors forming a cavity, in the so-called weak coupling regime, the Purcell effect will result in a redirection of the dipole emission, as the latter will be coupled to the only electromagnetic modes available, that is, the ones determined by the cavity itself. A similar concept is at the root of 2D photonic crystal cavities with embedded quantum dots.

For Pyramidal quantum dots however, none of these approaches appear feasible: micropillar cavities require DBRs, whose planarity is not compatible with 3 dimensional growth profile that characterizes MOVPE fabrication of PQDs, and while attempts have been made in the past to achieve integration of PQDs in 2D photonic crystals[8,9], this was achieved by growing dots on tetrahedral nano-, and not micro-, holes. As the size of the system in that case is of the same order of magnitude of the adatom diffusion length, the whole

growth process yields different results, and while the resulting QDs are far more suitable for integration in photonic structures defined via electron beam lithography, they never reached a quality comparable to the one demonstrated by their larger counterparts, nor the ability to generate entangled photons.

A different approach to significantly increase extraction efficiency which has gained considerable interest is represented by photonic nanowires[10–16], also called nanopillars: in their simplest form, these are semiconductor cylinders of uniform size, containing a quantum emitter along their axes. Similarly to what happens for micropillars, if their lateral size is properly chosen, these structures have the ability to channel the emission of the quantum source along the axis of the nanowire, suppressing emission in plane. However, the abrupt termination of the cylinder causes both significant backreflection of the mode and a significant divergence of the light which is emitted by the nanowaveguide: both effects are obviously detrimental for light extraction and collection, but can be significantly reduced by the termination of the cylinder with an adiabatic taper[17,18]. The gradually diminishing effective refractive index experienced by the mode during propagation along the taper allows it to leak out more and more from the semiconductor waveguide, resulting in a smooth transition into free space upon finally reaching the tip, as illustrated in figure 4.1.

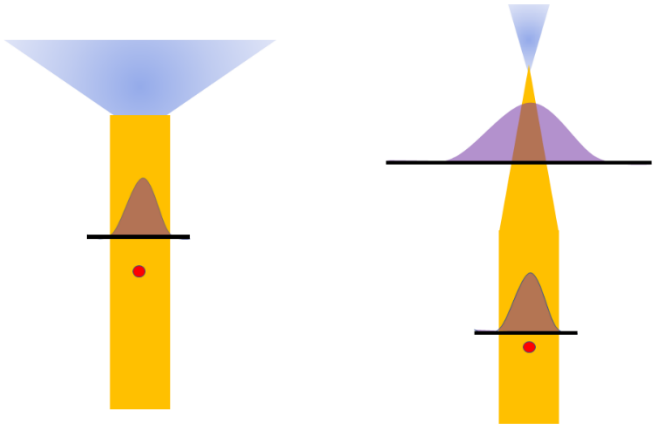


Figure 4.1 Comparison of a cylindrically shaped photonic nanowire without a tapered section (left) and with an adiabatic taper to improve light extraction

Photonic nanowires have been fabricated both via top-down[19] and bottom-up[20] approaches: the latter is usually a preferable route due to the lack of surface damage induced during the etching. However, the bottom-up approach is usually based on a gold catalyzed vapor liquid solid epitaxy which is, once more, not compatible with the growth mechanism of PQDs: a top-down approach is instead possible.

4.2 A self-aligning process for fabricating photonic nanowires with pyramidal quantum dots

Usually, top-down fabrication of photonic nanowires involves a lengthy process: since quantum emitters are randomly distributed, locating them using micro-PL is required as a starting point. A hard mask is then patterned directly above the QD, and an optimized dry etching process is used to fabricate the nanowire. PQDs have the advantage that the position of the emitter is known, as they form a well-defined lattice, but the topography of an as grown PQDs sample also offers some additional engineering opportunities that allow to skip an additional lithographic step altogether.

After the growth of a typical sample, the filling of the pyramid is far from complete, and a vestigial recess remains: as the MOVPE growth is symmetrical

on the three 111A planes, the symmetry of the recess reflects the one of the original inverted tetrahedral template, which also implies that alignment is preserved with respect to the quantum dot. If a dielectric layer is conformally deposited on the sample via sputtering or plasma-enhanced chemical vapor deposition (PECVD), its topography will once more reflect the 3-dimensional template. Exposure of the GaAs via CMP will then result in an inverted tetrahedrally-shaped dielectric mask which will be aligned to the quantum dot, and that can be used to define a triangular section pillar via a selective and anisotropic dry etching (fig. 4.2).

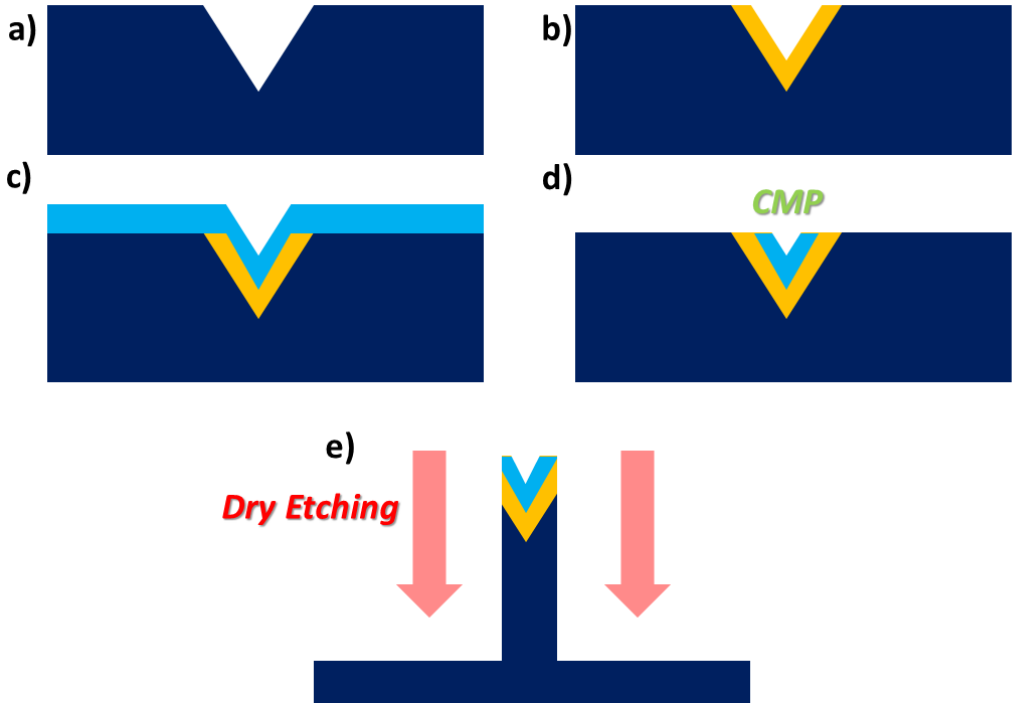


Figure 4.2 Micro/nanopillar fabrication process. a) substrate patterning. b) epitaxial growth. c) dielectric deposition. d) planarization e) dry etching

This is an inherently self-aligning technique: the position of the dot is defined by the symmetry of the growth template, and the alignment of the mask is guaranteed by the conformality of the deposition that mimics it.

However, the shape of the mask and the position of the epi-layer with respect to it create a significant problem: as discussed previously, the typical nanowire structure comprises a straight section which houses the quantum emitter and defines the operating wavelength of the photonic structure, and a tapered section that allows to maximize light extraction efficiency: as the dot is located less than 2 microns below the tip of the mask, there is no room to fabricate the nanowire directly in a pointing up configuration. The only possibility is to make an inverted structure with the taper pointing downward, and then finding a way to invert it.

4.3 FDTD Simulations of photonic nanowires with triangular sections

A pillar fabricated using the proposed approach would have, as discussed in the previous paragraph, a triangular cross-section: it is obvious that its behavior might deviate significantly from nanopillars which instead have a cylindrical one, due to the different rotational symmetry of the waveguide. A set of simulations was thus performed to assess the impact of geometric parameters on the confined mode, and whether a mechanism enforcing directional emission can appear in this case as well.

All of the results that will follow have been obtained by simulating the structures using Lumerical FDTD.

The first set of simulations carried out was a sweep of the lateral size of a triangularly-shaped waveguide with a length of 3 microns, using perfectly matched layers (PMLs) on either side of the waveguide in order to mimic an infinite one. The QD was approximated as a dipole positioned at the centroid of the triangular section and initially aligned along the axis of the triangle, and the power coming out of either end of the waveguide and into the PML was recorded.

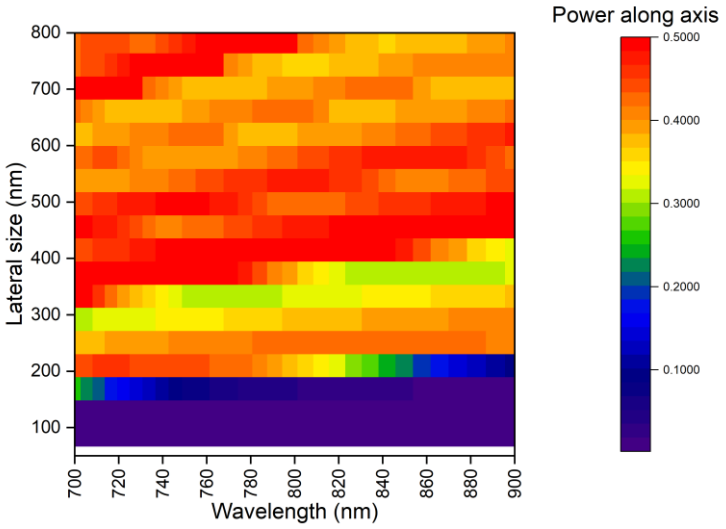


Figure 4.3 Fraction of dipole power emitted along the longitudinal axis of the waveguide, as a function of wavelength and lateral size

Results reported in fig. 4.3 clearly indicate that a significant amount of light can be channeled along the axis of the waveguide, provided a proper size is chosen: the lower high channeling band corresponds to the first mode supported by the structure, whereas the second band corresponds to the second order mode. It is interesting to observe that the waveguide operates quite well over a broad range of wavelengths, as seen in figure 4.3 for a lateral size of 250 nm: this is observed also in cylindrical ones, and makes photonic nanowires excellent structures for the extraction of entangled photons, since the two paired photon usually have fairly close emission wavelengths.

Caution is however needed in the interpretation of these results, as the imaginary component of the refractive index was neglected: this is quite correct for simulating photons emitted above the absorption threshold of GaAs at 10 K (820 nm), but obviously implies that our simulations fails to take into account losses at shorter wavelengths, where attenuation would become important: this suggest that application of this kind of structure for improving light extraction is viable for the usual InGaAs dots that operate at around 860 nm, but would be of limited usefulness for the GaAs ones.

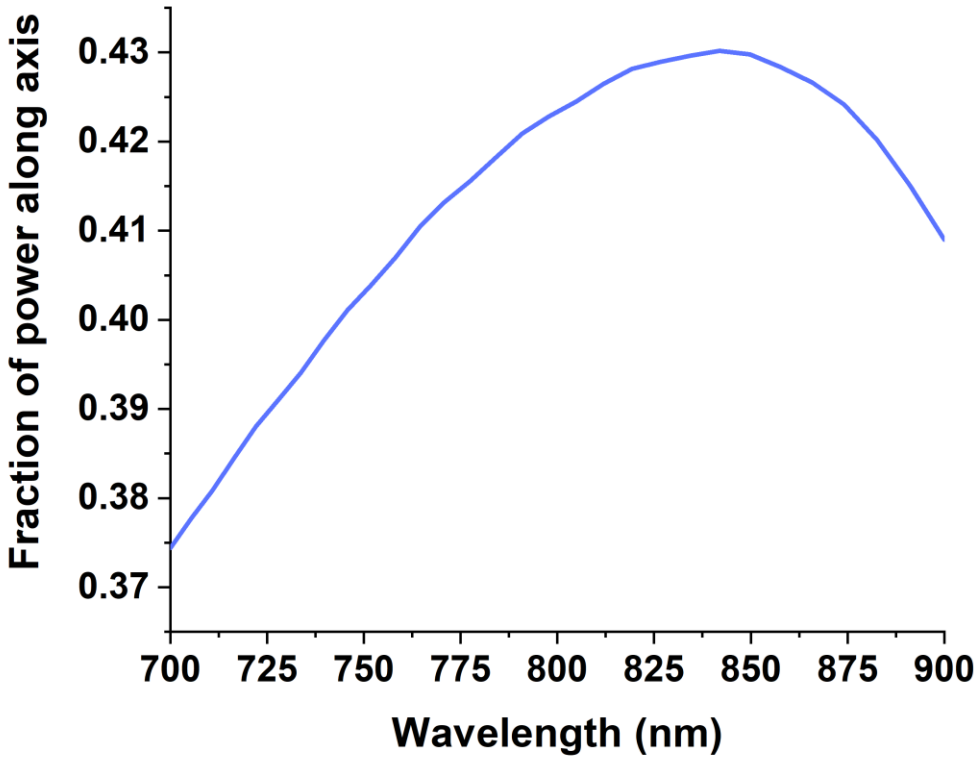


Figure 4.4 Fraction of dipole power emitted along the axis as a function of the wavelength, for a triangular wavelength of 250 nm lateral size

Moreover, in the case of polarization entangled photons, a different extraction efficiency for each of the photons composing the pair would affect the quality of the entanglement: since the waveguide in our case does not have complete rotational symmetry, it is important to assess the impact of the orientation of the dipole on the operation of the nanostructure.

To do that, a series of simulations was carried out, rotating the direction of the dipole of 90 degrees in steps of 10 degrees: results indicate that despite its asymmetry (or better, C_{3v} only symmetry), the nanowaguide is quite consistent in its behavior with respect to different polarizations, and its emission channeling effect remains surprisingly almost constant regardless of the direction of the emitting dipole (figure 4.5), although the two modes are obviously quite different, as can be seen in figure 4.6.

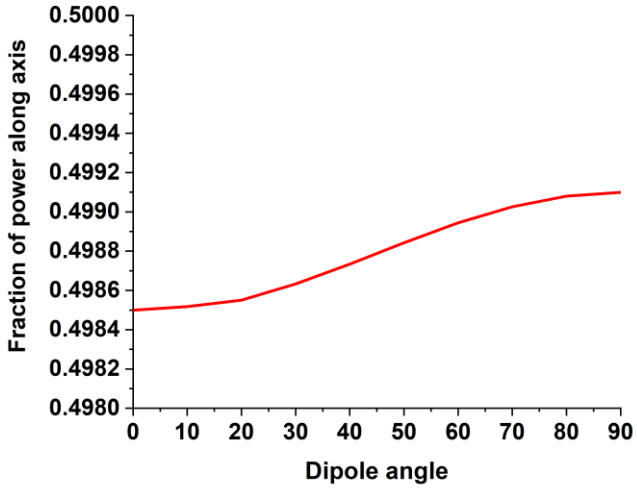


Figure 4.5 Fraction of power emitted along the axis as a function of the dipole angle, for a wavelength of 865 nm and a lateral size of 500 nm

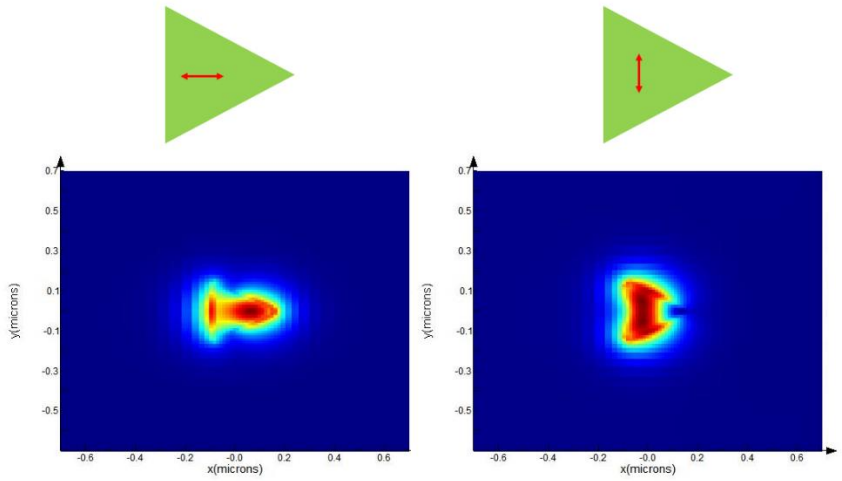


Figure 4.6 Normalized amplitude of the two fields emitted by a dipole. Left: for a dipole axis aligned along the axis of the triangular section, right: for a dipole direction aligned perpendicular to it (parallel to one of the sides).

Finally, we assess the importance of the tapering angle by simulating the whole nanopillar structure with a 3 microns long tapered section, terminating in a flat triangular surface of 60 nm lateral size, while the lateral size of the straight section containing the dipole was chosen to be 250 nm, in order to ensure single mode operation at the typical emission wavelengths of our InGaAs dots (850-870 nm). Two monitors were used to record the power flux:

one at the interface between the straight and tapered section of the nanopillar and one 500 nm above the end of the taper. Key results are reported in figure 4.7 (left), where it can be easily seen that the taper is quite effective at providing a significant power extraction, which reaches 40% at the wavelengths of interest, and could be increased further by adding a mirror on the bottom surface of the nanopillar. For comparison, a simulation of the same structure without the tapered section yields a mere 9% extraction efficiency.

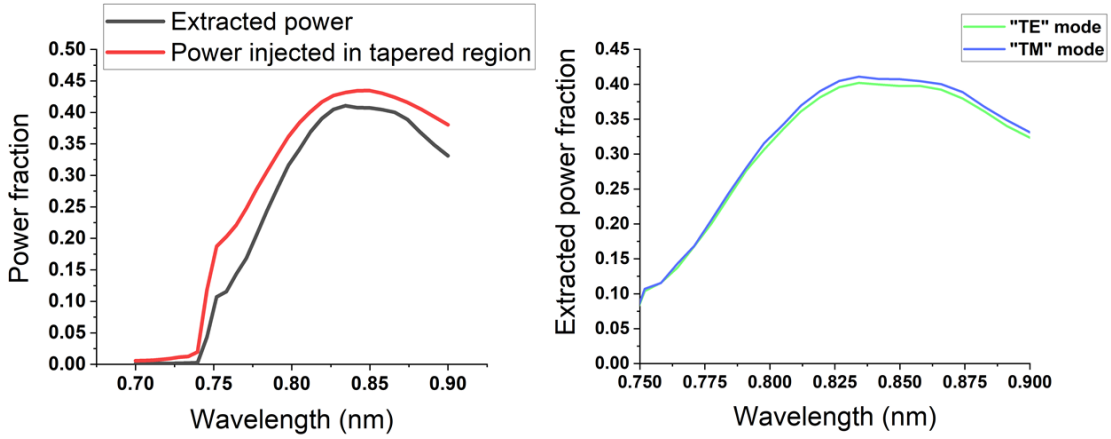


Figure 4.7 Left: fraction of dipole power injected in the tapered region (red curve) and fraction of power extracted from the taper (black curve). Right: extracted power from taper for the two orthogonal dipole orientation

Unsurprisingly, the behavior of the tapered photonic nanowire is again consistent for different polarization states: this stems from the insensitivity to polarization exhibited by the straight section previously discussed, with the taper actually reducing the effective refractive index during propagation of the modes along it, and thus making it even more polarization-insensitive (figure 4.7, right).

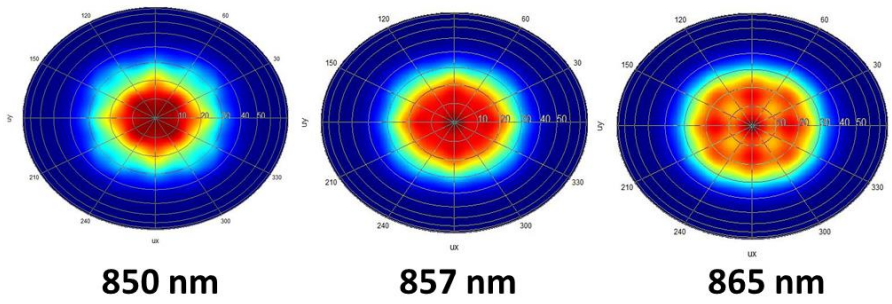


Figure 4.8 Calculated far fields from monitors placed 500 nm above the tip of a tapered nanopillar, for different wavelengths

On the other hand, simulation of the far fields yield more complex results, and seem to suggest a rather significant dependence of the latter on the emission wavelength, as reported in figure 4.8. While this has little impact on the ability to collect light using objectives as the emission is still quite directional, a far field which is more complex than a Gaussian/monopolar one might create problems for the coupling to single mode waveguides, where the amount of coupled power is dictated by mode-matching conditions, and might require more stringent fabrication tolerances than when brightness is assumed as the only figure of merit.

4.4 Dry etching: fundamentals

Wet etching has a large number of advantages, such as a high selectivity, but when coupled with the unconventional geometry of our samples it severely limits the kind of post growth processing that can be performed on them. Most notably, it is very difficult to fabricate vertical structures with high aspect ratios such as micropillars, or to transfer complex patterns in the semiconductor material.

We have already pointed out how polishing of the as-grown PQDs samples restores a planar geometry, which is the starting point for most semiconductor processing techniques, but a broadening of the available etching techniques is required in order to start developing new structures. In the case of nanopillar fabrication, employing wet etching is hardly an option, and a dry etching process has to be developed.

Dry etching is the second family of material removal techniques used in semiconductor technology, which uses a plasma ion bombardment to etch the material: while several techniques fall under this umbrella name, we will focus on the most common, which is Inductively Coupled Plasma Reactive Ion Etching (ICP-RIE) and use the two terms interchangeably.

In a typical RIE system, a radiofrequency signal (often 13.56 MHz), is used to generate and sustain a plasma between two parallel plates in a vacuum chamber where pressure and gas composition are precisely controlled: acceleration of the initial free electrons and ions quickly creates an avalanche effect, as collisions create even more electrons and ions until an equilibrium state is reached between the generation and recombination of free charges. Moreover, formation of unstable ions promotes their dissociation into new highly reactive species, which can either be again ionic in nature, or neutral radicals (molecules with an unpaired electron), as shown in figure 4.9.

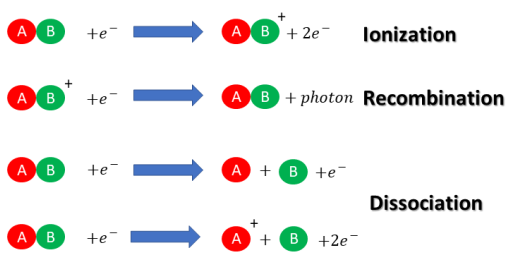


Figure 4.9 Typical processes happening in a plasma discharge

The different mobilities of the species in the chamber tend to create a non-uniform charge distribution: electrons, having a smaller mass than ions, respond very quickly to the RF field, and introduction of a capacitor in series to the cathode electrode allows for the buildup of a small negative charge and the formation of an electric field across the so-called ion sheath (fig. 4.10).

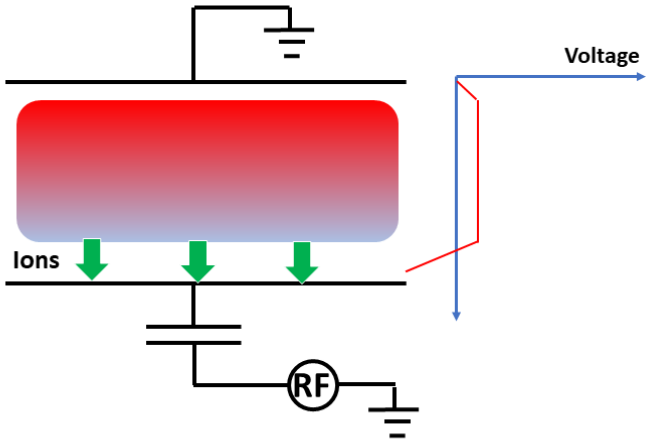


Figure 4.10: Sketch of a typical RIE chamber

Ions that diffuse from the plasma glow to this region are accelerated by the electric field toward the cathode, and the sample is placed upon it.

Two different mechanisms concur to the removal of material from the sample: a physical and a chemical one. They are usually both present at the same time, although their relative magnitude is dependent on the various parameters such as pressure, chemical composition of the plasma and magnitude of the electric field across the sheath.

The physical component of the etching is nothing else than the dislodging of atoms from the surface due to momentum transfer from the impacting high-

energy ions: a prime example of this is the use of Argon chemistries, where Ar^+ ions bombard the exposed semiconductor. This mechanism usually implies a low selectivity, as there is little to no discrimination due to the composition of the sample of the layers being etched.

The chemical component of the etching is related to the interaction of ions and neutral radicals coming from the plasma with the atoms on the exposed surface: it is a far more complex mechanism that entails the formation of volatile compounds (e.g. chlorides of III-V metals), which subsequently diffuse away from the sample.

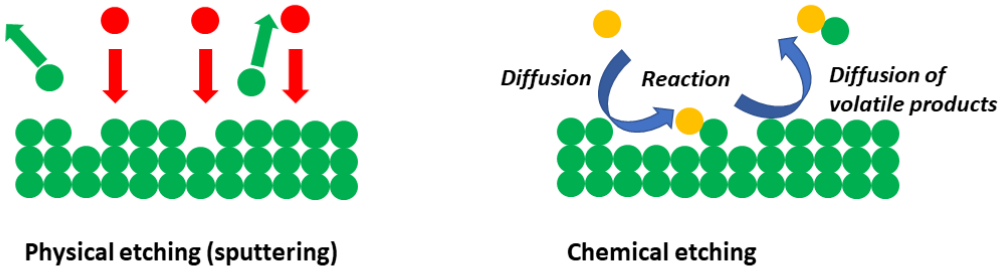


Figure 4.11 The two process happening simultaneously during dry etching. Left: ballistic dislodging of atoms from the surface. Right: chemical etching by reactive species via the formation of volatile compounds

A more advanced approach than RIE is ICP-RIE, which allows for an independent control of plasma density and ion energy by using a series of independent RF coils for ionization and sustaining of the plasma (figure 4.12): the plasma itself acts as the secondary of an electric transformer, and strong currents are created within it by the induced electric field. This allows to achieve larger plasma densities, and to relax constraints on the table power: as the latter is no longer the one responsible for sustaining the plasma, smaller powers can be applied, which in turn imply a smaller electric field across the ion sheath, and a bombardment of the sample with ions of lower energy.

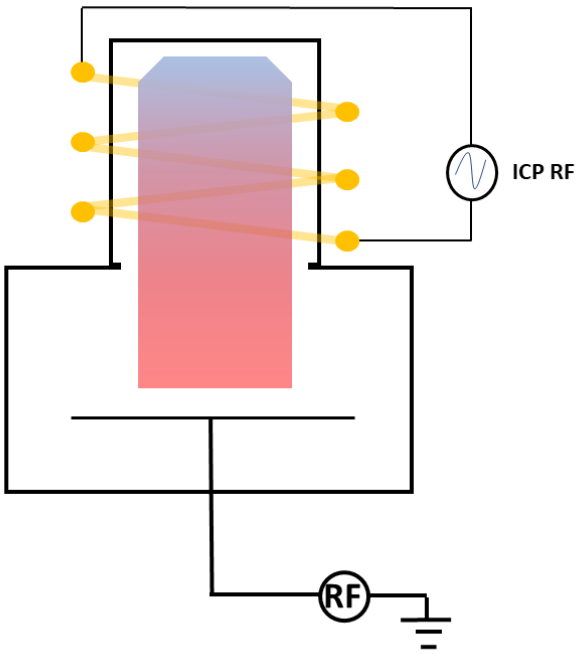


Figure 4.12 Sketch of an ICP chamber

The hallmark characteristic of dry etching is undoubtedly the high degree of anisotropy that can be achieved, while maintaining a low selectivity with respect to different crystal planes. The choice of the etching chemistry (that is, the gases introduced within the etch chamber) is obviously dependent on the material that is to be etched: in the case of our samples, where the bulk of the material is usually GaAs, this implies the use of Chlorine based chemistries that use either BCl_3 , Cl_2 or both. High selectivities can be achieved with respect to the mask material by using both hard masks (SiO_2) or photopolymers in the latter role.

4.5 Fabrication of photonic micro/nanopillars: challenges and key results

Top-down fabrication of nanopillars requires an optimized dry etching recipe that guarantees smooth sidewalls, a precise control of their angle, and a minimization of the surface damage that, due to the closeness of the quantum

dots to the pillar's sidewalls, might degrade the quality of the latter's emission due to the creation of a noisier environment.

$SiCl_4$ is usually the gas of choice for this kind of fabrication, but it wasn't available on our tool, so an alternative process had to be designed: the recipe I developed was inspired by the result of Volatier et al.[21], who managed to achieve a good control of the sidewall angle using their $BCl_3/Cl_2/Ar/N_2$ recipe by changing the amount of nitrogen in the plasma. The mechanism proposed in their paper to explain the behavior of this specific chemistry for the etching of GaAs is that N_2 has a surface passivating effect stemming from its interaction with volatile products coming from the etching of the SiO_2 mask, and thus can be used to tune both the etch rate and the sidewall angle. Several tests have been performed to assess the impact of etching parameters on the shape of vertical structures etched on 111B oriented GaAs crystal planes: in general control of the geometry was achieved by only changing the amount of N_2 and platen power (and so, DC bias), while leaving the other parameters constant: a higher platen power was found to be required during etch steps with high N_2 content not only because it allows for a greater verticality due to the higher DC bias across the ion sheath, but also prevents excessive deposition of polymer on the sidewalls of the etched nanopillars.

The final recipe used for the fabrication of nanopillars is comprised of 2 steps, as reported in table 4.1: a first step carried out a higher power/DC bias and N_2 content to obtain the straight section of the waveguide, and second step carried out at lower power and N_2 content to create a suitable taper. An SEM image of a typical outcome is reported in figure 4.13.

Table 4.1 Process parameters used in the fabrication of tapered nanowires

	Gas fluxes (BCl3/Cl2/Ar/N2) (sccm)	**Platen (RF) Power (W)**	**ICP power (W)**	**Pressure mTorr**
Step 1	13/13/13/6	60	600	5
Step 2	13/13/13/5	45	600	5

Choice of the etch times for either step is of paramount importance: for the first one, because it is desirable to have the dot lying inside the straight section in order to have the proper photonic mode it could couple to and, more critically, the second etch step should be terminated so that the pillars are standing on a tip which is not too large to cause reflections of the mode at the interface, but not too small so that the pillar falls (see figure 4.13).

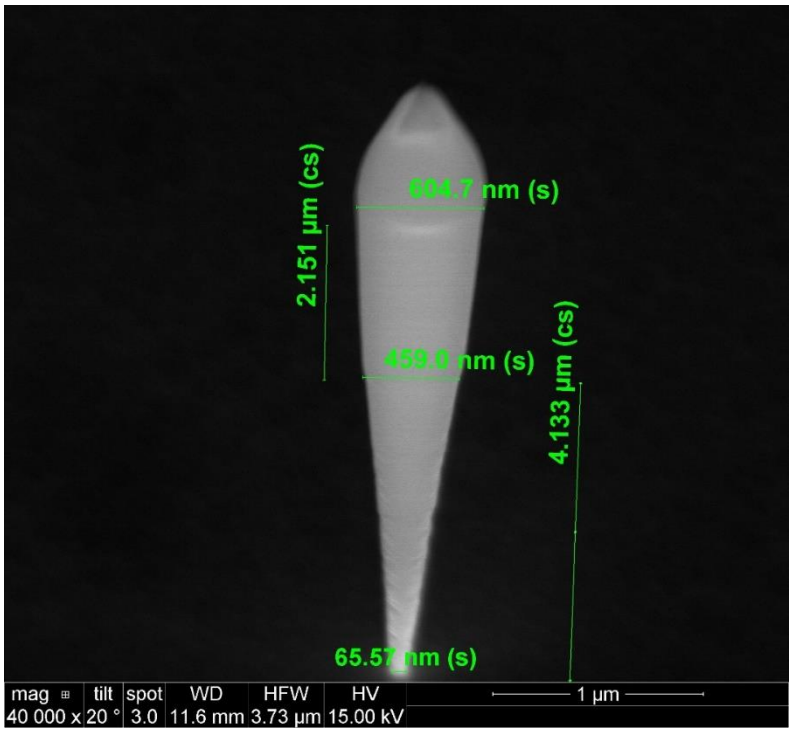


Figure 4.13 example of a successfully etched nanopillar with an inverted taper

In general, terminating the etching at the right moment is difficult, and since the polishing step usually introduces a gradient in the size of the masks across the sample, the loss of some nanopillars should be expected, with the smaller ones usually falling down once the base of the tapered section becomes too small to support their own weight.

Nanopillars fabricated in this way (or simply with vertical sidewalls) can be tested in a micro-PL setup, and indeed performed comparably to, or better than, back-etched pyramids in terms of light extraction efficiency, while displaying a greater uniformity than the latter in terms of spectral quality. The problem is that extracting light from the top is still difficult, as the lack of a taper causes, as discussed previously, significant reflections and a divergence of the mode. The problem is further exacerbated by the presence of the residual recess and of the mask on the side the light is extracted from, which causes both reflections and scattering, significantly depressing light extraction and collection efficiencies.

Nevertheless, quite promising results were obtained by using rather large pillars, of sizes between 1 and 2 μm in conjunction with a superhemispherical (Weierstraß) solid immersion lens to counteract these problems: in this case the pillars were simply straight, so there was little concern about their ability to withstand the weight of the lens without breaking. Indeed, the result represented our record of brightness with InGaAs quantum dots, achieving a photon count that was more than 10 times higher than the one achieved by processing the sample using the usual back-etching route.

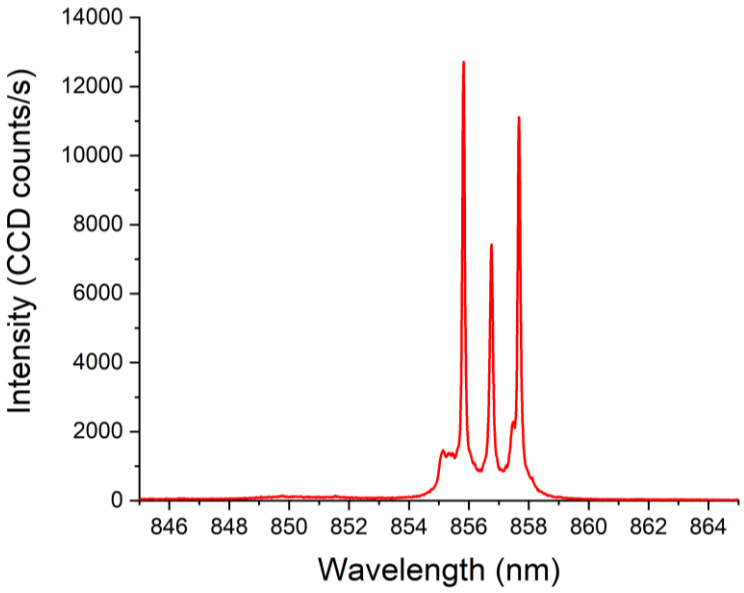


Figure 4.14 micro-PL spectrum of a particularly bright micropillar with a solid immersion lens on top

However, the brightness enhancement in this case is merely due to the classic waveguiding behavior of the pillar, with little to no channeling of the dot's emission in a specific mode, and the need to use a solid immersion lens further remarks that there is a strong scattering of the light at the interface, making this approach quite difficult for coupling with photonic circuits or a single mode optical fibre, which would be one of the most important advantages of nanopillars in the first place.

Finally, it was observed that for micropillars light tends to be quite strongly polarized when extracted from the recess: this was confirmed by FDTD simulations and we attribute it to the different boundary conditions at the interface (i.e. the tetrahedral recess) experienced by dipolar emissions of different polarizations , which affect the amount of light that is emitted from the pillar: this would in turn make pillars in the micron range of sizes unsuitable for extraction of polarization entangled photons.

4.6 Development of an inversion technique: preliminary results

By far the largest issue affecting the inversion of nanopillars is their inverted taper geometry that stems from the etching: as discussed before, there is no way to produce structures directly in a “pointing up” configuration, so that a way has to be devised to turn them upside down prior to micro-PL characterization. However, since after the etching they are attached only by the very small tapered tip that can barely support their own weight, they have little to no capability to withstand aggressive processing steps: this is in stark contrast with other nanopillar families, which are attached to the substrate by the larger base, and can survive encapsulation in an elastomeric layer (e.g. PDMS) which is then peeled off [20].

Since this is not possible, a more complex process has been devised: first of all, a rather thick (500 nm) Si_3N_4 is deposited conformally on the nanopillars, encapsulating them in a hard dielectric layer that can provide structural support. Then, dry etching is used once more to anisotropically etch the structures and expose the top of the nanopillars by exploiting a highly selective O_2/SF_6 chemistry that doesn’t etch GaAs.

The sample is subsequently adhesive-bonded on a carrier substrate, and then either the pillars are broken off directly at the tip by applying a shear force to the sample, or a several minutes etch is performed in Buffered Oxide Etchant (BOE) to remove the Silicon Nitride, leaving them with the larger base firmly bonded on the carrier and the fragile tip attached to the original GaAs wafer piece so that it can be easily broken.

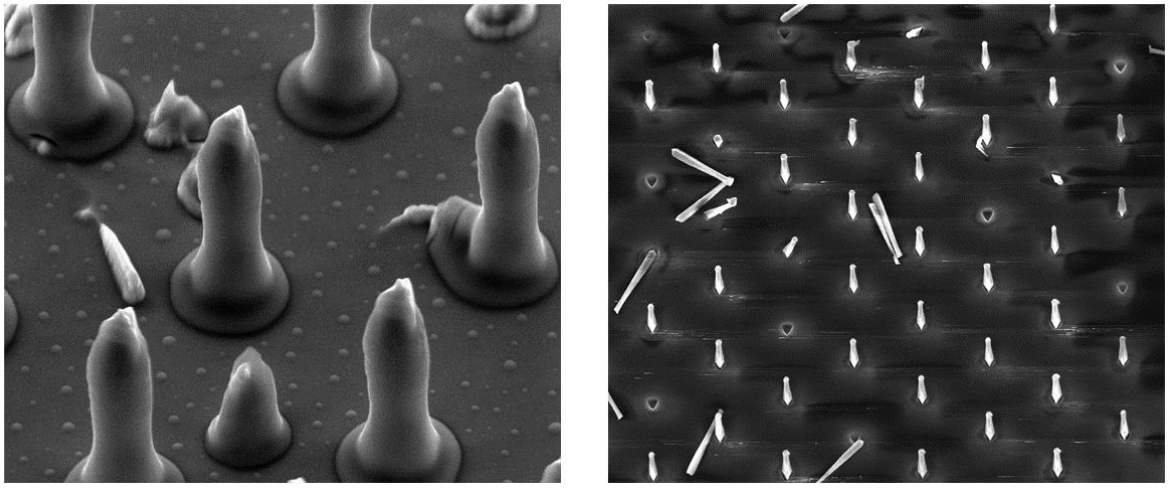


Figure 4.15 left: pillars encapsulated in a Silicon Nitride shell after dry etching end exposure of the top. Right: after bonding on an adhesive and inversion

This technique is quite complex and has so far been tested only on samples without quantum dots. It is also still undergoing optimization at the moment, but we have hope it will eventually lead to a reliable and reproducible inversion procedure.

1. Somaschi, N. *et al.* Near-optimal single-photon sources in the solid state. *Nat. Photonics* **10**, 340–345 (2016).

2. Nowak, A. K. *et al.* Deterministic and electrically tunable bright single-photon source. *Nat. Commun.* **5**, 3240 (2014).

3. Englund, D. *et al.* Resonant Excitation of a Quantum Dot Strongly Coupled to a Photonic Crystal Nanocavity. *Phys. Rev. Lett.* **104**, 073904 (2010).

4. Faraon, A. *et al.* Local quantum dot tuning on photonic crystal chips.

Appl. Phys. Lett. **90**, 213110 (2007).

5. Faraon, A. *et al.* Integrated quantum optical networks based on quantum dots and photonic crystals. *New J. Phys.* **13**, 055025 (2011).

6. Lodahl, P. All-solid-state quantum optics employing quantum dots in photonic crystals. *Quantum Opt. with Semicond. Nanostructures* 395-422e (2012) doi:10.1533/9780857096395.4.393.

7. Madsen, K. H. *et al.* Efficient out-coupling of high-purity single photons from a coherent quantum dot in a photonic-crystal cavity. *Phys. Rev. B* **90**, 155303 (2014).

8. Gallo, P. *et al.* Integration of site-controlled pyramidal quantum dots and photonic crystal membrane cavities. *Appl. Phys. Lett.* **92**, 263101 (2008).

9. Pelucchi, E., Watanabe, S., Leifer, K., Dwir, B. & Kapon, E. Site-controlled quantum dots grown in inverted pyramids for photonic crystal applications. *Phys. E Low-dimensional Syst. Nanostructures* **23**, 476–481 (2004).

10. Jöns, K. D. *et al.* Bright nanoscale source of deterministic entangled photon pairs violating Bell's inequality. *Sci. Rep.* **7**, (2017).

11. Reimer, M. E. *et al.* Bright single-photon sources in bottom-up tailored nanowires. *Nat. Commun. 2012 31* **3**, 1–6 (2012).

12. Versteegh, M. A. M. *et al.* Observation of strongly entangled photon pairs from a nanowire quantum dot. *Nat. Commun. 2014 51* **5**, 1–6 (2014).

13. Yu, P. *et al.* Nanowire Quantum Dot Surface Engineering for High Temperature Single Photon Emission. *ACS Nano* **13**, 13492–13500 (2019).

14. Leandro, L., Hastrup, J., Reznik, R., Cirlin, G. & Akopian, N. Resonant

excitation of nanowire quantum dots. *npj Quantum Inf. 2020 61* **6**, 1–5 (2020).

15. Laferrière, P. *et al.* Systematic study of the emission spectra of nanowire quantum dots. *Appl. Phys. Lett.* **118**, 161107 (2021).

16. Mäntynen, H., Anttu, N., Sun, Z. & Lipsanen, H. Single-photon sources with quantum dots in III–V nanowires. *Nanophotonics* **8**, 747–769 (2019).

17. Bulgarini, G. *et al.* Nanowire Waveguides Launching Single Photons in a Gaussian Mode for Ideal Fiber Coupling. *Nano Lett.* **14**, 4102–4106 (2014).

18. Gérard, J.-M., Mørk, J., Claudon, J., Gregersen, N. & Nielsen, T. R. Controlling the emission profile of a nanowire with a conical taper. *Opt. Lett. Vol. 33, Issue 15, pp. 1693-1695* **33**, 1693–1695 (2008).

19. Claudon, J. *et al.* A highly efficient single-photon source based on a quantum dot in a photonic nanowire. *Nat. Photonics* **4**, 174–177 (2010).

20. Reimer, M. E. *et al.* Bright single-photon sources in bottom-up tailored nanowires. *Nat. Commun.* **3**, 737 (2012).

21. Volatier, M., Duchesne, D., Morandotti, R., Arès, R. & Aimez, V. Extremely high aspect ratio GaAs and GaAs/AlGaAs nanowaveguides fabricated using chlorine ICP etching with N2-promoted passivation. *Nanotechnology* **21**, 134014 (2010).

5. Strategies for mitigation of excitonic fine structure splitting: piezoelectric actuators

5.1 The need of post-growth tuning mechanisms

Pyramidal quantum dots have shown a remarkable capability to be entangled photon sources: this stems for the symmetry of the dots, which is inherited from the original tetrahedral template thanks to the growth process: the reduced shape anisotropy implies a significant reduction of the excitonic fine structure splitting, which in turn allows for an easier generation of entangled photons without having to perform time gating[1,2].

However, minor fluctuations in the composition of the barriers, or strain field introduced during various processing steps, introduce random variations of the FSS from one dot to another, and while a high density of dots emitting entangled photons can be achieved[3], a way to increase up to unity both the yield of emitters and the fidelity of an individual one would be desirable.

Besides the problems related to the generation of entangled photons, small differences in the emission spectra wavelength between components of a dot ensemble tend to spoil the site controlled nature of PQDs, and ultimately imply that dots that have good properties must be looked for, their positions randomly distributed on the surface of a sample.

It is clear that optimisation of growth conditions can hardly be pushed further, and a post-growth tuning technique should be developed so that, given a single quantum dot, its emission spectrum can be shifted as will, and its symmetry fully restored in order to allow for the generation of entangled photons.

This has indeed been a very active research area in the community, and several strategies[4] have been developed to tackle these problems, such as thermal

annealing[5–7], or the application of external magnetic[8], electric[9], or more recently, strain fields[10–12]. The latter approach has several advantages, most notably that fact that it doesn't cause a reduction of the brightness as Stark effect would, nor introduces irreversible changes like annealing.

5.2 Strain in semiconductors

Strain is a pervasive effect in semiconductors: growth of materials with different lattice constants on top of each other will cause a straining, and the effect is so important that it determines the way the epitaxial material grows (e.g. Stranski-Krastanov or Volmer-Weber). While strain usually has a negative connotation, it can indeed be exploited to make self-assembled quantum dots, and the possibility of using it to tune the properties of semiconductor devices has given rise to a whole new field called *strain engineering*.

The effect of strain on the properties of a semiconductor can be intuitively grasped by thinking of the relationship between the lattice constant and the most important parameter of a semiconductor, that is, its bandgap: displacing the atoms from their minimum energy positions can cause an increase of the bandgap under compressive strain, or its reduction under tensile one.

The situation is obviously more complex in the case of a real semiconductor, which is a 3 dimensional and anisotropic system: first of all the relationship between the strain (that is, the deformation), and the stress that caused it (an applied force) is expected to be a tensor, and secondly different bands will react in different ways to the applied strain, depending on its direction, often resulting in a lifting of the degeneracies of band minima.

5.3 Fabrication of piezoelectric devices for strain tuning

The simplest device that can be built to tune quantum emitters is called a monolithic piezoelectric actuator: it is usually made of a PMN-PT 001 oriented membrane with a thickness of 300-500 µm onto whom the material containing the quantum dots is attached using a flip-chip bonder, using either an adhesive or thermocompressive bonding, although the latter approach has been determined to be less suitable for strain transfer[13]. PMN-PT (Lead Magnesium Niobate-Lead Titanate) is chosen because is a material with a high value for the d_{31} piezoelectric coefficient, meaning that a 001-oriented membrane will display a large in plane deformation when subjected to a longitudinal electric field. In the case of pyramidal QDs this was initially followed by the usual back-etching procedure to improve light extraction efficiency, as shown in fig 5.1.

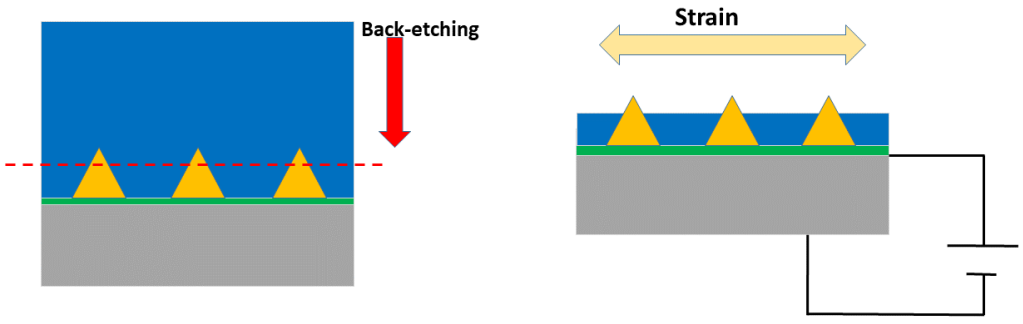


Figure 5.1 Fabrication process for a monolithic piezoelectric device. Back-etching is used to expose the tip of the pyramids in order to increase light extraction

Application of a voltage of hundreds of Volts between the two parallel faces of the PMN-PT crystal causes a (microscopic) deformation of the latter in the 3 dimensions, thus allowing for the generation and transfer of a biaxial strain to the attached GaAs membrane, and to the dots contained therein: this in

turn affects the dot's confining potential by affecting the band structure of the III-V material, and induces shifts of its emission spectrum.

As there is no way to control the orientation of applied strain, there is little way to use this approach to tune the fine structure splitting of a specific quantum dot in a controlled manner. To address this shortcoming, a more sophisticated version of this device was developed in Prof. Armando Rastelli's group in Linz, and in its last and more advanced incarnation is called a *six legs actuator.*



Figure 5.2 Sketch of a "six legs" device. Laser-defined cuts in PMN-PT membrane define 6 actuators. The top of the device is covered in gold to provide a shared ground, while the bottom is patterned to define 6 electrodes

This device is essentially a PMN-PT membrane, again of around 500 µm thickness, which has been laser-machined in order to have 6 cuts at 60 degrees with respect to each other, thus defining six triangular areas-the *legs* of the device. Gold is evaporated both on the top side of the device and, with a shadow mask, on the bottom, thus defining six contacts (fig. 5.2): while the top side is used as a ground electrode, the bottom electrodes are connected pairwise, so that when a voltage is applied two opposing legs can apply a compressive or tensile strain. As the device effectively acts as 3 independent piezoelectric actuators, it allows full control of the strain magnitude and direction in plane, and an independent tuning of the spectral shift.

In a way that is reminiscent of the fabrication of the so-called monolithic devices, we fabricated the first generation of six legs by bonding with a thin SU-8 layer a substrate containing the quantum dots to the piezoelectric material, and performing conventional back-etching. This, however, had some drawbacks: first of all, the delicate device was subjected to the aggressive mechanical thinning, but even more importantly there was a fundamental problem that prevented its correct operation, which had been seen in the monolithic devices, but became critical in this more complex system.

We have systematically observed, and it has been confirmed by simulations, that strain tends to relax in vertical structures, causing exposed pyramids to be much less reactive to the applied strain fields. Even worse, since the back-etching and the shape of the pyramids are not uniform, the effect of the applied strain seems to be quite uncontrollable, as the strain at the position of a specific quantum dot is as much dependent on the way it relaxes as it is on the direction it is applied along. In order to circumvent these problems, moving back to a planar geometry would be the best solution, but comes at the expense of a much greater fabrication complexity. The conundrum is the following: bonding the QD substrate in the usual way and not performing a back-etching does not yield a sufficiently high brightness to do any form of characterization, even if the wafer is thinned down, but the final chemical etching is not done to leave the pyramids embedded in the GaAs: indeed, even exciting the dot buried under several microns of GaAs can be challenging, and the site-controlled nature of PQDs would be concealed by the inability to see their positions using imaging systems.

If the substrate is bonded upside down, the thickness of the wafer (around 360 μm) prevents strain to be transferred up to the position of the dots, which would be close to the opposite surface, but light can be extracted more

efficiently, if the surface has been planarized to get rid of the recess and a solid immersion lens is used.

The best of both worlds can be achieved by employing the following procedure: first, a planarized substrate containing the QDs is bonded on a carrier substrate (GaAs or Silicon) using a PMGI-based resist such as SF19 or LOR30B. PMGI displays an exceptionally high thermal resistance, which makes it suitable to withstand the hard cure of the SU8 during the bonding step to the final device. The substrate is then thinned down to a thickness of only 20-30 µm, and bonded using a flip chip on a six legs device using SU8 as an adhesive and heating the whole ensemble above the SU8 glass transition temperature to allow for a complete resist reflow and wetting of the interface. Finally, the PMGI is removed by immersion in 1165 solvent, which does not attack (or only etches very slowly) hard-cured SU8, thus allowing for the removal of the carrier and exposure of the GaAs membrane, with the dots now located on the upper side.

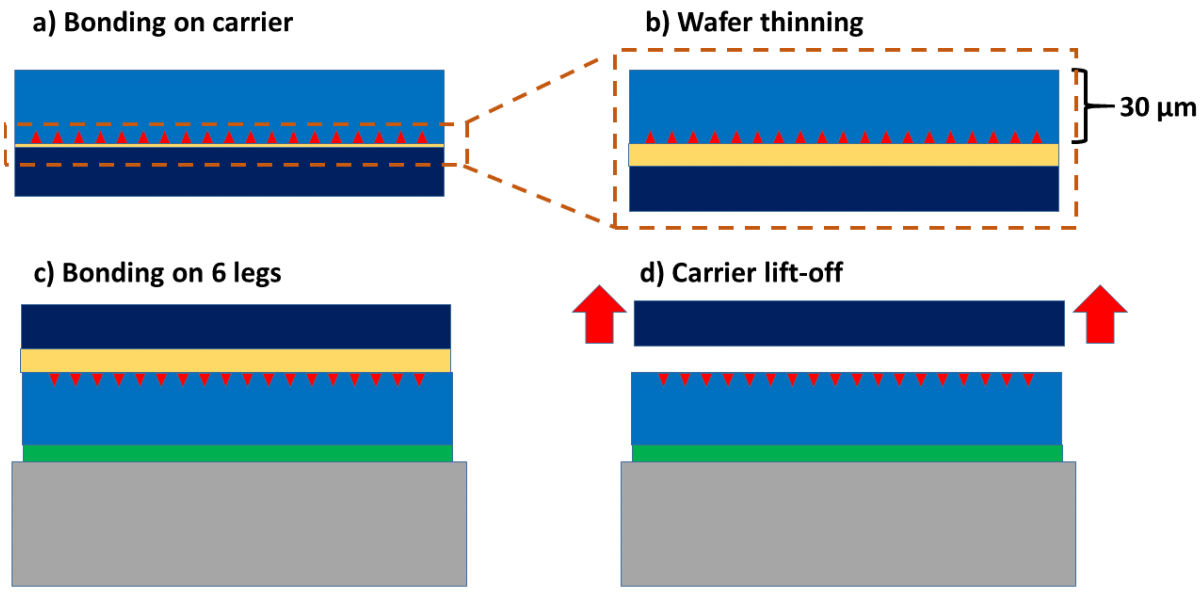


Figure 5.3 Sketch of the steps in the preparation of a "six legs" sample

This approach was successful in producing working devices, although the membrane was quite delicate and prone to breaking during measurements.

Moreover, not all the leg pairs of the 6 legs device responded in the same way, with one pair often being much more effective than the others: a behaviour we ascribe to a bonding issue originating during the resist reflow and to a tilt in the flip-chip machine used to bond the membrane to the device.

This in turn resulted in a limited ability to use one pair of legs to align the polarization direction of the excitons to the direction of another pair: a pre-requisite to fully erase the fine-structure splitting in a controllable way[11,13].

Nevertheless, by using various combinations of the legs actuators, tuning of the FSS over a relative large range of 10 µeV was achieved, as shown in figure 5.4.

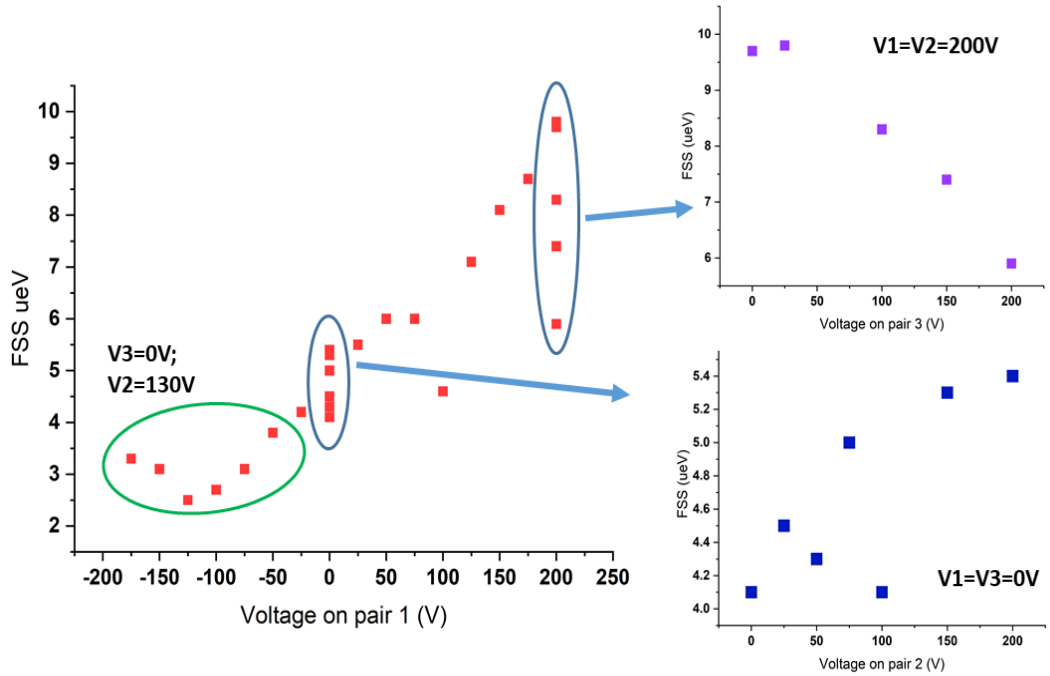


Figure 5.4 Dependence of the FSS for an individual quantum dots under strain tuning, for various voltages applied to the 3 leg pairs

While these results indicate that a strain tuning is possible, integrating piezoelectric materials into future quantum photonic platforms is challenging due to the fact, for example, that they often contain elements such as lead, which are considered contaminants for clean room environments and usually require dedicated processing tools. Also, while interesting results have been

obtained in the fabrications of micro actuators for this purpose[14], it looks like the technology is not compatible with the coupling to planar waveguides, unless used in combination with more complex processing techniques such as photonic wire bonding[15]: a more flexible approach would be desirable.

Indeed, during my PhD I developed an idea which, if proven correct, would allow to restore entanglement a posteriori using all (electro-)optical components, which is the topic of the following chapter.

1. Stevenson, R. M. *et al.* Evolution of entanglement between distinguishable light states. *Phys. Rev. Lett.* **101**, 170501 (2008).
2. Shooter, G. *et al.* 1GHz clocked distribution of electrically generated entangled photon pairs. *Opt. Express* **28**, 36838 (2020).
3. Juska, G., Dimastrodonato, V., Mereni, L. O., Gocalinska, A. & Pelucchi, E. Towards quantum-dot arrays of entangled photon emitters. *Nat. Photonics* **7**, 527–531 (2013).
4. Plumhof, J. D., Trotta, R., Rastelli, A. & Schmidt, O. G. Experimental methods of post-growth-tuning of the excitonic fine structure splitting in semiconductor quantum dots. *Nanoscale Res. Lett.* **7**, 336 (2012).
5. Langbein, W. *et al.* Control of fine-structure splitting and biexciton binding in <span class. *Phys. Rev. B* **69**, 161301 (2004).
6. Dubowski, J. J., Stanowski, R., Dalacu, D. & Poole, P. J. Precision tuning of InAs quantum dot emission wavelength by iterative laser annealing. *Opt. Laser Technol.* **103**, 382–386 (2018).
7. Rastelli, A. *et al.* In situ laser microprocessing of single self-assembled quantum dots and optical microcavities. *Appl. Phys. Lett.* **90**, 073120 (2007).
8. Stevenson, R. M. *et al.* Cancellation of fine-structure splitting in quantum dots by a magnetic field. *Phys. E Low-dimensional Syst. Nanostructures* **32**, 135–138 (2006).
9. Kowalik, K. *et al.* Influence of an in-plane electric field on exciton fine structure in InAs-GaAs self-assembled quantum dots. *Appl. Phys. Lett.* **86**, 041907 (2005).
10. Höfer, B. *et al.* Independent tuning of excitonic emission energy and decay time in single semiconductor quantum dots. *Appl. Phys. Lett.* **110**, 151102 (2017).

11. Trotta, R. *et al.* Wavelength-tunable sources of entangled photons interfaced with atomic vapours. *Nat. Commun.* **7**, 1–7 (2016).

12. Trotta, R. *et al.* Universal recovery of the energy-level degeneracy of bright excitons in ingaas quantum dots without a structure symmetry. *Phys. Rev. Lett.* **109**, 1–5 (2012).

13. Martín-Sánchez, J. *et al.* Strain-tuning of the optical properties of semiconductor nanomaterials by integration onto piezoelectric actuators. *Semiconductor Science and Technology* vol. 33 39 (2018).

14. Zhang, Y. *et al.* Monolithically Integrated Microelectromechanical Systems for On-Chip Strain Engineering of Quantum Dots. *Nano Lett.* **16**, 5785–5791 (2016).

15. Koos, C. *et al.* Photonic wire bonding: a novel concept for chip-scale interconnects. *Opt. Express, Vol. 20, Issue 16, pp. 17667-17677* **20**, 17667–17677 (2012).

6. A theoretical proposal for the a-posteriori mitigation of the effects of excitonic fine structure splitting

The following chapter describes a different approach for the restoral of polarization entanglement by manipulation of the relative phase of the emitted entangled photon pair instead of an erasure of the source's excitonic fine structure splitting, and will be presented in the form of the paper we have submitted reporting our findings.

An intuitive scheme for the restoration of entanglement for polarization-entangled photons emitted from quantum dots with non-vanishing fine structure splitting

SIMONE VARO[1*], GEDIMINAS JUSKA[1] AND EMANUELE PELUCCHI[1]

1 *Tyndall National Institute, University College Cork, Dyke Parade, Cork, Republic of Ireland*
**Simone.varo@tyndall.ie*

Abstract: Generation of polarization-entangled photons from quantum dots via the biexciton-exciton recombination cascade is complicated by the presence of an energy splitting between the intermediate excitonic levels, which severely degrades the quality of the entangled photon source. In this paper we present a novel, conceptually simple and straightforward proposal for restoring the entanglement of said source by applying a cascade of time-dependent operations on the emitted photons. This is in striking contrast with the techniques usually employed, that act on the quantum emitter itself in order to

remove the fine structure splitting at its root. The feasibility of the implementation with current technology is discussed, and the robustness of the proposed compensation scheme with respect to imperfections of the experimental apparatus is evaluated via a series of Monte Carlo simulations.

Introduction

Quantum dots (QDs) have emerged as one of the most promising candidates for on-demand generation of non-classical light, due to their ability to generate single photons[1–3] and even entangled ones[4–7], especially via the biexciton-exciton recombination cascade mechanism[8].

The presence of a fine structure splitting (FSS) between the intermediate excitonic levels[9,10] has been for years the most severe obstacle in the generation of high quality polarization-entangled photon pairs: in a textbook example of Noether's theorem, the degeneracy of the levels is promptly lifted not only due to shape anisotropy but even because of disorder in the alloy of the barriers of the dot, or strain and piezoelectrically induced electric fields which reduce the symmetry of the confinement potential[11]. This causes a residual FSS to appear even in highly symmetrical dots[12], in spite of significant improvements in growth techniques that helped to reduce it significantly in recent years[13–17].

Several approaches have been proposed to tackle this issue at its root[18], i.e. relying on the application of external tuning mechanisms in the form of the electric[19] and optical Stark effect[20], and magnetic[21] or strain[22–24] fields in order to restore the symmetry and remove the source of the problem, or by annealing of the quantum dot to mitigate the severity of the effect[25]. While several attempts have been made to integrate the most successful of these solutions on semiconductor platforms in order to achieve compact and scalable entangled photon sources[24], this usually implies a significant increase in fabrication complexity, a limited yield in terms of working dots and devices, or

brings in new problems such as the quenching of the photoluminescence when electric field tuning is employed.

Most of these attempts undertaken to restore the quality of the emitted entangled photons, however, start from the assumption that the degradation of the entanglement properties of the source is an irreversible process, and thus focus on removing the FSS. A posteriori solutions to mitigate FSS effects after the photons have been emitted are possible, but only a few proposal in this sense have emerged so far[26–31] and, to our knowledge, none of them has been experimentally implemented at the time of this paper being written. Moreover, it looks like most of these proposals start by identifying the energy difference of the photons, inherited by the excitonic FSS of the quantum dot, as the issue to tackle: the underlying assumption is that such a difference makes the two possible decay channels of the biexciton-exciton cascade distinguishable[6,28,32,33], thus breaking quantum superpositions in the final state. Indeed, the idea that the existence of a "which-path" information is the root of polarization entanglement degradation was widely accepted in the community in the past, and it would stand to reason in such a framework that performing a quantum erasure by restoring energy degeneracy of the photons before any measurement is done would yield perfectly entangled states. However, the now widely accepted mechanism via which FSS impacts on the generation of entangled photons via the biexciton-exciton recombination cascade was later discussed in detail by Stevenson et al. in their seminal paper[34], and will be briefly recalled in order to establish the theoretical framework and notation used in the rest of our paper.

Let |XX> indicate the biexcitonic (electronic) state of the quantum dot, and $|X_H>$ and $|X_V>$ the two intermediate excitonic states, with energies E_X^H and E_X^V, as shown in figure 6.1. If the emitter is populated with a biexciton (e.g. via a two-photon resonant pumping scheme), it will decay after a time t_1 leading to an exciton-photon entangled state of the form $|\psi> \alpha(|H_{XX}X_H>+|V_{XX}X_V>)$,

where $|H_{XX}>$ and $V_{XX}>$ respectively denote a horizontally and vertically polarized photon emitted during the biexciton to exciton transition.

Before the completion of the recombination cascade, marked by the exciton to ground state transition after a temporal delay t_2, a different energy of the two intermediate levels, that is, the presence of an FSS, will lead to a different time evolution of the excitonic states as per the time-dependent solution of the Schrödinger equation:

$$|\Psi(t)>=\alpha(|H_{XX}X_H>* e^{i(E_X^H*t)/\hbar}+|V_{XX}X_V>* e^{i(E_X^V*t)/\hbar}) \quad (1)$$

With the resulting phase accumulated in this interval finally transferred to the two photons state resulting from the overall cascade, which, neglecting global phase terms can be written as:

$$|\psi>=\alpha\,(|H_{XX}H_X>+e^{i(FSS*t_2)/\hbar}|V_{XX}V_X>) \quad (2)$$

With $|H_X>$ and $|V_X>$ being the horizontally and the vertically polarized photons emitted during this second transition.

As it can be seen, the state is still an entangled one, albeit not the Bell state that would be produced should the FSS be zero. The random nature of the interval t_2 that precedes the recombination of the exciton implies that while the dot would always emit entangled photon pairs, the state each pair would be entangled to will be a (different) random one, effectively mimicking, in a statistical sense, classical light, and making such a source relatively useless for practical applications should the FSS be sufficiently large to broaden the distribution of the generated states[35]. Post selection techniques based on time-gating are possible, and allow the discard of photon pairs generated for longer values of the recombination time t_2 where the phase build-up causes a significant drift of the state from the maximally entangled Bell one: the obvious downside is that a trade-off has to be reached between the desired level of

entanglement and the amount of acceptable losses. For instance, sometimes the fraction of acceptable photons drops to a few percentage points[36] of the overall emission from the quantum dot.

However, as each emitted state is already an entangled one, the problem of restoring the quality of the entanglement of the source could be reformulated as the search for a unitary transformation that merely transforms, a posteriori, any of these states to a predetermined one, thus removing statistical fluctuations.

As discussed before, most approaches present in the literature have focussed on shifting the energy of the two polarization states of the emitted photons so that they become degenerate after the emission. The approach we hereby propose however, builds directly on the theoretical framework developed by Stevenson and that we have recalled, and starts by considering the difference in phase and not in energy between the two excitonic photon states as the issue to tackle.

Results and discussion

Determination of the conditions for entanglement restoral

Let's assume that both the biexciton and the exciton photons fly across a device which has the ability to impart a phase which is both different depending on the polarization and wavelength and changing linearly in time, so that we can write the phases introduced on either polarization of the photons as:

$$\Phi_{V_{XX}}(t) = K_{V_{XX}} * t + \Phi^0_{V_{XX}} \qquad \Phi_{V_X}(t) = K_{V_X} * t + \Phi^0_{V_X}$$

$$\Phi_{H_{XX}}(t) = K_{H_{XX}} * t + \Phi^0_{H_{XX}} \qquad \Phi_{H_X}(t) = K_{H_X} * t + \Phi^0_{H_X} \tag{3}$$

With the various K representing the slopes of the introduced phases for a given polarization and wavelength of a photon and the Φ^0 terms indicating the

constant (that is, time independent) phases introduced by the compensation system.

In general, if we assume the zero of our time scale to correspond with the initialization of the biexciton, the state resulting from such an operation can be written as a function of the time intervals t_1 and t_2 (with t_1 and t_2 being the random times before the emission of the biexciton and of the exciton photons, respectively) as:

$$\begin{aligned} &|H_{XX}> e^{(i*\Phi_{H_{XX}}*(t_1+t_{prop}{}^{XX}-t_{start}{}^{XX}))} \otimes |H_X> e^{(i*\Phi_{H_X}(t_1+t_2+t_{prop}{}^{X}-t_{start}{}^{X}))} + \\ &+|V_{XX}> e^{(i*\Phi_{V_{XX}}(t_1+t_{prop}{}^{XX}-t_{start}{}^{XX}))} \otimes |V_X> e^{(i*\Phi_{V_X}(t_1+t_2+t_{prop}{}^{X}-t_{start}{}^{X}))} * e^{(i*FSS*t_2/\hbar)} \end{aligned} \quad (4)$$

Where $t_{prop}^{X,XX}$ (*prop* being short for propagation) is the time of flight of the biexciton (exciton) photon from the quantum dot to the entrance of the compensation system, and $t_{start}^{X,XX}$ is the time at which the ramping of the differential phases begins. With our choice of the zero of the time scale, we will thus have that if $t_{prop}^{XX} = t_{start}^{XX}$, the phase ramp for the biexciton photon will start when an XX photon emitted at t=0 (immediately after the dot has been excited) will reach the compensation system .

Substituting relations (3) and collecting all terms we can get an overall state of the form:

$$|H_{XX}H_X> + e^{i\Phi(t)}|V_{XX}V_X>,$$

With

$$\begin{aligned} &\Phi(t) = (K_{V_{XX}} - K_{H_{XX}} + K_{V_X} - K_{H_X})*t_1 + (K_{V_X} - K_{H_X} + \frac{FSS}{\hbar})*t_2 + \\ &+(K_{V_{XX}} - K_{H_{XX}})*\left(t_{prop}^{XX} - t_{start}^{XX}\right) + \left(K_{V_X} - K_{H_X}\right)*\left(t_{prop}^{X} - t_{start}^{X}\right) + \\ &+(\Phi_{V_{XX}}^0 - \Phi_{H_{XX}}^0 + \Phi_{V_X}^0 - \Phi_{H_X}^0) \end{aligned}$$

From this, conditions *so that the phase term no longer depends on random variables* t_1 *and* t_2 can be straightforwardly determined:

$$K_{V_X} - K_{H_X} = -\frac{FSS}{\hbar} \qquad (5)$$

$$\left(K_{V_{XX}} - K_{H_{XX}}\right) = -\left(K_{V_X} - K_{H_X}\right) \qquad (6)$$

If these conditions are met, the final 2 photon state resulting from the quantum dot emission after the compensation system will always be the same for each biexciton-exciton photon pair, as all of the other terms depend only on experimental parameters, such as the time of flight, that are assumed to remain constant over time: this implies that this residual constant phase term does not infringe on the resulting degree of entanglement, but merely changes the pure state all the photons pair will be entangled to, and can be easily compensated for using an additional static (i.e. non time-dependent) quantum gate.

Figure 6.1 provides a graphical and intuitive representation of the workings of the scheme we are proposing and of the conditions we have derived, in an ideal case where the other phase terms are simply assumed to be zero and the ramps are perfectly synchronized (these hypothesis are not necessary for the scheme to work, but merely simplify our analysis): condition (6) implies that the phase differences imparted between the two $|H_{XX}H_X>$ and $|V_{XX}V_X>$ by the operation on the biexciton line and that on the exciton line are equal but opposite. Provided the differential phase ramps are synchronized, the differential phase introduced on the biexciton photon emitted at t_1 will be perfectly compensated when the exciton photon, emitted at $t_1 + t_2$, crosses the compensation system. Likewise, condition (5) will ensure that the phase introduced by the evolution of the state due to the FSS is compensated as well when the exciton photon crosses the compensation system we have described. This removes the randomness of the final state.

Notably, one important advantage of this differential compensation approach is its insensitivity to any jitter present in the system, including those related to the excitation scheme employed, and to the starting point of the ramps, which as discussed before would only determine the final entangled state, but not the

degree of entanglement (concurrence) of the source. Moreover, since all photon pairs will be transformed to the target state and none discarded, the technique we are proposing is in principle a lossless one: a major improvement with respect to time-gating techniques.

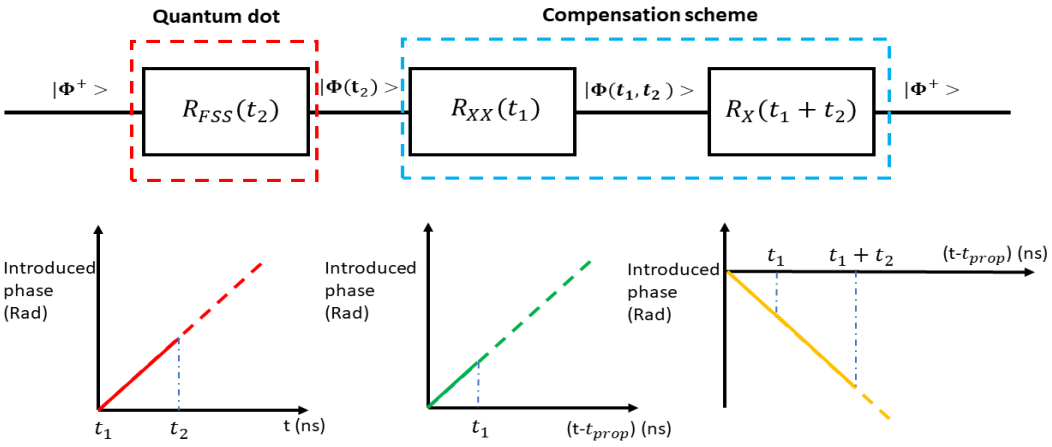


Figure 6.1 Circuit model representation of the overall temporally-phase evolution in the proposed compensation scheme: spin precession inside the quantum dot causes the build-up of a phase dependent on random time t_2 .After emission, the effect of the scheme on the biexitonic part of the state adds another phase jump dependent on t_1 (emission time of the biexciton photon) when the XX photon crosses the system at time $t_1 - t_{prop}$. Both phase terms are compensated by the operation of the excitonic part of the wavefunction, if the proper conditions are met, when the exciton photon is imparted an opposite phase at time $t_1 + t_2 - t_{prop}$. Note that we have assumed $t_{prop}^{XX} = t_{prop}^{X} = t_{start}^{XX} = t_{start}^{X}$ for simplicity

We can also observe that from a quantum circuit perspective, the scheme hitherto proposed is equivalent to a cascade of two temporally-dependent phase gates, one operating on the biexciton and one operating on the exciton photon: in this model, the degradation of the entanglement due to the FSS is equivalent to the action of a phase gate $R_{FSS}(t_2)$, which turns what would otherwise be a perfect Bell state into a random one, $|\Phi(t_2)\rangle$ If the conditions we have derived

are fulfilled, the sequential action of the two phase gates $R_{XX}(t_1)$ and $R_X(t_1+t_2)$ would compensate the effect of the first phase gate, and result in the recovery of the original Bell state $|\Phi^+\rangle$. It should be noted that the scheme (and subsequent proposed implementation) we are proposing are somewhat similar to the one suggested by Wang et al. in their paper[30]. Their formalism however adopted a frequency domain approach, focused on the removal of the energy difference between the two excitonic photon, and neglected the effect of other, time-independent phase terms on the outcome state. We believe our approach to provide a more natural, elegant, physically complete and simple to grasp picture, which especially in view of its circuit model interpretation could be easily applied to photonic quantum circuit design. Obviously, however, if one considers only frequency translation[37], the two can be seen as rather complementary: in fact, our solution will restore the energy degeneracy as well, and the two formalisms can be easily reconciled in the framework of signal theory using the concept of instantaneous angular frequency[38].

If we define the energy scale according to figure 6.2, we will have that:

$$\omega_X^V = \frac{E_X}{\hbar} + \frac{FSS}{2\hbar}$$

$$\omega_X^H = \frac{E_X}{\hbar} - \frac{FSS}{2\hbar} \tag{7}$$

For an angle modulated wave s(t)=Acos($\omega_c t + \vartheta(t)$)=Acos(Φ(t)), phase modulation will introduce an instantaneous angular frequency defined as $\omega_i(t) = \frac{d\Phi(t)}{dt}$, so that in our case, for a signal affected by the ramp, we will have:

$$\omega_X^V(t) = \omega_X^V + K_V$$

(8)

$$\omega_X^H(t) = \omega_X^H + K_H$$

And substituting equation 5 we will have that $\omega_X^V(t) - \omega_X^H(t) = 0$, which implies that the resulting photons will also be degenerate, and that the two approaches are consistent with each other. Indeed, the resulting state will be entangled in both polarization and energy, but we stress that, while the two effects (of phase correction and frequency translation) cannot be decoupled, what is needed to restore polarization entanglement is exclusively the phase correction, and the frequency translation should be regarded in principle as a side effect. Our discussion in the final part of our manuscript (see fig. 6.4) will help clarify that a simple frequency correction (ref 30) will not in general deliver a state whose fidelity to the ideal Bell state is unitary.

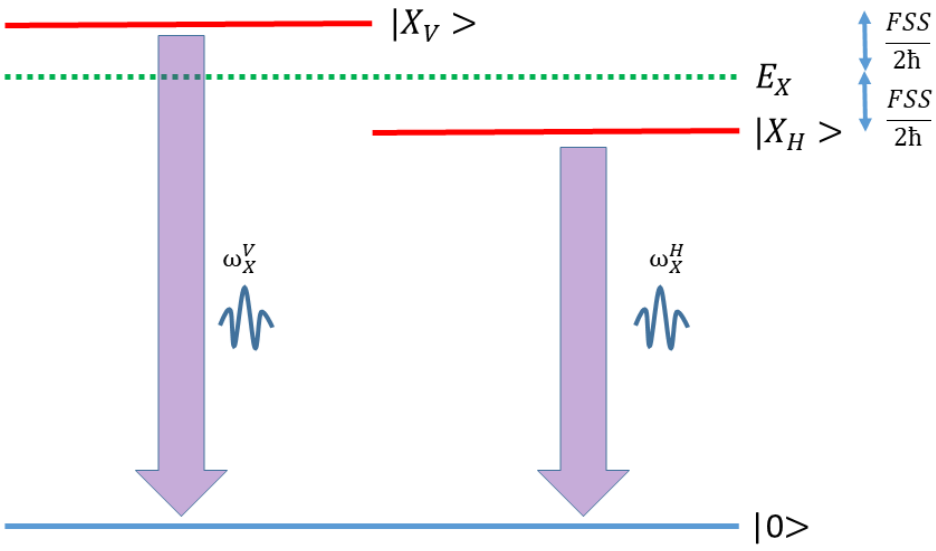


Figure 6.2 Graphical representation of the excitonic levels and fine-structure splitting. The zero in the energy scale is assumed to be the ground state

Proposed implementation and feasibility analysis

In deriving the conditions that allow to restore the entanglement of the source, we have not made any assumption on the nature of the system that is supposed to implement them. It is quite obvious however that a natural realization of such a scheme could be based on the Pockels effect, as was also proposed in ref. [30]: a birefringent crystal would introduce a phase difference between polarizations aligned along the two optical axes, and the application of a transversal external electric field would allow to tune such a phase difference and change it in time by modifying the material's index ellipsoid: electro-optical phase modulators are indeed devices designed for this specific purpose, and that could be employed to implement our proposal.

For instance, in the most widely used material, $LiNbO_3$, the relationship between the applied field and the variation of the refractive index is described by the tensor[39]:

$$r_{i,k} = \begin{bmatrix} 0 & -r_{22} & r_{13} \\ 0 & r_{22} & r_{13} \\ 0 & 0 & r_{33} \\ 0 & r_{51} & 0 \\ r_{51} & 0 & 0 \\ -r_{22} & 0 & 0 \end{bmatrix} \tag{9}$$

So that variations of the refractive index with the application of an external electric field can be written, in first approximation, as:

$$\Delta n_i = -\frac{n_i^3}{2}\sum_{k=1}^{3} r_{ik} E_k \tag{10}$$

Application of an external field in the z direction will affect the ordinary and extraordinary refractive indexes in a different way, owing to the different terms involved in the tensor product, and thus allow for an externally controlled (and potentially temporally-varying) phase gate.

Once the FSS, which is a property of the dot and can be measured experimentally is known, the relationship between the slope of the voltage ramp and the FSS can be easily determined in order to fulfill condition (5), while

condition (6) can in turn be easily fulfilled by employing two phase modulators operated with opposite voltage ramps, one affecting the biexciton photon while the other affects the exciton, as shown in figure 6.3.

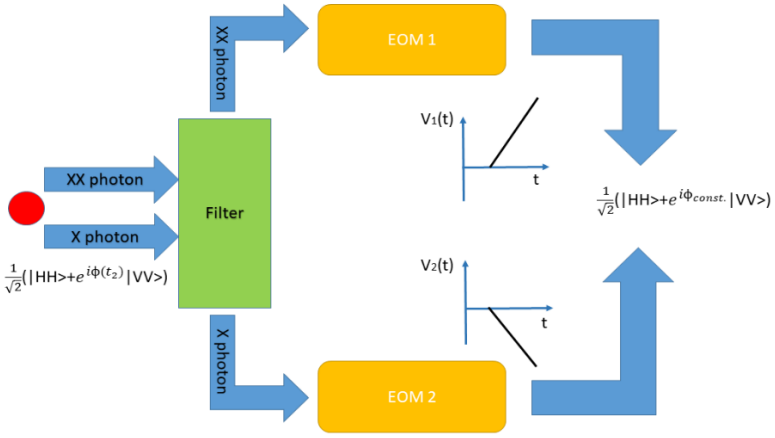


Figure 6.3 proposed implementation of the compensation scheme using two electo-optic modulators operated in a parallel configuration, as also envisioned by Wang et al.

A travelling wave, velocity matched phase modulator is conveniently characterized by its half-wave voltage V_π that is, the value of the applied voltage that induces a phase shift of π on a wave travelling through it. As the electro-optic coefficients are different for the two axes, we can denote with V_π^V and V_π^H the values of V_π for a V- and H-polarized wave respectively. The induced phase shift of a photon wave packet entering the modulator at time t for either polarization can then be easily written as $\Phi^{V,H}(t)=\frac{V(t)}{V_\pi^{V,H}}*\pi$

If the voltage is varying linearly in time, we can calculate the slope of induced phase by trivially taking the time derivative of this expression, and easily rewrite equation 5 as:

$\frac{dV}{dt}(\frac{1}{V_\pi^V}-\frac{1}{V_\pi^H})*\pi=-\frac{FSS}{\hbar}$ to determine the slope of the voltage ramp.

If for instance we consider again a z-cut $LiNbO_3$ integrated EOMs, and assume a V_π of 3 Volts for the TM mode and a 3 times larger a V_π for the TE modes,

we will get a slope of the voltage ramp $\frac{dV}{dt}$ of around 2 V/(ns*μeV), which appears to be within the capabilities of modern high frequency EOMs if only a FSS of a few μeV has to be corrected, as it customarily found in dots grown on high symmetry substrates[13,14].

This implies that the proposed scheme can indeed be implemented with currently available technology, while advances in electro-optic material science[40] and integration[41] can pave the way for the development of compact quantum photonic circuits that perform a similar task and push the performance much further.

Sensitivity to imperfections of the compensation scheme

In order to estimate the robustness of our approach to imperfections of the setup, a simple Monte Carlo simulation was performed, generating density matrixes for different values of the mismatches

$$\Delta\omega_1 = K_{V_X} - K_{H_X} - \frac{FSS}{\hbar}$$

(11)

$$\Delta\omega_2 = K_{V_{XX}} - K_{H_{XX}} + K_{V_X} - K_{H_X}$$

This was done by first of all assuming that $t_{prop}^{XX} = t_{start}^{XX}$ and $t_{prop}^{X} = t_{start}^{X}$, that is, a perfect syncing of the start of the ramp with the laser pulse, and by ignoring every other constant phase term. By creating random values for variables t_1 and t_2, a large number of density matrixes was generated and averaged until a suitable convergence was reached. In all of these simulations we have assumed a lifetime of the exciton state X of 1 ns, and half of that for the biexciton state,

as it is often the case for III-V semiconductor quantum dots, and the FSS was chosen to be 3 μeV (corresponding to a spin precession of around 4.6 Rad/ns).

Figure 6.4 shows the behaviour of the concurrence of the resulting density matrixes and their fidelity to the Bell state $|\Phi^+>=\frac{1}{\sqrt{2}}\left(|HH\rangle+|VV\rangle\right)=\frac{1}{\sqrt{2}}\left(|00\rangle+|11\rangle\right)$ as a function of the errors $\Delta\omega_1$ and $\Delta\omega_2$: it can be observed that $\Delta\omega_2$ has a less severe impact due to the term being weighted by the random variable t_1, which is related to the shorter lifetime of the biexciton. For comparison, without the compensation scheme applied the same quantum dot would exhibit a fidelity and concurrence of 0.52 and 0.21 respectively. It can be also noticed that while t_1, the time that passes between the excitation of the quantum dot and the emission of the biexciton photon, plays no role in the level of the entanglement without our compensation scheme, it becomes important when the latter is applied: this is due to the differential phase gates being dependent on t_1 and t_1+t_2.

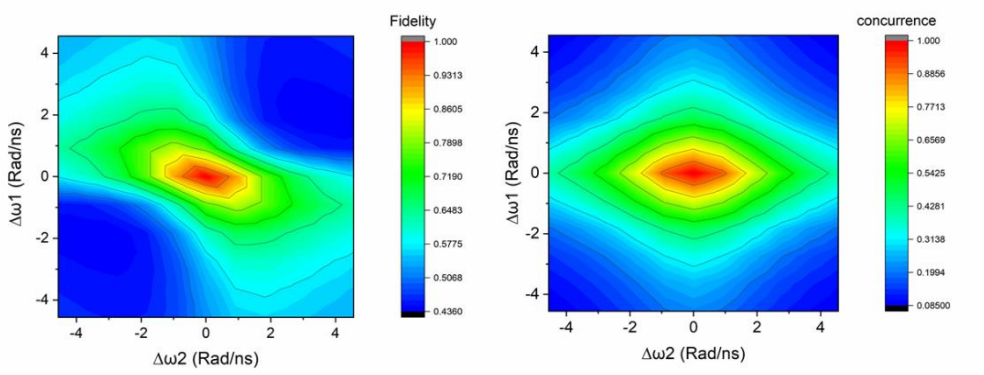


Figure 6.4 Fidelity (left) and Concurrence (right) of the state obtained after the compensation scheme for a dot with an FSS of 3 μeV, as a function of the errors $\Delta\omega_1$ and $\Delta\omega_2$. All of the other time-independent phase terms are assumed to be 1 for simplicity.

In order to also understand the impact of the constant phase term, a new series of simulations was performed. In this case, conditions to perfectly restore the entanglement of the state have been assumed to be fulfilled ($\Delta\omega_1=\Delta\omega_2=0$),

and concurrence and fidelity to the states $|\Phi^+>$ and $|\Phi^->$ were calculated as a function of the time delay $\delta t=\left(t_{prop}^{XX}-t_{start}^{XX}\right)-\left(t_{prop}^{X}-t_{start}^{X}\right)$, again for a quantum dot having a 3 μeV FSS.

As can be seen from figure 6.5, this has no effect on the level of concurrence, and thus on the degree of entanglement, but it can be exploited to finely tune the final state which is generated by the application of the compensation scheme.

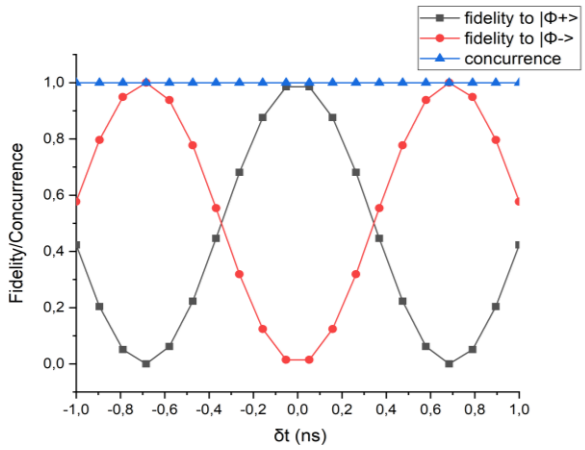


Figure 6.5 Fidelity to the Bell states and concurrence of the density matrix obtained after the compensation scheme as a function of temporal detuning δt in case of a perfect compensation of the FSS

In conclusion, we proposed a conceptually simple and intuitive way to compensate the effects of FSS on entanglement quality.

Conclusions

The scheme we have discussed for restoring the entanglement of photons emitted from quantum dots using the biexciton-exciton recombination cascade appears to be quite robust, flexible and powerful, and it appears to be possible to implement it with currently available technology. As the implementation we have suggested is based on the repurposing of devices already widely employed in the (classical) field of information technology and telecommunications, it represents an elegant solution that could significantly lower infrastructural costs

associated with a “quantum internet”. This is especially true since in principle no photon losses are introduced by our approach, which would result result in a higher bitrate Moreover, by introducing the paradigm shift of a-posteriori compensation of the effect of the FSS, constraints on the sources that could be employed for such a purpose are significantly relaxed, and fabrication of devices integrating semiconductor quantum dots as entangled photon sources for quantum information processing are simplified.

Methods

Monte Carlo simulations were performed using a custom-written Python code. Large numbers of density matrixes were generated and averaged until a suitable convergence was reached, defined as a less than 10^{-6} relative change in the matrix elements from the previous iteration.

Fidelity of the converged density matrixes to any Bell state was calculated as:

$$F = \left(Tr\left(\sqrt{\sqrt{\rho_B} * \rho * \sqrt{\rho_B}} \right) \right)^2$$

Where we have used ρ_B and ρ to indicate the density matrix of the target Bell state and the one resulting from our simulation, respectively.

Concurrence was calculated using the standard formula:

$$C(\rho)=\max\left(0, \lambda_1 - \lambda_2 - \lambda_3 - \lambda_4\right)$$

With λ_n being the square roots of the eigenvalues, in decreasing order, of the operator $R = \rho\Sigma\rho^T\Sigma$, and $\Sigma = \begin{pmatrix} 0 & 0 & 0 & -1 \\ 0 & 0 & 1 & 0 \\ 0 & 1 & 0 & 0 \\ -1 & 0 & 0 & 0 \end{pmatrix}$

Author contribution

S.V. conceived the idea and developed the code used to simulate the density matrixes with assistance from G.J. E.P supervised the work and assisted in writing the manuscript. All authors reviewed the manuscript.

Acknowledgments

This research was supported by Science Foundation Ireland under Grant Nos. 15/IA/2864, SFI-18/SIRG/5526, and 12/RC/2276_P2 .

Additional Information

The authors declare no competing interests.

Data availability

Our simulations have been performed using a custom-written code in the 3.7 version of the Python language. The code uses the *Scipy* and *Numpy* Python libraries, and was run via the *Anaconda* Python distribution, with typical computation times of less than 2 hours on a 3.4 GHz quad-core Intel i3 machine with 16 Gbyte of RAM. All code is available free of charge upon request.

References

1. Arakawa, Y. & Holmes, M. J. Progress in quantum-dot single photon sources for quantum information technologies: A broad spectrum overview. *Applied Physics Reviews* vol. 7 21309 (2020).
2. Somaschi, N. *et al.* Near-optimal single-photon sources in the solid state. *Nat. Photonics* **10**, 340–345 (2016).
3. Senellart, P., Solomon, G. & White, A. High-performance semiconductor

quantum-dot single-photon sources. *Nat. Nanotechnol.* | **12**, (2017).

4. Shields, A. J. Semiconductor quantum light sources. *Nat. Photonics* **1**, 215–223 (2007).

5. Orieux, A., Versteegh, M. A. M., Jöns, K. D. & Ducci, S. Semiconductor devices for entangled photon pair generation: A review. *Reports on Progress in Physics* vol. 80 076001 (2017).

6. Akopian, N. *et al.* Entangled photon pairs from semiconductor quantum dots. *Phys. Rev. Lett.* **96**, 130501 (2006).

7. Schwartz, I. *et al.* Deterministic generation of a cluster state of entangled photons. *Science (80-.).* **354**, 434–437 (2016).

8. Yamamoto, Y., Santori, C. & Pelton, M. Regulated and entangled photons from a single quantum dot. *Phys. Rev. Lett.* **84**, 2513–2516 (2000).

9. Gong, M., Zhang, W., Guo, G. C. & He, L. Exciton polarization, Fine-structure splitting, and the asymmetry of quantum dots under uniaxial stress. *Phys. Rev. Lett.* **106**, 227401 (2011).

10. Abbarchi, M. *et al.* Fine structure splitting of quantum dot excitons: Role of geometry and environment. *Phys. E Low-Dimensional Syst. Nanostructures* **42**, 881–883 (2010).

11. Bayer, M. *et al.* Fine structure of neutral and charged excitons in self-assembled In(Ga)As/(Al) GaAs quantum dots. *Phys. Rev. B - Condens. Matter Mater. Phys.* **65**, 1953151–19531523 (2002).

12. Juska, G., Dimastrodonato, V., Mereni, L. O., Gocalinska, A. & Pelucchi, E. Towards quantum-dot arrays of entangled photon emitters. *Nat. Photonics* **7**, 527–531 (2013).

13. Huber, D. *et al.* Highly indistinguishable and strongly entangled photons from symmetric GaAs quantum dots. *Nat. Commun.* **8**, 15506 (2017).

14. Gurioli, M., Wang, Z., Rastelli, A., Kuroda, T. & Sanguinetti, S. Droplet epitaxy of semiconductor nanostructures for quantum photonic devices. *Nature Materials* vol. 18 799–810 (2019).

15. Basso Basset, F. *et al.* High-Yield Fabrication of Entangled Photon Emitters for Hybrid Quantum Networking Using High-Temperature Droplet Epitaxy. *Nano Lett.* **18**, 505–512 (2018).

16. Chung, T. H. *et al.* Selective carrier injection into patterned arrays of pyramidal

quantum dots for entangled photon light-emitting diodes. *Nat. Photonics* **10**, 782–787 (2016).

17. Skiba-Szymanska, J. *et al.* Universal Growth Scheme for Quantum Dots with Low Fine-Structure Splitting at Various Emission Wavelengths. *Phys. Rev. Appl.* **8**, 014013 (2017).

18. Plumhof, J. D., Trotta, R., Rastelli, A. & Schmidt, O. G. Experimental methods of post-growth-tuning of the excitonic fine structure splitting in semiconductor quantum dots. *Nanoscale Res. Lett.* **7**, 336 (2012).

19. Kowalik, K. *et al.* Influence of an in-plane electric field on exciton fine structure in InAs-GaAs self-assembled quantum dots. *Appl. Phys. Lett.* **86**, 041907 (2005).

20. Muller, A., Fang, W., Lawall, J. & Solomon, G. S. Creating polarization-entangled photon pairs from a semiconductor quantum dot using the optical stark effect. *Phys. Rev. Lett.* **103**, 217402 (2009).

21. Stevenson, R. M. *et al.* A semiconductor source of triggered entangled photon pairs. *Nature* **439**, 178–182 (2006).

22. Trotta, R. *et al.* Universal recovery of the energy-level degeneracy of bright excitons in ingaas quantum dots without a structure symmetry. *Phys. Rev. Lett.* **109**, 1–5 (2012).

23. Martín-Sánchez, J. *et al.* Strain-tuning of the optical properties of semiconductor nanomaterials by integration onto piezoelectric actuators. *Semiconductor Science and Technology* vol. 33 39 (2018).

24. Zhang, Y. *et al.* Monolithically Integrated Microelectromechanical Systems for On-Chip Strain Engineering of Quantum Dots. *Nano Lett.* **16**, 5785–5791 (2016).

25. Ellis, D. J. P. *et al.* Control of fine-structure splitting of individual InAs quantum dots by rapid thermal annealing. *Appl. Phys. Lett.* **90**, 011907 (2007).

26. Stace, T. M., Milburn, G. J., Milburn, G. J. & Barnes, C. H. W. Entangled two-photon source using biexciton emission of an asymmetric quantum dot in a cavity. *Phys. Rev. B - Condens. Matter Mater. Phys.* **67**, 085317 (2003).

27. Jones, N. S. & Stace, T. M. Photon frequency-mode matching using acousto-optic frequency beam splitters. *Phys. Rev. A - At. Mol. Opt. Phys.* **73**, 033813 (2006).

28. Coish, W. A. & Gambetta, J. M. Entangled photons on demand: Erasing which-path information with sidebands. *Phys. Rev. B - Condens. Matter Mater. Phys.* **80**, 241303 (2009).

29. Zhou, Z. Q. *et al.* Phase compensation enhancement of photon pair entanglement generated from biexciton decay in quantum dots. *Phys. Rev. A - At. Mol. Opt. Phys.* **81**, 064302 (2010).

30. Wang, X. Bin, Yang, C. X. & Liu, Y. B. On-demand entanglement source with polarization-dependent frequency shift. *Appl. Phys. Lett.* **96**, 201103 (2010).

31. Fognini, A., Ahmadi, A., Daley, S. J., Reimer, M. E. & Zwiller, V. Universal finestructure eraser for quantum dots. *Opt. Express* vol. 26 24487–24496 (2018).

32. Meirom, E. A. *et al.* Distilling entanglement from random cascades with partial 'which path' ambiguity. *Phys. Rev. A - At. Mol. Opt. Phys.* **77**, 062310 (2008).

33. Pfanner, G., Seliger, M. & Hohenester, U. Entangled photon sources based on semiconductor quantum dots: The role of pure dephasing. *Phys. Rev. B - Condens. Matter Mater. Phys.* **78**, 195410 (2008).

34. Stevenson, R. M. *et al.* Evolution of entanglement between distinguishable light states. *Phys. Rev. Lett.* **101**, 170501 (2008).

35. Juska, G. *et al.* Conditions for entangled photon emission from (111)B site-controlled pyramidal quantum dots. *J. Appl. Phys.* **117**, 134302 (2015).

36. Shooter, G. *et al.* 1GHz clocked distribution of electrically generated entangled photon pairs. *Opt. Express* **28**, 36838 (2020).

37. Wu, Z. & Grbic, A. Serrodyne Frequency Translation Using Time-Modulated Metasurfaces. *IEEE Trans. Antennas Propag.* **68**, 1599–1606 (2020).

38. Alencar, M. S. & da Rocha, V. C. Angle Modulation. in *Communication Systems* 197–224 (Springer US, 2005). doi:10.1007/0-387-27097-3_6.

39. Saleh, B. E. A. & Teich, M. C. *Fundamentals of Photonics*. (John Wiley & Sons, Inc., 1991). doi:10.1002/0471213748.

40. Liu, J. *et al.* Recent advances in polymer electro-optic modulators. *RSC Advances* vol. 5 15784–15794 (2015).

41. Luo, K. H. *et al.* Nonlinear integrated quantum electro-optic circuits. *Sci. Adv.* **5**, eaat1451 (2019)

7.TEM analysis of pyramidal quantum dots

One of the most striking features of pyramidal quantum dots is the fact that, in the 25 years since they appeared, next to nothing has been obtained in terms of their morphological characterization, so that very little is known about their actual shape and composition. Indeed, extensive attempts have been made to gauge the size of the dot and of the layers grown via MOVPE within the pyramidal hole by using Atomic Force Microscopy[1] (AFM): this was done by cleaving the substrate so that the cleave plane intersected the pattern, thus allowing to perform cross-sectional analysis. However, results obtained in this way were rather limited, as the technique employed only allowed for a 2D scan, and was inherently unable to reconstruct the complex shape of the dot, let alone its chemical composition. Furthermore, relaxation of the exposed epi-structure's surface due to strain resulted in a fundamental perturbation of the system under investigation, and calls for a less invasive technique.

While models for the growth on 111A GaAs surfaces have been developed both for V grooves and inverted pyramidal holes[2,3], the lack of a direct and accurate characterization of the dot and its surrounding environment is obviously a serious issue that hampers development of novel pyramidal quantum dot families and prevents, for instance, any ab initio calculation of the dot's excitonic wavefunctions. Educated guesses can indeed be made on the profile of the dot's shape and confining potential, but as discussed in the Introduction of this thesis, the connection of the dot to a series of surrounding nanostructures tends to turn this in an exercise in futility due to the inherent complexity of the system. If, for instance, we consider the InGaAs in GaAs dot family, the dot itself is connected to at its corners to 3 lateral InGaAs quantum wires (themselves possibly having a varying Indium content across their

section) which would be expected to result in a lower confining potential at the corners.

For the GaAs/AlGaAs family of PQDs, the situation might be even more complex, as the dot's vertical confining effect is provided by two vertical AlGaAs quantum wires, formed by a gradient of the Al content in a plane perpendicular to the growth axis.

It is clear that a way to properly investigate the dots is needed. Indeed, in view of its high resolution, Transmission Electron Microscopy (TEM) would seem like a good candidate to do so.

7.1 Transmission electron microscopy: basics

In this sub chapter, the basics of Transmission Electron Microscopy (TEM) and Scanning Transmission Electron Microscopy (STEM) will be covered, in order to describe the capabilities and limitations of the techniques employed in the investigation of our samples, and introduce the terminology used in the rest of the chapter to discuss the obtained results.

As the name implies, TEM is a microscopy technique that relies on the transmission of an electron beam through a specimen under investigation[4]. The use of electrons, which possess a small De Broglie's wavelength, implies that a very high resolution can be achieved but, in striking contrast with SEM, this technique does not produce an image by collecting backscattered or secondary electrons generated by the interaction of the primary beam with the specimen, but rather employs a detector which is positioned on the opposite side of the sample with respect to the electron gun (figure 7.1), and this allows for much more sophisticated analysis capabilities than a SEM: while the latter is mostly confined to imaging of surfaces, the former can extrapolate information about buried structures as well. TEM however is a significantly

more complex tool, and sample preparation is often a delicate and time-consuming task: as the information about the specimen is carried by the electron current passing through the sample, in order to have a sufficient signal to noise ratio the specimen must be prepared in the form of thin slices called lamellae less than a hundred nanometers thick, a size comparable with an electron's mean free path in the material under investigation.

A STEM (Scanning Transmission Electron Microscope), is a more sophisticated version still, which uses a beam deflecting apparatus to scan the focused electron beam across the sample, and instead of simply using an imaging device such as a CCD for image reconstruction, boasts a series of detectors that analyze transmitted electrons, extracting physical information about the voxel (interaction volume between the beam and specimen) and producing a 2D map of the sample via raster scanning.

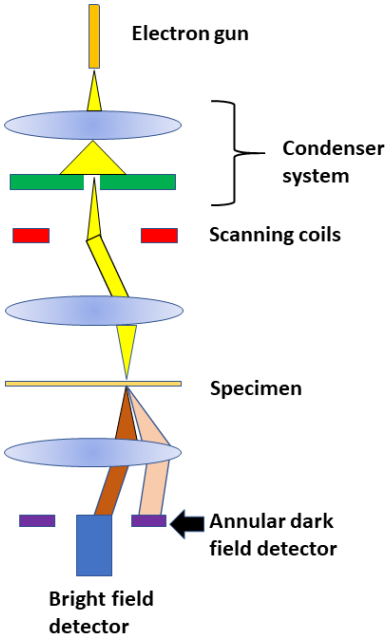


Figure 7.1 Sketch of a TEM system

Depending on which detector is used in the half space below the sample for image reconstruction, two types of images can be generated: bright field and dark field ones.

Bright field images are generated from transmitted electrons, using a detector which is located underneath the sample. This is the simplest and most common image generation technique, where areas of the sample that absorb or scatter electrons appear darker, while areas with lighter atoms appear brighter.

Annular dark field images, and high-angle annular dark field images (**HAADF**) are generated using, as the name suggests, an annular detector that collects electrons incoherently scattered at high angles by the interaction with atomic nuclei in the sample, with the choice of the angle allowing to also reject electrons that have undergone Bragg (coherent) scattering from crystal planes. As the scattering cross section is heavily dependent on the atomic number Z, this imaging mode is particularly suitable to detect heavy atoms embedded in a matrix of lighter ones. Also, it is a more suitable technique for the imaging of crystalline structures, and will give rise to bright features in the HAADF image against a darker background.

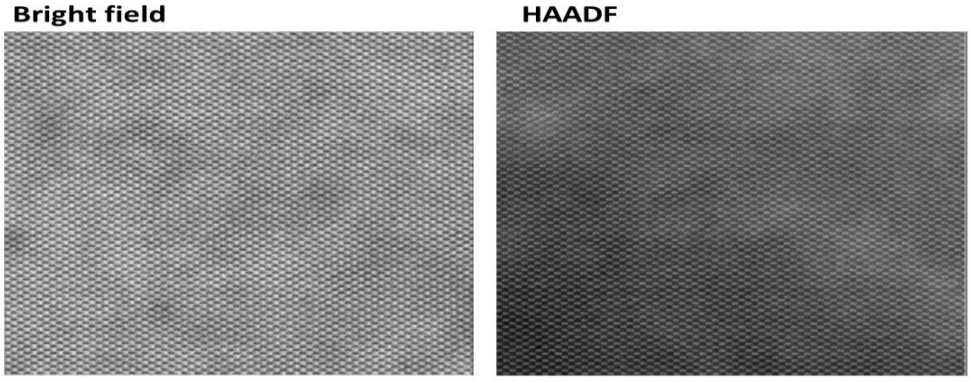


Figure 7.2 TEM bright and dark field images of a GaAs sample. Individual atoms can be identified

While imaging modes can provide a qualitative investigation of the chemical composition of the sample, techniques are available that allow to provide a quantitative analysis as well. The two most widely used techniques are:

Electron Energy Loss Spectroscopy (EELS). The energy of a photon is difficult to change via interaction with matter (Compton scattering for instance becomes significant only at very short wavelengths) but electrons, being charged particles, readily interact with the electron clouds surrounding atoms. If we consider an ideally monochromatic electron beam passing through a thin sample, as it happens in TEM/STEM, it is expected that after having crossed the sample, the beam will be polychromatic: as both the scattering cross-sections and energy lost in an individual inelastic scattering event are dependent on the electron clouds of the atom, that is, on its atomic number, an electron spectrometer allows to perform a chemical analysis and determine the composition of the voxel.

Energy-Dispersive X-Ray Spectroscopy (EDX) Interaction of the high energy electrons of the scanning beam with a core electron of the specimen's atom can result in the emission of the latter. The resulting ion would then be in a high energy excited state which would be short lived, as the missing core electron will be replaced by one transitioning from the atom's outer shell: such a transition would be accompanied by the emission of a photon in the X ray spectral region, which could in turn be collected by a spectrometer and provide an identification of the atom it was emitted from. In EDX terminology, the spectral fingerprint of a given element are its *characteristic X Rays*. EDX is sometimes also called Energy Dispersive Spectroscopy (**EDS**).

The two techniques are rather complementary, both in terms of analyzed energy spectrum and interaction mechanism: EELS probes how the material is excited, while EDX extracts information by the way the system relaxes. Also, a

typical EELS spectrum spans a few KeV, while a typical EDX spectrum spans tens of KeV.

7.2 Sample preparation techniques: lamellae cutting from back-etched structures

The first attempts to do TEM on pyramidal quantum dots were carried out by our collaborators in Belfast either on as grown or back-etched substrates. In both cases sample preparation involves the deposition on top of the sample of a thick platinum layer to protect it, followed by the milling of the thin TEM lamella using a Gallium-ions Focused Ion Beam (FIB), as shown in figure 7.3.

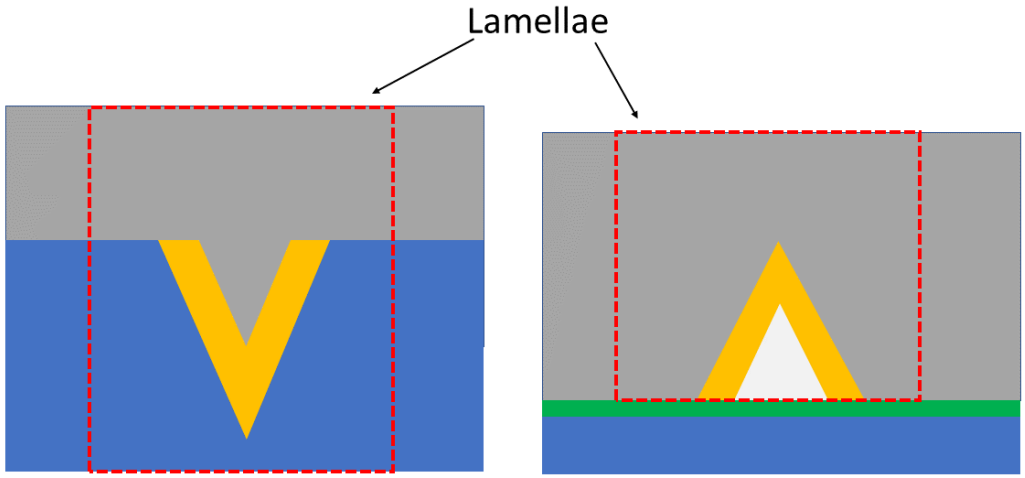


Figure 7.3 Sketch of the first approach for sample preparation: after deposition of a Pt protective layer, a lamella is cut using a Focused Ion Beam (FIB), either from an as grown sample (left) or a back-etched one (right)

In general, a sufficient contrast can be achieved in a conventional SEM to clearly identify the individual layers of the epi-structures, which in principle greatly simplifies the fabrication of a lamella comprising the region of interest.

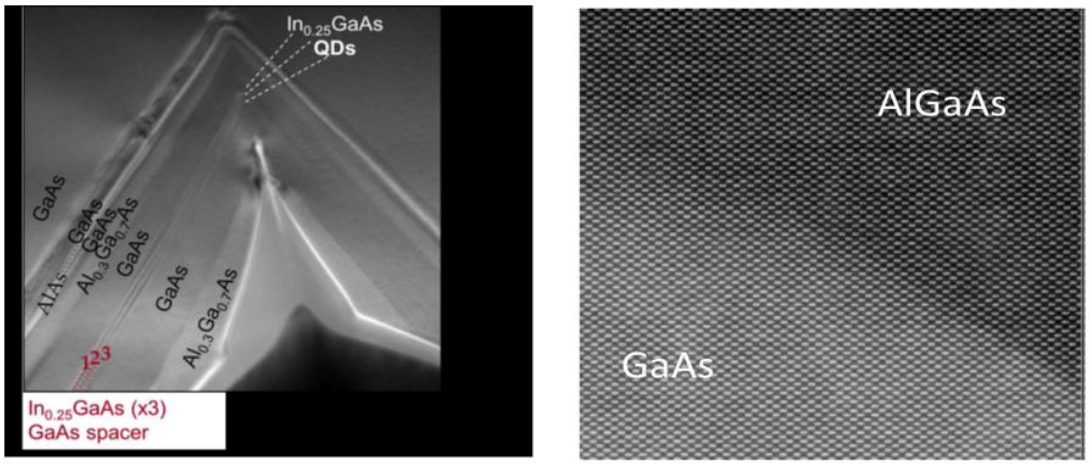


Figure 7.4 left, STEM low resolution image of a lamella, with individual layers clearly distinguishable. Right, high resolution image of the interface between a GaAs and an AlGaAs layer grown on one of the tetrahedral faces. Individual atoms can be seen, as can a clear transition between the different layers.

Figures 7.5 and 7.6, display some key results obtained by STEM analysis of lamellae prepared from back-etched samples. EDX maps clearly show qualitative elemental distributions and interfaces between various layers, but significant issues arise when magnification is increased and a quantitative analysis of the alloy compositions is attempted.

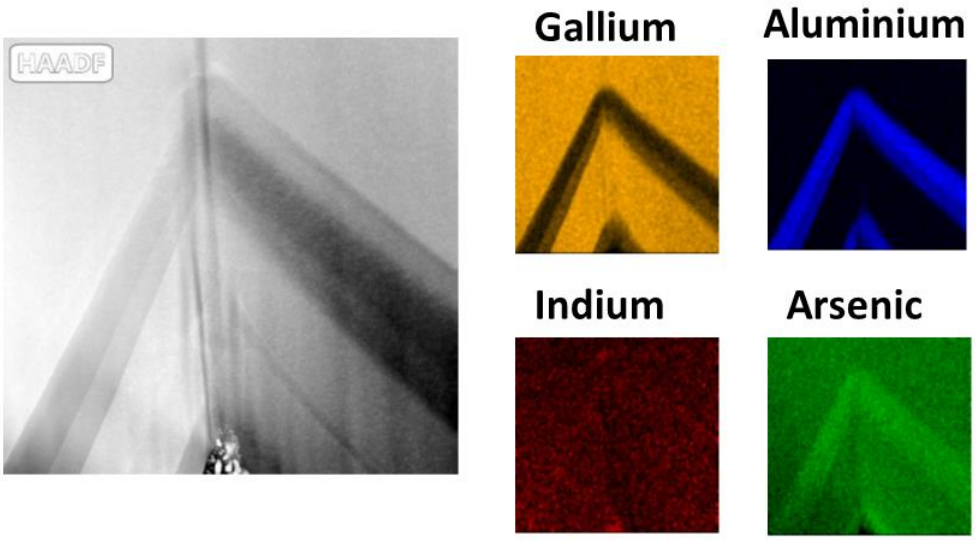


Figure 7.5 single quantum dot EDX map

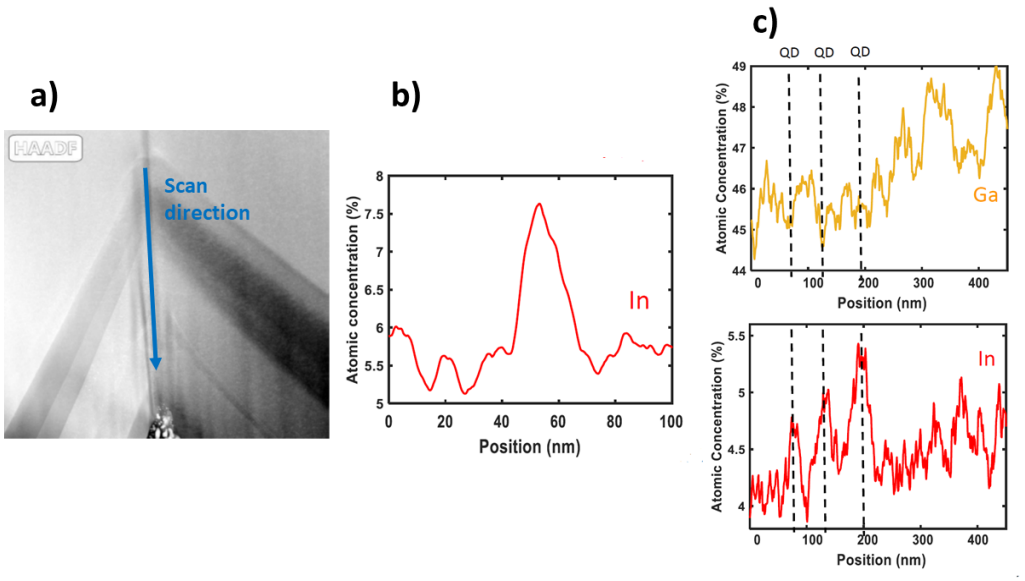


Figure 7.6 a) HAADF image of a lamella cut from a back-etched pyramid. b) Indium atomic concentration in one of the lateral quantum wells. C) In and Ga atomic fraction obtained via EDX analysis for a triple quantum dot system, along the scan direction marked in a).

A typical result is shown in figure 7.6, and was obtained on a sample containing three stacked quantum dots, with a nominal In concentration of 25%: while the results are expressed in terms of atomic fraction (so that they must be doubled in order to give the correct stoichiometry), the detected levels of Indium are quite small, even more so if compared to the background noise, and not compatible with the confining effect of the quantum dots, as the expected bandgap would be larger than the energy of the typical transitions observed in micro-PL. Interestingly however, and despite the unphysical results, the three quantum dots produced clearly defined peaks when a linear scan was performed along the growth axis.

Repeating measurements with lamellae of different sizes or with different samples did not affect the outcome significantly for quantum dots, while the analysis of quantum wells yielded slightly better results, especially when the lamella was cut perpendicularly to the well, but estimations of the In concentrations still appeared to be quite off with respect to nominal values. This is quite surprising, as the position of the dot can indeed be seen in both

bright field and HAADF TEM images, but it looked like either the techniques employed to investigate its chemical composition were not sensitive enough to determine it, or the 3 dimensional nature of the system complicated the matter by creating shadowing effects, as results obtained by scanning the lateral quantum wells formed on the 111A faces seem to suggest.

Moreover, sample preparation likely did not help, as the cutting of a lamella is more complex in this case that for a simple, planar epi-structure with rather uniform layers.

7.3 Advanced sample preparation techniques: cutting of lamellae from nanopillars

In order to simplify sample preparation, I proposed to switch once more to the nanopillar geometry, and to add AlAs marker layers above and below the quantum dot that could help identifying its position: as discussed in the previous chapters, the fabrication of nanopillars preserves the symmetry of the original tetrahedral template, and since the final structure has a smaller size, it should be possible to machine a lamella with a greater precision.

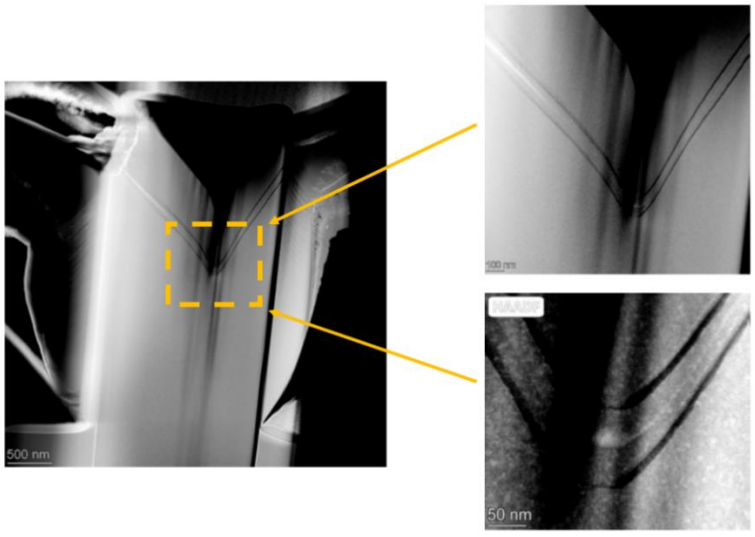


Figure 7.7 TEM lamella cut from a nanopillar. Two AlAs marker layers, placed above and below the quantum dot, help identifying its position

The approach proved to be successful, and a realistic estimation of the In concentration in the quantum dot was finally achieved. Whether this is due to the nanopillar geometry helping to find the correct position to mill the lamella, or the SiO_2 mask still present on top of the pillar protecting the structure during the Ga FIB milling is not clear, but the results speak for themselves: the atomic concentration implies that the alloy of the dot is $In_{0.22}GaAs$, very close to the nominal composition of 25% Indium. It can also be seen from the scan performed along the vertical axis that the concentration of In changes rather smoothly and in an asymmetric way, compatibly with a domed shape created by the evolution of the growth profile and In diffusion (fig. 7.8).

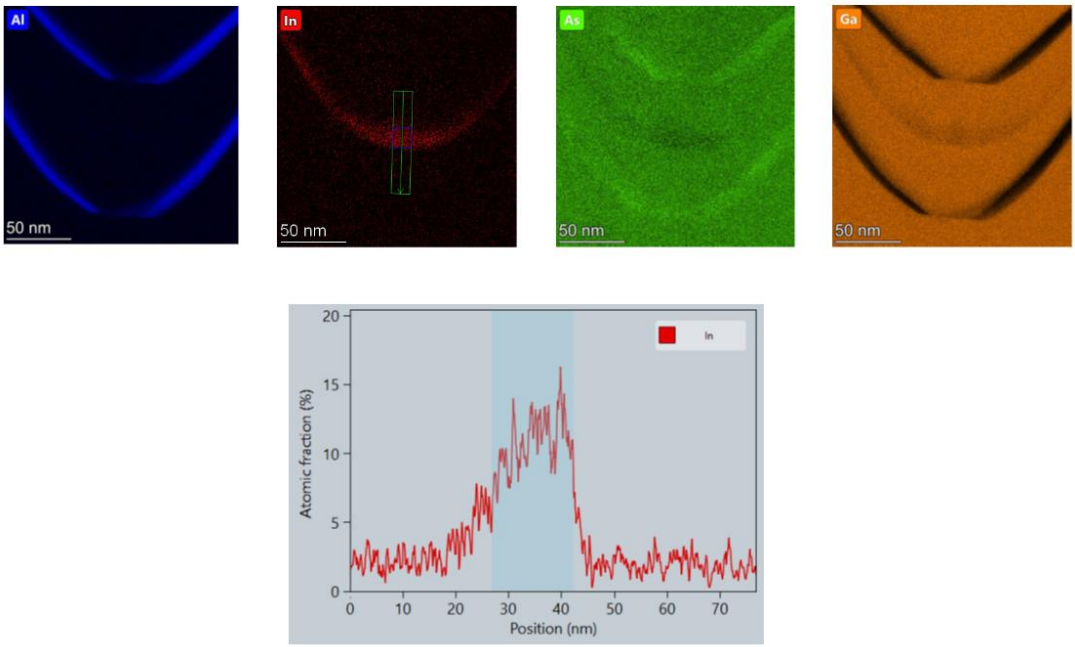


Figure 7.8 Top row: color map of elemental concentrations. Bottom: scan of In atomic concentration along the growth axis at the position of the quantum dot.

It is also surprising that the Al content drops in center of the structure, which seems to imply that it is quite difficult for it to grow along the 111B direction: the effect was already qualitatively predicted by growth models[3], but its magnitude is unexpected. This may also explain why the etch stop layer often

fails to protect the quantum dots when the back-etching procedure is performed, as AlAs will grow extremely thin along the axis, leading to a faster etching of the pyramidal tip.

While TEM finally allowed to validate some assumptions about growth models such as the formation of the lateral quantum wells and the entity of the segregation effects that leads to the formation of the nanostructures in the first place, it became clear at this point that the complexity of pyramidal quantum dots systems made their characterization via TEM quite challenging. Multiple crystal planes and different nanostructures surrounding individual quantum dots render reconstructing the morphology and elemental distribution significantly difficult, especially in view of the fact that PQDs are an inherently 3-dimensional system, and TEM always collapses a 3D structure in a 2D image.

Milling of horizontal lamellae, and their tilting to allow for a proper tomographic scan is possible[5–7], albeit quite challenging. Preliminary results in this sense have already been obtained: in this case a precise location of the dot in the plane was not necessary for the milling of a lamella, and the use of nanopillars was deemed unnecessary. As such, after growth of a sample with multiple quantum dots and its planarization, a horizontal lamella was milled using only the FIB.

Results from this sample (fig. 7.9) have shown that InGaAs quantum dots have an hexagonal shape in plane, with a small bulging in the center that appears to be In-enriched, and is likely to provide the confinement effect. This is a consistent with results obtained via AFM scan of MOVPE-grown structures in tetrahedral nanoholes[8], where however the size of the structure is comparable with the adatom diffusion length. A precise estimation of the stoichiometry was however impossible, as the dot is much thinner than the lamella, and

measurements of the atomic fraction suffer from an averaging effect from the large amount of GaAs that makes up the rest of the lamella.

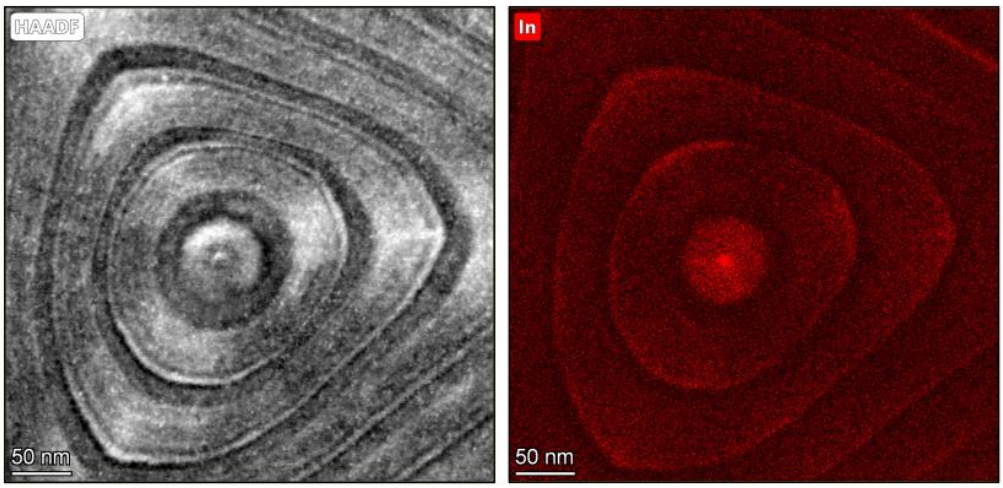


Figure 7.9 Left, HAADF image from a horizontal lamella of a PQD. Right: EDX Indium map

Nevertheless, these results provide some much needed structural information on PQDs, and in particular the strong segregation effect which has been observed might be a source of FSS, due to the strong alloying and higher disorder in its proximity.

While we still have hope that this could give us more information in the future, I started looking for a different technique that could get rid of the shortcomings of the TEM altogether, and complement the data so far collected.

7.4 A different approach: atom probe tomography

Atom Probe Tomography (APT) is indeed a promising candidate, as it allows for 3D reconstruction of a specimen down to the atomic level[9].

The technique works by first of all preparing the sample in a needle-like configuration, with a very sharp tip of a few tens of nm radius. The sample is placed in ultra high vacuum (UHV) conditions, and atoms are evaporated from the tip using voltage pulses or a combination of a high voltage bias between the sample and a counterelectrode, and laser pulses promoting ionic emission. The highly inhomogeneous electric field generated by an annular electrode accelerates ions toward a detector and allows for a 2D imaging of the emitted atom layer, while time-of-flight analysis allows to determine the mass, i.e. the chemical nature, of the ions. The procedure is repeated for as many times as needed, exfoliating and scanning the sample one atomic layer at a time for hundreds of nanometers.

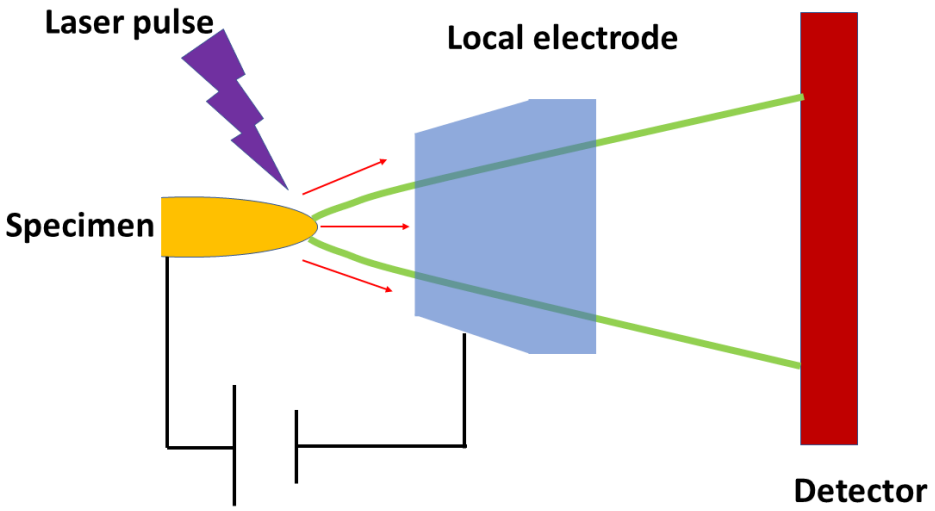


Figure 7109 Sketch of a typical APT apparatus. Laser pulses and intense electric fields cause an ablation of the material. Ions are accelerated by a radial electric field, and a detector allows for reconstruction of atomic distribution

Preparation of the sample involved once more the development of a dedicated procedure, and the resulting approach is a multi-step process aimed at fabricating a nanowire containing the quantum dots.

7.5 Fabrication of samples for APT-first strategy

First of all, as the scan depth in a typical ATP measurement is limited, samples containing a stack of multiple quantum dots were grown. A thick Cr layer (around 1 micron) was deposited on the as grown sample to fill up the vestigial recess and to increase the height of the final pillar. The plan was then to use a conventional back-etching to subsequently expose the pyramids, and a thick Silicon Nitride layer was to be deposited to protect the epitaxial layers during the aggressive milling with the focused ion beam, which could be used to cut away a nanopillar, while leaving a small tether to hold it in place. Silicon nitride was then to be removed in a plasma asher using a CF4 chemistry, thus exposing the GaAs layers, and the FIB was to be used once more to cut away the fabricated nanowire, and finally attach it to a probe. The final step of sample preparation involves the sharpening of the nanowire in a high electric field.

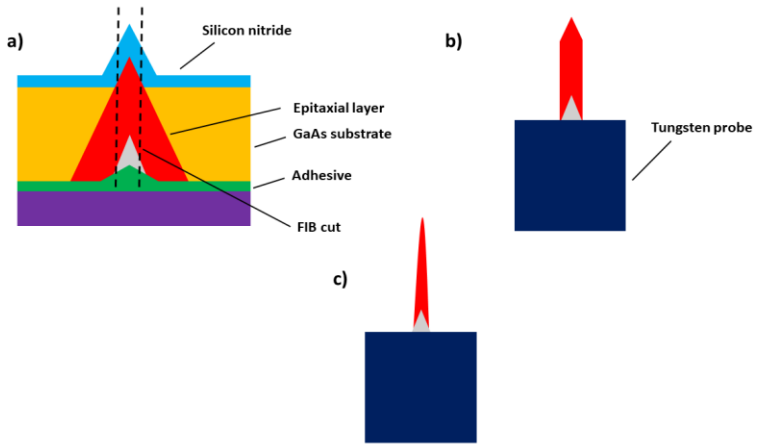


Figure 7.11 Sketch of the first technique developed for sample fabrication. a) a back etched sample is milled using a fib and the resulting post is attached to a Tungsten probe (b). Finally, an electrosharpening of the milled pillar is performed to prepare the final needle-like specimen.

However, the thick metal layer caused significant problems during the early processing steps: its thermal expansion when heated at 150 degrees or more resulted in a delamination from the adhesive, and caused significant bending and disuniformity across the sample.

A better approach, which removes the need to subject the sample to several thermal cycles is the use of a dry etch process to expose the pyramids: this required the development of a sufficiently fast selective etching of GaAs over AlGaAs/AlAs, which can be achieved by employing a BCl_3/SF_6 plasma chemistry, where the fluorine interacts with the AlGaAs to create an AlF passivating layer and prevent the damaging of the pyramid.

Indeed, fabrication of samples in this way is possible, and using micro-PL to assess the impact of this processing approach on the quantum dots indicated no degradation of the spectral quality, suggesting the dry etching process tends to introduce negligible surface defects.

Milling the pillar using the FIB was however found to be less straightforward than expected: even if the tip of the pyramid can be seen in the SEM, the fact that what is exposed is a 3-dimensional structure caused issues with location of the exact position where the milling has to be performed, and the need to remove the adhesive from the bottom of the sample prior to gluing on the APT tip complicated the overall process.

7.6 Fabrication of samples for APT-direct milling using FIB

A simpler yet more effective approach was found to be the direct milling of the pillars using the FIB, starting from planarized samples with a Cr protective layer evaporated upon them: if the sample is not fully polished, a small vestigial recess is left above the quantum dots and can be used to identify their positions. Evaporation of a thin (500 nm) layer of Cr doesn't remove the recess, but can be an effective protection of the epi-layer underneath if a vertical milling is performed using Ga ions. An additional advantage in this case is the possibility of milling a perfectly circular pillar, without any issue related to the tetrahedral faces of the pyramid, which might avoid further complications arising from an asymmetric electric field during the final sharpening phase of the pillar or the analysis of the sample.

A cylinder was fabricated in this way using the FIB system available in Tyndall, with a diameter as small as 800 nm, and subsequently transferred onto the tungsten tip and glued using a Carbon deposition. The final result can be seen in figure 7.12.

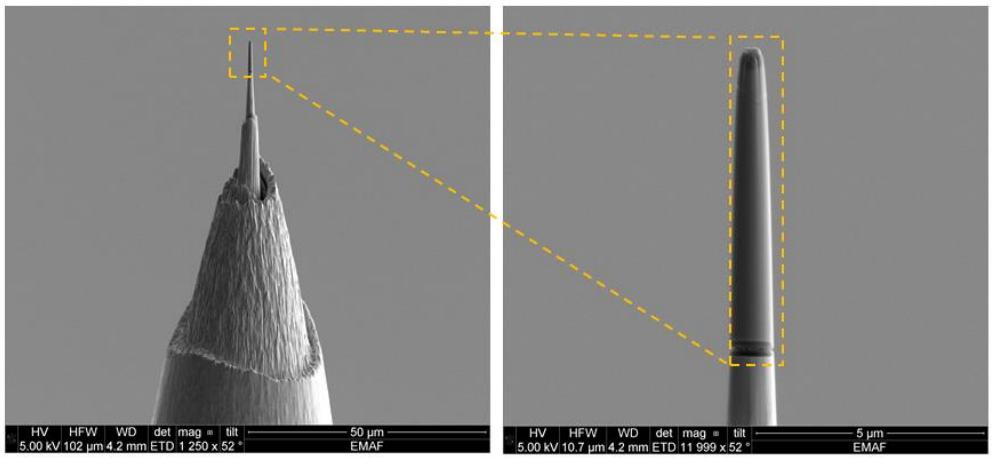


Figure 7.12 APT sample fabricated using FIB milling. Left: sample mounted on a Tungsten probe after final sharpening. Right: detail of the GaAs milled pillar. The Carbon bonding layer can be seen between the Tungsten tip and the GaAs pillar

A first batch of samples has been fabricated in this way and has been sent for APT analysis to CEA-Leti in Grenoble at the time this thesis is being written, as part of the Ascent project I have recently been awarded.

1. Juska, G., Dimastrodonato, V., Mereni, L. O., Gocalinska, A. & Pelucchi, E. Towards quantum-dot arrays of entangled photon emitters. *Nat. Photonics* **7**, 527–531 (2013).

2. Dimastrodonato, V., Pelucchi, E. & Vvedensky, D. D. Self-Limiting Evolution of Seeded Quantum Wires and Dots on Patterned Substrates. *Phys. Rev. Lett.* **108**, 256102 (2012).

3. Pelucchi, E., Moroni, S. T., Dimastrodonato, V. & Vvedensky, D. D. Self-ordered nanostructures on patterned substrates. *J. Mater. Sci. Mater. Electron.* **29**, 952–967 (2018).

4. Williams, D. B. & Carter, C. B. Transmission electron microscopy: A textbook for materials science. *Transm. Electron Microsc. A Textb. Mater. Sci.* 1–760 (2009) doi:10.1007/978-0-387-76501-3.

5. Chen, C.-C. *et al.* Three-dimensional imaging of dislocations in a nanoparticle at atomic resolution. *Nat. 2013 4967443* **496**, 74–77 (2013).

6. Kübel, C. *et al.* Recent Advances in Electron Tomography: TEM and HAADF-STEM Tomography for Materials Science and Semiconductor Applications. *Microsc. Microanal.* **11**, 378–400 (2005).

7. Arslan, I., Yates, T. J. V., Browning, N. D. & Midgley, P. A. Embedded Nanostructures Revealed in Three Dimensions. *Science (80-.).* **309**, 2195–2198 (2005).

8. Surrente, A. *et al.* Self-formation of hexagonal nanotemplates for growth of pyramidal quantum dots by metalorganic vapor phase epitaxy on patterned substrates. *Nano Res. 2016 911* **9**, 3279–3290 (2016).

9. Kelly, T. F. & Miller, M. K. Atom probe tomography. *Rev. Sci. Instrum.* **78**, 031101 (2007).

4. Conclusions

In the course of my nearly 4 years in Tyndall I have been involved in a broad series of activities and started quite a few novel research lines, several of which are still ongoing. Many plans were quite ambitious, aiming to significantly change the prospective for application of Pyramidal Quantum Dots in the field of quantum information, and only time will tell whether some of the work I have started will bear fruits. Indeed, I believe I have significantly broadened the range of processing techniques available for these kind of dots, provided for the first time a deeper understanding of the mechanisms determining light emission from pyramidal structures, and suggested several ways to improve it.

The development of GaAs dots, to which I have contributed alongside my colleagues, has paved the way to the possibility of achieving resonant excitation of the quantum emitter: a fundamental milestone that was necessary to reach in order to provide a jitter-free population of the biexcitonic state and high quality spectral emission, although a significant work lies ahead to achieve a high degree of photon indistinguishability.

In conjunction with Prof. Di Falco's group we have also demonstrated the potential of Electron Beam Induced Deposition to the field of solid state quantum light sources, and paved the way for the fabrication of complex 3D features on top of individual quantum emitters: we believe that this technique complements the ones already available to our community due its additive nature, and expect significant developments in the future..

The fabrication technique I have developed for micro/nanopillars has already provided us with our own record of extraction efficiency, and for the first time allowed to fabricate samples suitable for TEM analysis. The latter has finally given us an insight into the structure and shape of the dots and various surrounding nanostructures, although much work lies ahead to increase our

understanding of this system, and we have great hope that the novel approach which I have suggested, Atom Probe Tomography, will expand the work we have done so far.

I believe the greatest contribution I have given during my PhD is theoretical framework I have developed for a posteriori entanglement restoral, which expands the proposal from Wang et al. by taking into account the effects of other phase terms originating from imperfections of the setup, and is overall more intuitive and easy to grasp. I hope one day to see my model confirmed (or disproved) by experimental evidence.

Future works

FSS tuning: Our preliminary results indicate that tuning of the FSS using piezoelectric actuators is indeed feasible, but an optimization of the sample fabrication technique is probably needed to yield reliable devices. This is even more important now, as the transition to GaAs dots implies working with dots that have on average a higher FSS, and demands an external mechanism to generate entangled photons without compromising brightness via post-selection;

APT of Pyramidal Quantum Dots: Atom Probe Tomography seems to be the ideal technique to investigate the shape and composition of our quantum dots. The collaboration I have set up with CEA-LETI might soon provide a feedback on whether this is the case;

Coupling of micro/nanopillars to waveguides: Interfacing pyramidal quantum dots with a photonic chip is obviously the next major hurdle. The higher brightness achieved with the micro and nanostructures that I have developed, in conjunction with their better far field when compared to the usual pyramids suggests that this could be a potential route. Novel ways to transfer individual structures have to be devised, although our results obtained with the Focussed

Ion Beam and its micromanipulators suggest that this tool could be a viable option.

Appendix A

Supplementary information for "Planar Semiconductor Membranes with Brightness-enhanced Embedded Quantum Dots via Electron Beam Induced Deposition of 3D Nanostructures: Implications for Solid State Lighting"

List of contents

1. **Images of each of the structures fabricated during the first set of depositions……..138**
   - **1.1 Platinum patterns**
   - **1.2 SiO2 patterns**
2. **Images and data of the second set of depositions……140**
3. **EDX analysis of SiOx structures…….……143**

1. High resolution images of each of the structures fabricated during the first set of depositions

1.1. Platinum patterns

All of these patterns have been fabricated using the precursor $(Me_3)MeCpPt$, and decomposing it with a deposition current of 150 pA, accelerating voltage of 3 kV, dose of 1 C/cm^2, step size of 20 nm, and dwelling time of 50ms, at room temperature

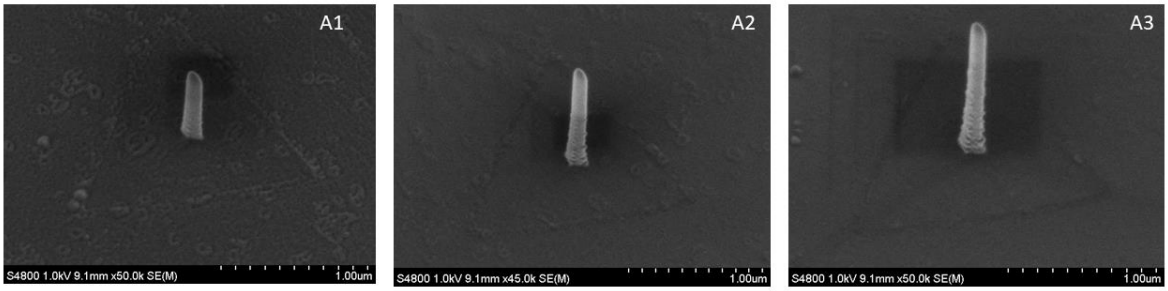


Figure S1: Pt pillars fabricates during the first set of depositions

1.2. SiO2 patterns

All of this structuers have been fabricated by decomposing the precursor Penta Methyl Cyclo Penta Siloxane (PMCPS), with a deposition current of 150 pA, accelerating voltage of 3 kV, dose of 1 C/cm^2, step size of 10 nm, and dwelling time of 0.01ms with variable (100-5000) writing loops at room temperature

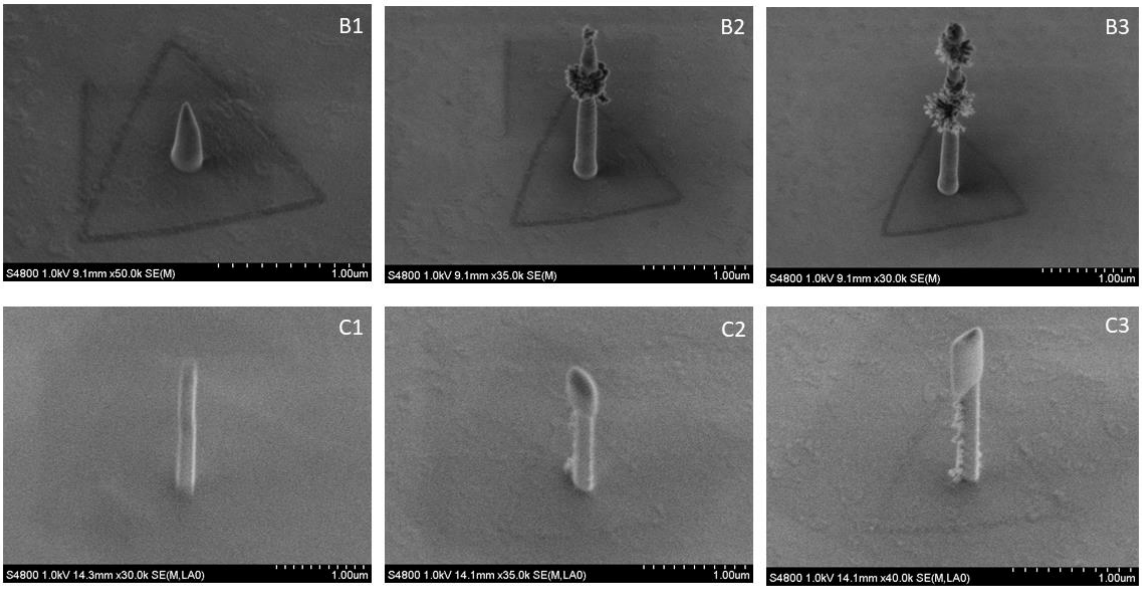


Figure S2 Si-O-C structures fabricated during the first set of depositions from B1 to C3

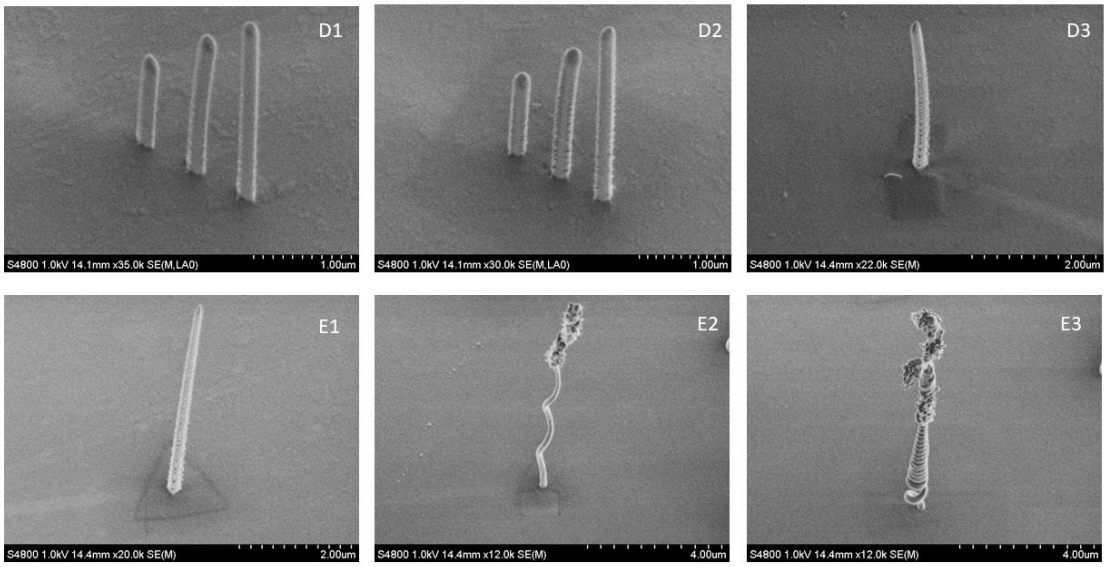


Figure S3 Si-O-C structures fabricated during the first set of depositions, from D1 to E3

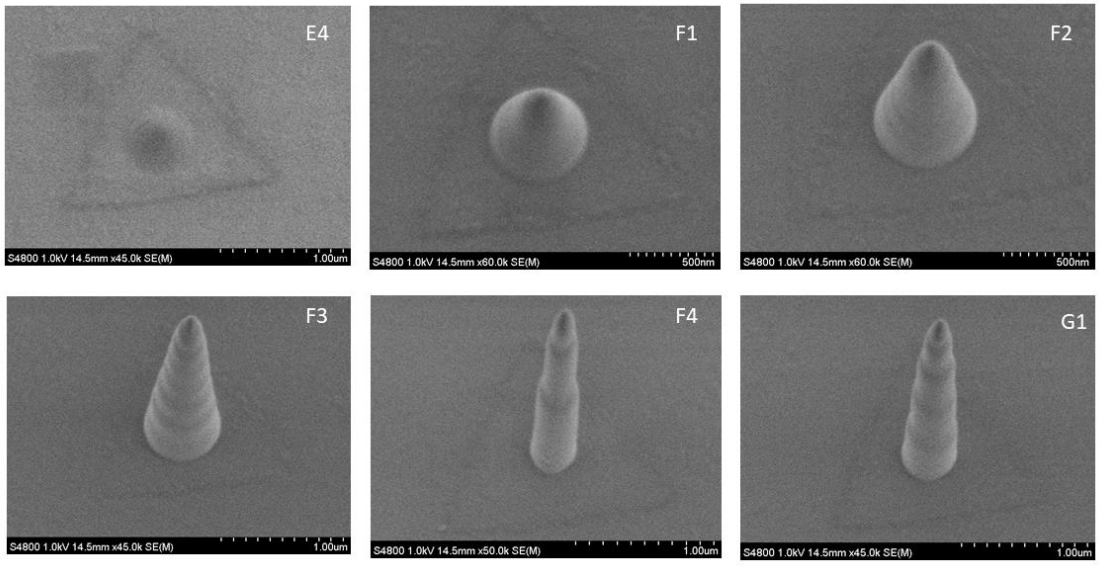


Figure S4 Si-O-C structures fabricated during the first set of depositions, from E4 to G1

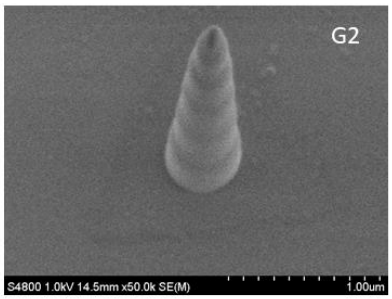


Figure S5 Si-O-C structure fabricated during the first set of depositions, G2

2. Second set of depositions on previously mapped QDs

All of this depositions are of SiO2 pillars, deposited using the same conditions employed for the first series

Table S2 Geometrical parameters of the structures fabricated during the second set of depositions

Sample #	w (nm)	h (nm)
1	576	250
2	609	617
3	613	904
4	620	1200
5	641	1530
6	657	1700
7	647	1650

Sample #6 shows irregular pattern due to the fabrication error. Please check the SEM image.

Sample #	w (nm)	h (nm)
8	496	206
9	536	530
10	566	810
11	569	1070
12	576	1310
13	588	1450

Sample #	w (nm)	h (nm)
14	391	177
15	432	367
16	481	571
17	464	793
18	465	1020
19	476	1070

Sample #	w (nm)	h (nm)
20	285	140
21	341	283
22	357	391
23	361	511
24	373	673
25	376	749

Sample #	w (nm)	h (nm)
26	199	119
27	225	146
28	261	202
29	257	276
30	270	338

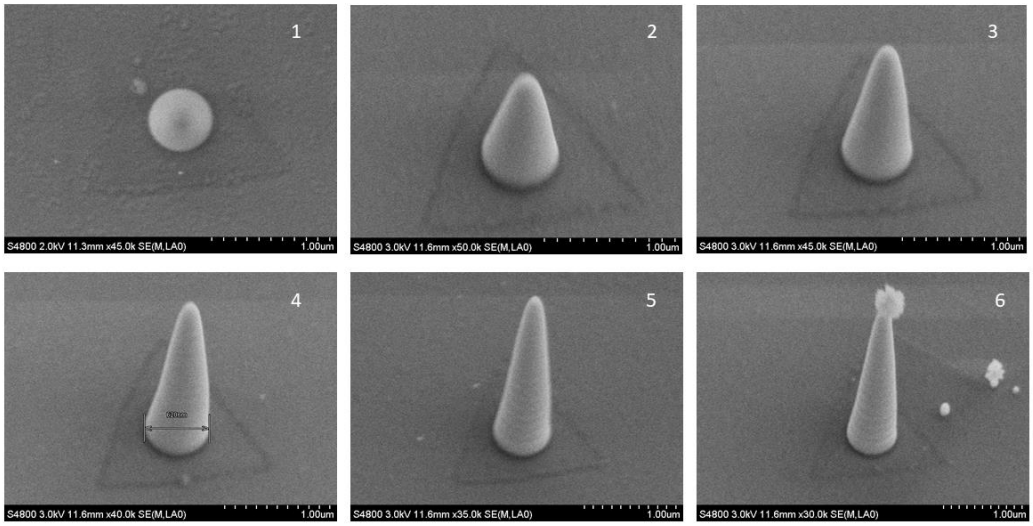


Figure S6 Si-O-C structures fabricated during the second set of depositions, 1 to 6

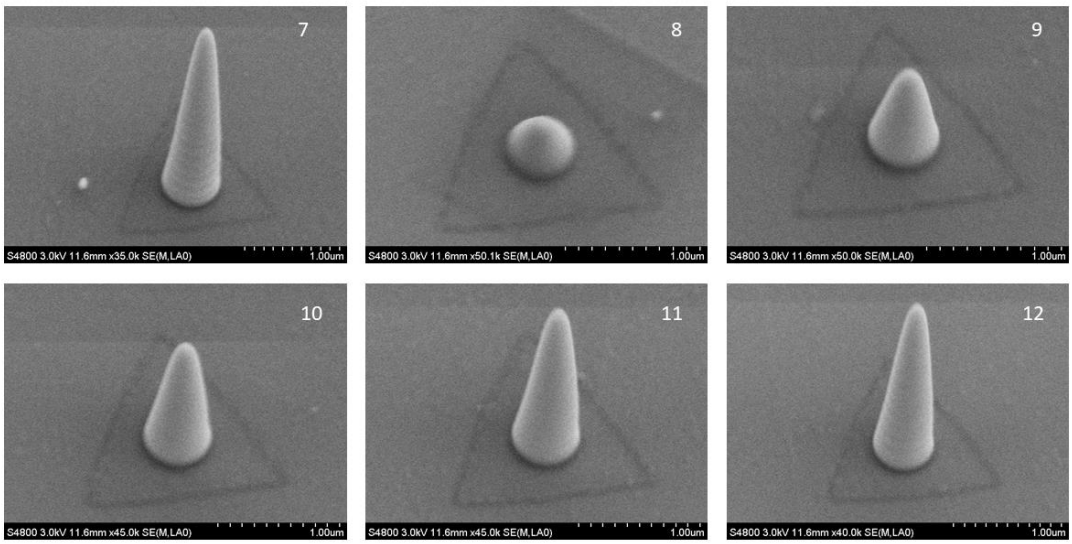


Figure S7 Si-O-C structures fabricated during the second set of depositions, from 7 to 12

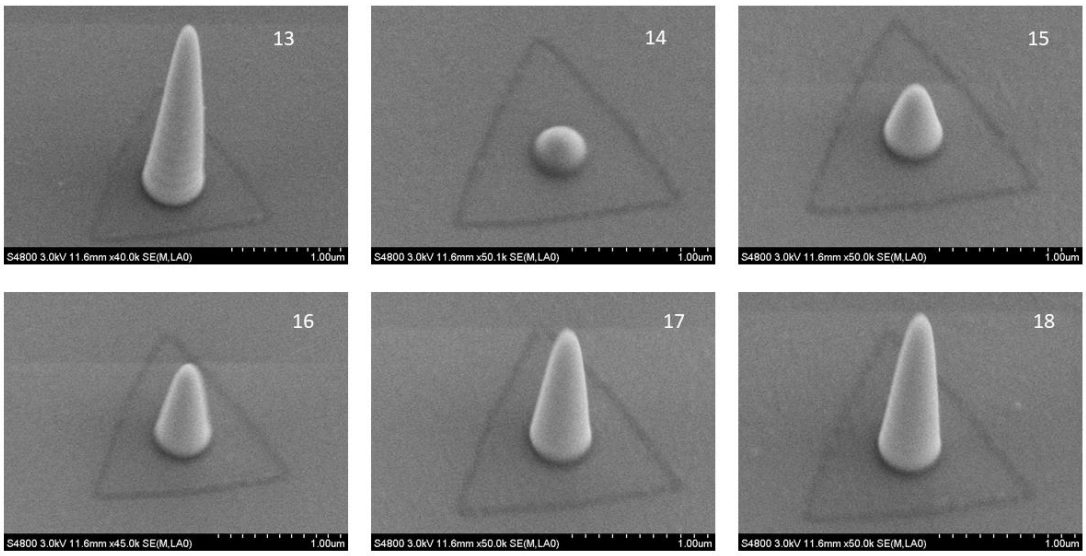


Figure S8 Si-O-C structures fabricated during the second set of depositions, from 13 to 18

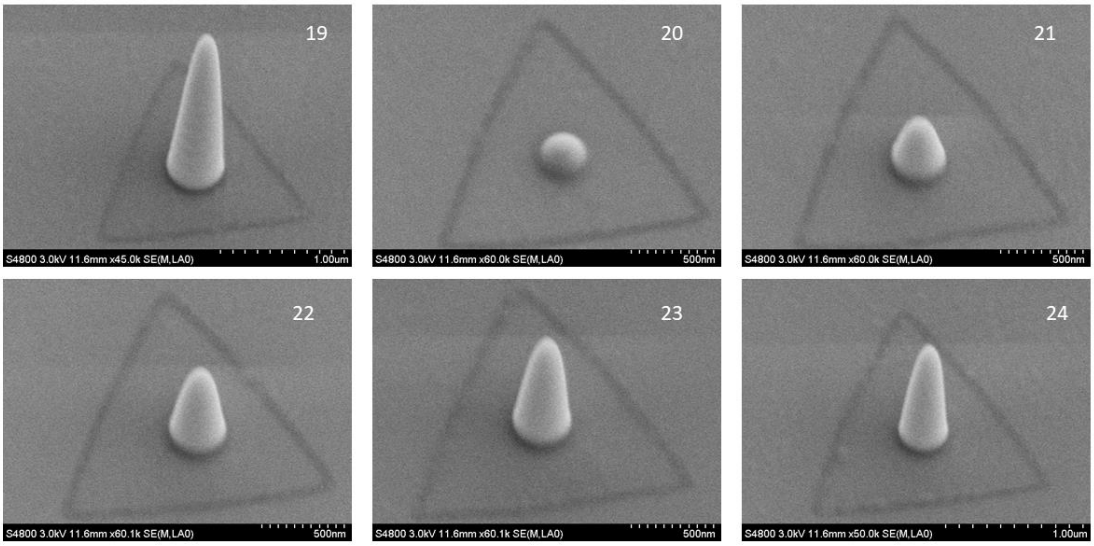


Figure S9 Si-O-C structures fabricated during the second set of depositions, from 19 to 24

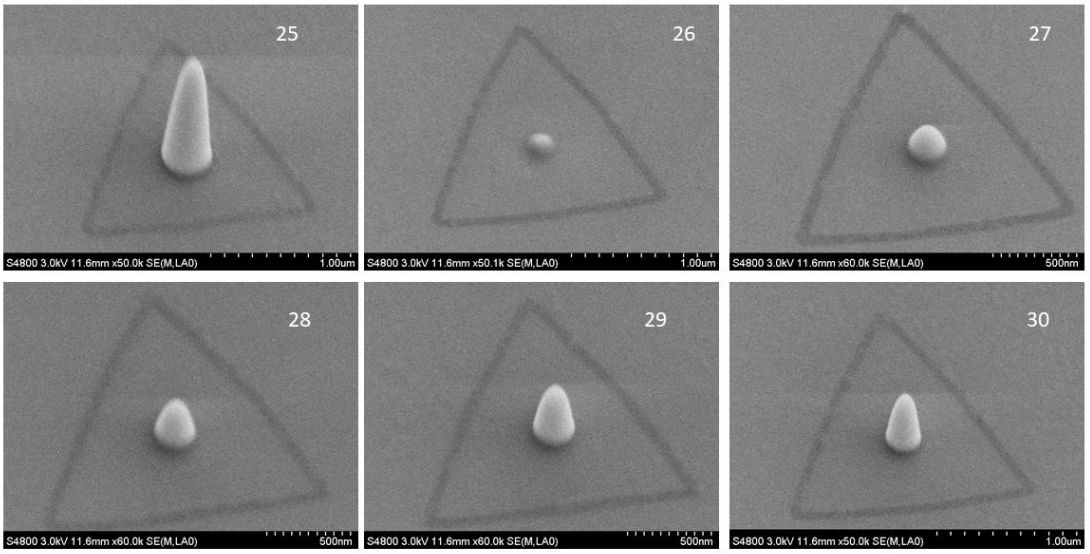


Figure S10 Si-O-C structures fabricated during the second set of depositions, from 25 to 30

3. EDX analysis of SiOx structures

EDX analysis was performed on SiOx nanostructures using a Quanta 650 SEM. A typical spectrum and elemental analysis are included.

Table S3 Results of the EDX analysis. Atomic percentages rounded to the nearest integer

Element	Weight%	Atomic%
O K	19.85	47
Si K	12.45	17
Ga K	31.41	17
As L	36.29	18
Totals	100.00	

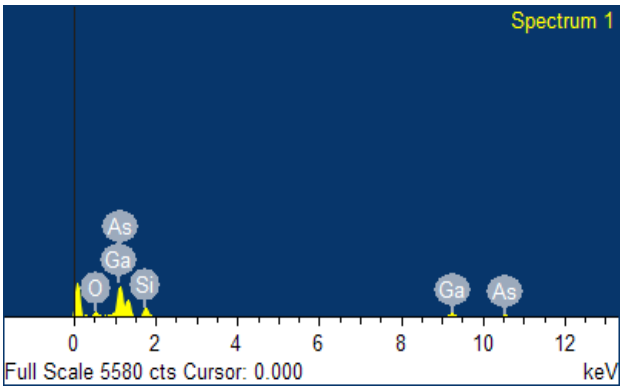


Figure S11 EDS spectrum of the analyzed structure